Multiscale Numerical Investigation of Crystallization Processes with Lattice Boltzmann Methods

Zur Erlangung des akademischen Grades eines

DOKTORS DER INGENIEURWISSENSCHAFTEN (DR.-ING.)

von der KIT-Fakultät für
Chemieingenieurwesen und Verfahrenstechnik des
Karlsruher Instituts für Technologie (KIT)
genehmigte

DISSERTATION

von

M.Sc. Fedor Bukreev

aus Moskau

Tag der mündlichen Prüfung: 25. November 2025

Erstgutachter: PD Dr. rer. nat. Mathias J. Krause
Zweitgutachter: Prof. Dr.-Ing. habil. Matthias Franzreb

Danksagung

Diese Arbeit ist in der Lattice Boltzmann Research Group (LBRG) unter der Betreuung von Herrn Mathias J. Krause entstanden.

Ich möchte mich bei Herrn Krause für die ausgezeichnete Betreuung bedanken. Tagtäglich hat er mir bei meinen zahlreichen Fragen mit nützlichen Ratschlägen zur Seite gestanden, die nötigen Ressourcen besorgt und sich um eine freundliche und kreative Atmosphäre in der Arbeitsgruppe gekümmert. Besonders dankbar bin ich für die Möglichkeit, an vielen Konferenzen in der ganzen Welt teilnehmen zu dürfen.

Mein Dank gilt auch meinen Kollegen, die stets bereit waren, mir während der Arbeit und in der Freizeit in allen möglichen Belangen zu helfen. Ich schätze ihre hervorragende Zusammenarbeit und die gemeinsam verbrachte Zeit, die in diesen fünf Jahren zu einer echten Freundschaft gewachsen ist.

Ich möchte meinen Eltern danken, die mich bei all meinen Vorhaben stets unterstützt und motiviert haben. Auch meinen Verwandten in Deutschland möchte ich meinen Dank aussprechen: Die Zeit, die ich mit ihnen verbracht habe, hat mir immer geholfen, mich von der Arbeit und anderen Sorgen abzulenken. Schließlich möchte ich meinen Freunden danken, auf die ich mich immer verlassen konnte.

Zusammenfassung

Phosphor ist eines der wichtigsten chemischen Elemente in der Landwirtschaft und der chemischen Industrie. Die vorhandenen Phosphorressourcen reichen möglicherweise nicht aus, um den aktuellen industriellen Bedarf zu decken, weswegen es notwendig ist, effiziente Methoden zur Rückgewinnung von Phosphor aus alternativen Quellen zu entwickeln. Eine solche Quelle ist Abwasser, das weltweit ein bislang kaum genutztes Reservoir für Phosphor darstellt. Eine vielversprechende Lösung für die Nutzung dieser Quelle ist das P-RoC-Verfahren (*Phosphorus Recovery from Wastewater by Crystallization*), eine am Karlsruher Institut für Technologie (KIT) entwickelte, fortschrittliche Abwasserbehandlungstechnologie, wo das gelöste Phosphat aus dem Abwasser an Calciumsilikathydrat-(CSH)-Mikropartikeln in einem Rührkesselreaktor kristallisiert. Damit diese Technologie in der Praxis eingesetzt werden kann, muss ihre Effizienz verbessert werden. Leider besteht ein Wissensmangel sowohl über die Phosphatkristallisation unter dynamischen Bedingungen, als auch über eine dynamische Darstellung des Reaktion auf der nanometrischen Porenebene innerhalb der Mikropartikel. Ziel dieser Arbeit ist es daher, zu untersuchen, welche Prozessparameter in einem Rührkristallisator optimiert werden können und wie die Stoffmischung, Reaktion und Kristallisation auf Porenebene präzise vorhergesagt und beeinflusst werden können.

Hierzu wird ein multiskaliger Lösungsansatz vorgestellt, der die Hauptschritte der numerischen Analyse beschreibt. Dieser Ansatz modelliert den Kristallisator auf der Makroskala, heterogene und homogene Mischungs- und Reaktionsprozesse auf der Mikroskala sowie Transport- und Kristallisationsphänomene auf der Nanoskala. Aspekte der Fluid-Struktur-Interaktion (FSI), wie die Bewegung von Partikeln oder des Rührwerks, werden in dieser Arbeit nicht berücksichtigt. Auf allen Skalen – mit Ausnahme von FSI-Szenarien – wird ein eulerscher Mehrphasen-Mehrkomponentenansatz verwendet, da jede Phase und Komponente im Modell als kontinuierlich angenommen wird. Zur effizienten Berechnung auf hochparallelen Systemen und zur Auflösung der Simulationen auf dem erforderlichen Detaillierungsgrad wird die Lattice-

Boltzmann-Methode (LBM) als Diskretisierungsstrategie gewählt. Die grundlegenden theoretischen Konzepte zu Modellierung und Diskretisierung werden dargestellt, und die definierten Fragestellungen werden systematisch auf allen drei Längenskalen bearbeitet. Alle entwickelten Modelle wurden in der Open-Source-Softwarebibliothek *OpenLB* implementiert und sind über die entsprechenden Git-Commits oder durch Kompilieren der in der veröffentlichem Repository enthaltenen Examples reproduzierbar. Eine Beschreibung sämtlicher Setups und Modelle befindet sich im Anhang dieser Arbeit.

Auf Makroskala wird der vollständige Reaktor modelliert, wobei CSH-Mikropartikel, Phosphatspezies und Partikelbeladung als kontinuierliche eulersche Phasen betrachtet werden. Die heterogene Reaktionskinetik wird über die Linear Driving Force (LDF)-Methode abgebildet, unter Verwendung experimentell bestimmter Adsorptionsisothermen und mehreren Stufen des Stoffaustauschs. Die Validierung anhand analytischer Benchmarks, wie einem Batch-Reaktor und einem Festbettreaktor mit Massentransferzone (MTZ), bestätigt die Zuverlässigkeit des Modells bei geringen Feststoffvolumenanteilen und rechtfertigt die Verwendung einer einseitigen Kopplung zwischen Strömungs- und Stofftransportgleichungen. Das Modell stellt die erste Simulation der Adsorption an bewegenden Partikeln dar und kann auf komplexere Strömungsprobleme wie, zum Beispiel, Simulation eines statischen Mischers mit bewegten Adsorbenspartikeln, angewandt werden.

Auf der Mikroskala wird ein Modell zur genauen Berechnung homogener Misch- und Reaktionsprozesse für chemische Spezies mit niedriger Diffusivität entwickelt. Simulationen laminarer Strömungen zeigen, dass unbeachtete Batchelor-Skalen erhebliche numerische Diffusion verursachen können, was die Ausbeutevorhersage verfälscht. Selbst unter laminaren Bedingungen erzeugen sekundäre Strömungsstrukturen hohe Scherbeanspruchungen, die eine spezielle Behandlung der Transportgleichungen erfordern, wozu eine Stabilisierung basierend auf der Schmidt-Zahl eingeführt wird. Eine künstliche Diffusion, skaliert mit einer vordefinierten Stabilisierungs- oder turbulenten Schmidt-Zahl, stabilisiert die Simulationen bei gleichzeitig minimalen nichtphysikalischen Effekten. Das Modell wird mit der LBM diskretisiert und gegen experimentelle sowie numerische Daten aus einem laminaren reagierenden T-Mischer-Benchmark validiert, wobei eine höherauflösende Reproduktion des Modells auf einem äquidistanten LES-Gitter erfolgt. In turbulenten Strömungen wird die Impulsgleichung durch ein Subgrid-Scale-(SGS)-Turbulenzmodell erweitert, während die Tranasportgleichung die gleiche Stabilisierung wie im

laminaren Fall verwendet. Ein Mikromischer mit kollidierenden Jets dient als turbulentes Anwendungsbeispiel.

Auf der Nanoskala liegt der Fokus auf der Phosphatkristallisation in den Nanoporen der CSH-Mikropartikel. Hierzu wird ein reaktives Navier-Stokes-Poisson-Nernst-Planck-Gleichungssystem (RNSPNPE) entwickelt, das drei reagierende ionische Spezies in einer bewegenden Trägerflüssigkeit unter Einfluss eines dynamischen elektrischen Feldes mithilfe eines zeitadaptiven Splitting-Verfahren modelliert und mit LBM diskretisiert wird. Zur Sensitivitätsanalyse wird zusätzlich ein Verfahren der algorithmischen Differenzierung (AD) verwendet. Der vollständige Löser wird schrittweise anhand analytischer Lösungen validiert, wobei die AD-Ergebnisse gegen eine Sensitivitätsanalyse mit der Finite-Differenzen-Methode (FDM) verglichen werden. Das RNSPNPE-System wird in ein Framework integriert, das speziell für die Untersuchung von Kristallisationsprozessen in nanoporösen Geometrien entwickelt wurde. Eine der zentrale Neuheiten dieser Arbeit ist die Erweiterung des LBM-basierten physikochemischen Lösers um ein AD-Algorithmus. Die Methodik ermöglicht integrierte 2D- und 3D-Simulationen komplexer Nanoporen, in denen elektrochemische, hydrodynamische und kristalline Vorgänge sowie Sensitivitätsanalysen gleichzeitig betrachtet werden. Die untersuchte Reaktion ist die Bildung von Octa-Calcium-Phosphat (OCP) innerhalb von CSH. Mithilfe von AD werden vereinfachte 2D-Modelle offener und geschlossener Poren sowie ein 3D-μCT-Scan eines porösen Gesteins untersucht, um den Einfluss des elektrischen Oberflächenpotentials, der Porengröße, Strömungsgeschwindigkeit und Ionenkonzentration auf die OCP-Übersättigung zu analysieren. Simulationen zeigen, dass lange, enge Blindporen mit hohem elektrischem Oberflächenpotetnial die OCP-Kristallisation begünstigen und dass größere Geometrien mit weit verzweigten Porennetzen höhere Ionenkonzentrationen in ihrem Zentrum als die kleineren Systeme akkumulieren.

Zusammenfassend, der in dieser Arbeit vorgestellte multiskalige Modellierungsansatz bietet ein robustes und flexibles Simulationsframework zur Optimierung von Phosphatkristallisationsprozessen. Die entwickelten Modelle legen das Fundament für eine multiskalige Optimierung von Kristallisatoren und liefern wertvolle Erkenntnisse über die unterschiedlichen Skalen des P-RoC-Prozesses. Damit leistet diese Arbeit einen Beitrag zur Entwicklung nachhaltigerer Verfahren in der chemischen Verfahrenstechnik.

Abstract

Phosphorus is one of the most important chemical elements used in agriculture and the chemical industry. However, existing phosphorus resources may not be sufficient to meet current industrial demands. Therefore, it is essential to develop efficient methods for recovering phosphorus from alternative sources, such as wastewater, which remains a largely untapped global reservoir. One promising solution is the P-RoC process (*Phosphorus Recovery from Wastewater by Crystallization*), an advanced wastewater treatment technology developed at the Karlsruhe Institute of Technology (KIT). In this process, dissolved phosphate in wastewater crystallizes on calcium silicate hydrate (CSH) microparticles within a stirred tank reactor. To make this technology viable for practical applications, its efficiency must be improved. Unfortunately, limited knowledge exists regarding phosphate crystallization under dynamic conditions, and a detailed understanding of the crystallization process at the nanoscopic pore level within the microparticles is also lacking. This thesis aims to address the questions, which process parameters can be optimized in a stirred tank crystallizer, and how can species mixing, reaction, and pore-level crystallization be accurately predicted and influenced.

For that, a multiscale solution approach is then introduced, outlining the primary steps of the numerical analysis. This approach focuses on modeling the full-scale crystallization reactor at the macroscale, heterogeneous and homogeneous mixing and reaction processes at the microscale, and resolved transport and crystallization phenomena at the nanoscale. Fluid-structure interaction (FSI) aspects involving the motion of resolved particles or the reactor impeller are not considered. At all scales—excluding FSI scenarios—an Eulerian multiphase multicomponent modeling approach is employed due to the continuity of each phase and component within the models. To resolve simulations at the required level and efficiently process the generated meshes on highly parallel machines, the Lattice Boltzmann Method (LBM) is chosen as the discretization strategy. Foundational theory on the employed modeling and discretization techniques is presented, and the defined open questions are systematically addressed across

all three length scales. All models built this thesis are implemented in the *OpenLB* open source software library and can be reproduced by reviewing the Git commits or by compiling the example cases provided in the published repository. Descriptions of some setups are provided in the appendix of this thesis.

At the macro-level, the full-scale reactor is modeled. CSH microparticles, phosphate species, and particle loading are treated as continuous Eulerian phases. Heterogeneous reaction kinetics are modeled via the Linear Driving Force (LDF) method, using experimentally derived adsorption isotherms and incorporating multiple mass transfer stages. Validation against analytical benchmarks, such as a batch reactor and a fixed-bed reactor with mass transfer zone (MTZ) characteristics, confirms the model's reliability under low solid volume fraction conditions. This justifies the use of one-way coupling between the flow and species transport equations. This model represents the first simulation of adsorption on moving particles, which can be applied to more complex flow problems such as simulation of a static mixer with moving adsorbent particles.

At the micro-level, a simulation model is developed to accurately compute homogeneous mixing and reaction processes for low-diffusivity chemical species. Simulations of laminar flows reveal that unresolved Batchelor scales can lead to significant numerical diffusion, distorting yield predictions. Even under laminar conditions, secondary flow structures induce high shear stresses that necessitate special treatment of the transport equations using Schmidt number-based stabilization. Artificial diffusion, scaled with a predefined stabilization or turbulent Schmidt number, is introduced to stabilize the simulations while minimizing non-physical effects. The simulation model is discretized using LBM and validated against both experimental and numerical results from a laminar reactive T-shaped micromixer benchmark. The benchmark is re-established with higher accuracy using a fine, LES-scale, equidistant mesh. In turbulent flows, the momentum conservation equation is extended using a subgrid-scale (SGS) turbulence model, while the species transport equations retain the same stabilization scheme as in the laminar case. A micromixer with confined impinging jets is used as a turbulent flow application example.

At the nano-level, the focus is on phosphate crystallization within the nanopores of CSH microparticles. A reactive Navier-Stokes-Poisson-Nernst-Planck equation (RNSPNPE) system is developed for modeling three ionic species in a

moving carrier fluid under the influence of a dynamic electric field. A time-adaptive splitting approach is introduced to decouple the system for LBM discretization. Additionally, an algorithmic differentiation (AD) approach is implemented to calculate parameter sensitivities. The complete solver is validated stepwise using analytical solutions, and the AD results are benchmarked against those from a finite difference method (FDM) sensitivity analysis. This work integrates the RNSPNPE system into a framework specifically designed to investigate crystallization processes in nanoporous geometries. The model couples fluid flow, electric potential, and ion transport in a reactive environment. A novel contribution of this thesis is the integration of sensitivity analysis algorithms into the LBM-based physicochemical solver, extending LBM beyond traditional fluid dynamics to a powerful tool for sensitivity analysis. This solver can also be applied to other nanoscale and microscale chemical electrohydrodynamics processes. The developed methodology enables the first integrated simulations of complex 2D and 3D nanopore systems that involve electrochemical, hydrodynamic, and crystallization phenomena, along with sensitivity analysis. The specific phenomenon analyzed is the formation of octa-calcium phosphate (OCP) within CSH. Using AD, simplified 2D models of open and blind pores, as well as a 3D μCT scan of a porous rock, are examined to study the effects of surface electric potential, pore dimensions, carrier fluid velocity, and ion concentrations on OCP saturation. According to simulation results, long, narrow blind pores with higher surface electric potential promote OCP saturation. Additionally, larger geometries with more extensive pore networks accumulate higher ion concentrations in their centers compared to smaller systems.

In conclusion, the multiscale modeling approach presented in this thesis provides a robust and flexible simulation framework for optimizing phosphorus crystallization processes. The developed models lay the groundwork for multiscale optimization of crystallization reactors and contribute valuable insights into the various scales of the P-RoC process, advancing the pursuit of more sustainable chemical engineering practices.

Contents

1 Introduction

1.1 Phosphorus recovery from wastewater

Phosphorus is an essential and irreplaceable nutrient, mainly used as fertilizer in agriculture. Due to limited natural phosphate resources and the lack of domestic reserves in Germany, the recovery of phosphorus from wastewater and sewage sludge has become increasingly important. Since 2017, phosphorus recovery has been a legal requirement in Germany under the Sewage Sludge Ordinance [1].

The P-RoC process (*Phosphorus Recovery from Wastewater by Crystallization*), developed at the Karlsruhe Institute of Technology (KIT), provides a promising solution [2]. In this semi-continuous process, calcium silicate hydrate (CSH) particles are placed in a stirred reactor with phosphate-rich wastewater from sludge dewatering. Phosphate binds to the particles as the wastewater flows through, while a sieve retains the CSH material. Once the particles reach saturation, the reactor contents are transferred to a sedimentation tank, where the sediment is dried and used as fertilizer.

The P-RoC process can recover up to 30% of the initial phosphorus load in the influent according to the current state of the art, and the crystallized product contains up to 13 wt% phosphorus [3]. However, modifications are necessary to ensure economic viability. Under typical operating conditions, recovery rates range from 15% to 25% [4].

To perform such modifications, the crystallization process in the stirred reactor should be investigated in detail and optimized based on the results of these investigations. Investigations in this thesis are focused on a selection of knowledge gaps defined further.

1.2 Open questions of P-RoC process

To fully exploit the benefits of phosphorus recovery using the P-RoC process and to increase the efficiency of phosphate crystallization in the stirred tank reactor, it is essential to understand the influence of dynamic processes on the growth of phosphate loading in CSH particles. However, there is currently a lack of knowledge about these interactions that allow prediction and optimization of operating parameters. So, the first challenge of the current thesis is to

- *describe the dynamic dependencies of the multiphase moving system in the crystallization reactor with the crystallization process occurring in the CSH microparticles to enable optimization of the P-RoC process.*

Because the concentration of phosphate in the immediate vicinity of the CSH particles is subject to dynamic changes as a result of flow conditions, it cannot be assumed that the reaction is in equilibrium. Until now, a linear reaction kinetic model was generally assumed [5]. These findings are based on the results of the experiments, which are, in the case of microparticles, integral values observed at the macro-level and do not give insights into the processes at the pore-level. That is why the next challenge will be

- *representation of the dynamic crystallization process at the scale of microparticles and their pores where investigation of each process step is possible and identification of the most important parameters influencing crystallization.*

After naming these two global challenges, more concrete and specific questions must be defined to be answered in this thesis.

Q1 Wich crystallization process parameters are significant and can be optimized by a stirred tank crystallization reactor?

Q2 Reaction happens at the level of microparticles within their nanopores, so how can species mixing and reaction be correctly predicted?

Q3 Which parameters influence the pore-level crystallization reaction?

Although there are only three questions, finding answers thereon is a multistep process considering crystallization from distinct points of view.

1.3 Multiscale solution approach

The attempt to find answers to the questions from the previous Section will be realized through numerical analysis, which is much cheaper and faster than experiments and allows one to look into much smaller scales than the existing measuring techniques [6]. The development of a numerical analysis consists of the following steps:

S1 Modeling and discretization

S2 Sensitivity assessment and optimization

S3 Reduced-order model

The first step **S1** includes the composition of a mathematical equation system describing separate processes occurring in the considered apparatus, which need to be specified in advance. In terms of computational fluid dynamics (CFD) the simulation models consist primarily of Navier–Stokes equations (NSE) with distinct modifications and extensions depending on the concrete case. The discretization is reformulating the composed not always solvable NSE into solvable equations whose solution approximates the theoretical solution of the NSE. There exist different methods of this transformation, by which all of them are applied to a mesh in which the volume of the apparatus is divided. The second step **S2** is the scheme to calculate the dependencies of the built-up system on the chosen set of parameters, which can then be used in optimization. The sensitivities with respect to specific parameters are used to update them in the direction of the desired change of target parameters. To use the acquired knowledge in a faster way, a reduced-order model for the current problem can be derived in **S3**.

Each of these analysis steps contains three *substeps* necessary to proceed with accurate results to the next step:

Sx.1 Implementation

Sx.2 Validation

Sx.3 Application

Each step **S1–S3** must be performed for actually evaluating on computers in the form of a code during the implementation substep. In the current thesis, it

will be done within the *OpenLB* open-source software library. Descriptions of some code parts used for these implementations are given in the Appendix A.2. The models built up in the **S1–S3** main steps must be validated on analytical, numerical, or experimental results in the validation substep. After that, they can be applied to the regarded problem in the last substep.

At first, crystallization in a stirred tank reactor is regarded at the fully macroscopic scale to give answers to the first question **Q1**.

1.3.1 Crystallization process at the macro-level

Optimization of the crystallization stirred tank reactor requires considering the whole reactor volume with the reaction occurring inside of the moving microparticles. To model such a reactor, the following processes should be considered (Figure 1.1).

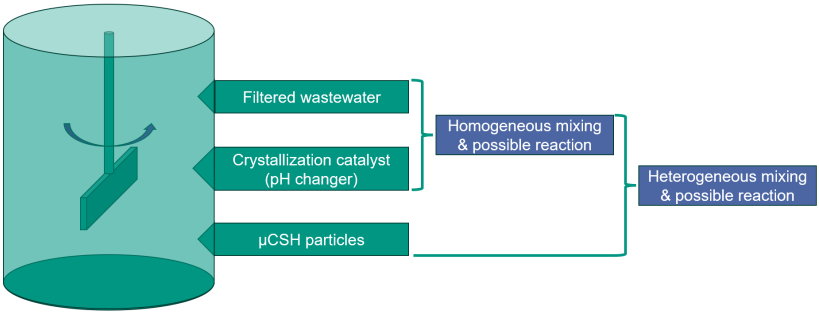

Figure 1.1.: Crystallization stirred tank reactor with participating components and subprocesses involving these components, as considered in the current thesis.

The vessel possesses a rotating impeller that can mix the suspension inside in laminar or turbulent regimes. The suspension consists of a liquid mixture and solid CSH microparticles. The mixture contains pre-filtered wastewater and possible liquid catalysts to adjust the pH factor and enhance calcium dissolution as mentioned in [5]. The mixing process and possible reactions or ions exchange occurring in the liquid can be regarded as homogeneous. The interaction of liquid with solid particles is a heterogeneous process. All these points should be taken into account in the resulting macroscopic reactor

simulation model. Speaking about the fluid flow driven by the rotating impeller in the sense of a model, a fluid-structure interaction solver with turbulence modeling in bulk and at the moving and stationary walls should be designed, which is beyond the scope of the current thesis.

First, only a pressure gradient driven fluid with dissolved adsorbate and adsorbent is considered, wherein adsorption takes place. At the macroscale, it is impossible to resolve the interface of particles and fluids and, in some sense, a volume average is needed [7]. Describing all components with an Euler-Euler model can solve this requirement. The adsorption process is a heterogeneous process between the continuously transported dissolved phosphate and the unresolved continuous particulate CSH microparticles-phase. Thereby, phosphate-to-CSH adsorption consists of multiple mass transport steps that occur between the bulk and particle pores:

1. Migration of reacting ions from bulk to the pore entrance (diffusive, hydraulic and electric transport),
2. Migration of ions through pore volume (diffusive, hydraulic and electric transport),
3. Contact of ions with pore wall leading to dissolution of calcium cations,
4. Saturation of reactants at the soil surface,
5. Distinct nucleation of the adsorbate ion based crystal at the point with most appropriate conditions (saturation product above one and low surface tension),
6. Growth of the crystal.

These steps cannot be resolved in the case of subgrid Eulerian particulate phase modeling, which is why they should also be modeled more generally mathematically, namely in the form of film, surface, and pore diffusion in addition to the crystallization itself. This reaction is macroscopically realized in the form of standard linear, Langmuir, or Freundlich sorption isotherms.

To come as close as possible to the microscale where mixing and reactions are occurring and to reproduce correctly flow structures of the specie transport equations in the case of full-size reactor simulation, fine grid cell sizes and processing of high cell numbers are required. The Lattice Boltzmann methods (LBM) have some unique advantages with respect to parallelization compared to traditional NSE solvers (FVM, FDM, FEM), such as their simple structure

and ease of algorithm [8–10]. In addition to this macroscale model, in the subsequent simulations, LBM is used as a discretization method because of the large meshes (sometimes more than 10^8 cells) needed for accurate results repeated several times according to the number of discretized equation systems.

Only a few examples of the combination of an Euler-Euler approach to particle and adsorption modeling exist. Peng *et al.* [11, 12] have used LBM to simulate adsorption in clusters of unresolved particles with a constant particle density. Maier *et al.* [13] have done work on adsorption on moving particles but with a Euler-Lagrange approach. Ma *et al.* [14] have chosen a similar approach to the one taken in this thesis in simulating adsorption using volume averaging but with a multiple relaxation time model. Their work was restricted to simpler kinetics, only applied to a fixed-bed reactor, and did not provide any data on the convergence of their method, which is missing for a fully validated approach.

An adsorption model based on the linear driving force model (*LDF*) with transport equations in the form of the advection-diffusion equation (*ADE*) for moving particles, dissolved solute, and particle loading with multiple mass transport mechanisms combined together with distinct adsorption isotherms and discretized with LBM has been missing. In this thesis, such a model is built (**S1.1**) and validated on examples with analytical solutions like ideal batch and fixed-bed reactors (**S1.2**). The model is then applied to a static mixer with moving particles (**S1.3**). From this model, parameters important for the adsorption efficiency can be defined to perform sensitivity analysis and optimization (**S2**).

1.3.2 Mixing and reaction at the micro-level

To answer **Q2** it is important to consider the interaction of species at the microparticle level. To do so, a reliable model should be found. The flow in the stirred tank crystallization reactor can exist in local laminar and turbulent regimes, by which the mixing and reaction processes proceed.

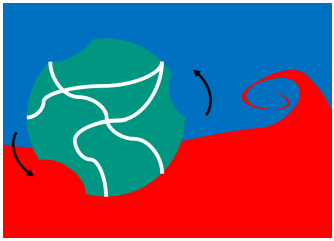

Figure 1.2.: Symbolic porous CSH microparticle in a flow with mixing chemical species (blue and red).

Figure 1.2 abstractly shows a flow around a CSH microparticle where two distinct chemical species are solved. Only one species or both, but with different efficiency, can build a chemical compound on the surface of the particle. In addition, ionic exchange can occur between the two species. For a correct prediction of the crystallization reaction in the microparticle, these species' interactions in the liquid should be accurately represented.

Estimation of the contact area between mixing species is a decisive factor in the calculation of mixing efficiency and reaction conversion. Due to computational power limitations, accurate tracking of the fluid structures that increase this area has been impossible until recently. Today, CFD allows for a precise calculation of flow behavior [15, 16]. The most reliable results are achieved by direct numerical simulation (DNS), considering a solution of the carrier fluid conservation equations, where the cell size is less than or equal to the finest length scale of the investigated flow structures. Even by a laminar mixing flow, there exist secondary flow structures, where the length scale is bounded from below by the Kolmogorov length scale, at which the kinetic energy of the vortex is dissipated into thermal energy due to the friction of the flow layers [17]. The concentrations of species transported by the microflow form smaller structures within the vortex of the carrier fluid. Therefore, in order to accurately simulate the mixing and reacting processes, a finer cell size is required than the one given by the hydrodynamic length scale. Specifically, the simulation must resolve the Batchelor length scale, which is even smaller than the Kolmogorov length scale [18]. Taking into account that, the most existing micromixing simulations can be considered as LES and not accurate enough to understand the behavior of the transported species in the secondary flow structures.

An established benchmark for mixing and reactions at the microscale are micromixers that are widely used in precise chemical process technology due to their multiple advantages compared to macroscopic mixers and reactors. Specifically, the high aspect ratio of micromixers leads to microfluidic flow structures that enable efficient fluid mixing and better heat and mass transfer. Calculating the reacting micromixer requires the incorporation of fluid dynamics in conjunction with a chemical reaction mechanism [19]. In order to effectively control reactions within these reactors, it is crucial to have a comprehensive understanding of microfluidic mechanics, as short residence times do not impede the chemical reaction [20]. Micromixers are operated in the laminar regime with secondary flow due to their small geometry as well as in a turbulent regime.

One disadvantage of micromixers is the inherent complexity of their utilization at large industrial scales. Despite this, there exists a wide range of examples showcasing diverse applications of micromixers. Micromixers are used most frequently in laboratories for analysis, synthesis of various species, and process development [21, 22]. The production of fine chemicals with strict purity and quality requirements is done using micro-mixers [22]. In addition, micromixers have applications in the pharmaceutical industry for research purposes [23].

In the current thesis, a simulation model for microscopic mixing and reaction is built, based as well on the Eulerian continuous approach (**S1.1**). It is possible because of the assumption that the specie concentrations are relatively low and do not significantly change the density of the carrier fluid where they are solved. The model is then discretized with LBM and applied to a laminar T-micromixer, which benchmark is re-established by calculating the concentrations on an equidistant fine lattice close to the Batchelor scale (**S1.2**), which makes this simulation a uniform large eddy simulation (ULES) of the whole apparatus. Afterwards, a similar model with LES-wise represented carrier fluid dynamics is applied to a turbulent impinging jets micromixer [24] to test its stability there (**S1.3**).

1.3.3 Crystallization at the nano-level

The third question **Q3** stated in the Section 1.2 requires investigating the crystallization process at the scale where it is actually proceeding – inside of the microparticle pores that lie in the nanometer region [25]. Due to that

fact, simulations performed on the resolved pore volumes can be considered nanoscopic.

At the nano-level, simulation of the phosphate crystallization would allow one to model the above-mentioned adsorption steps (Section 1.3.1) explicitly without big simplifications and empiricism (Figure 1.3).

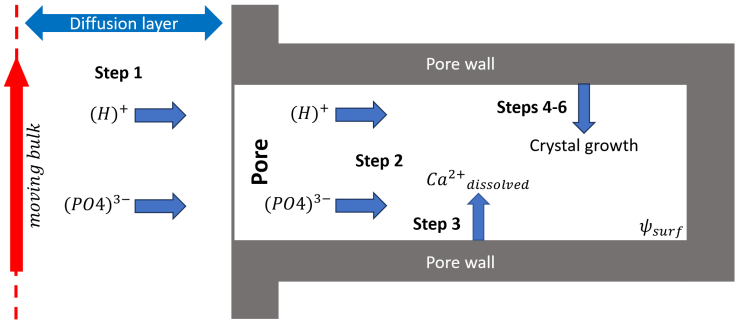

Figure 1.3.: Schematic pore-scale crystallization process. The step shown here are listed above in the Section 1.3.1.

The nanoscopic investigations of chemical processes have already been documented in the literature. Experimental and numerical studies (not CFD) demonstrated that the phosphate crystallization reaction starts with the dissolution of calcium cations from the surface of the CSH pores [26, 27]. Concrete leaching (similar reaction to calcium dissolution in CSH) at multiple scales was numerically simulated by Su *et al.* [28]. Considering adsorption-crystallization at the nanoscale, the electric potential plays an important role in the dynamics of dissolved ions in the vicinity of the pore surface. The incorporation of separate phosphate ions into the pore surface was modeled using the extended triple level method by Fukushi *et al.* [29]. The basics of nucleation and crystallization are explained in [30]. The ionic reaction with nucleation and crystallization at the microscale in an example of calcium carbonate crystal growth was experimentally investigated by Kim *et al.* [31].

In the context of CFD and LBM, general mineral precipitation in a porous domain with reactively changing porosity has been simulated by Ahkami *et al.* [32]. In the simulative publications, the Eulerian modeling approach has always been chosen, which is why in the current work at the nano-level it is

taken as well as at other modeling scales. Because of the reaction mechanism, the saturation product of octacalcium phosphate (OCP) as the precursor of hydroxyl apatite (HAP) plays the main role in the process. Until now, the sensitivity of the saturation product with respect to design parameters, like pore size, carrier fluid velocity, Helmholtz electric potential, and reacting ion concentrations, at the pore-level has not been analyzed.

In this thesis, such a dynamic electrochemical model coupled with a sensitivity assessing solver is built (**S1.1**, **S2.1**), validated (**S1.2**, **S2.2**), and applied to simplified 2D and realistic 3D porous geometries (**S1.3**) including the sensitivity analysis with respect to the parameters named above (**S2.3**). After extending the model with crystal nucleation and growth schemes, the resulting sensitivity analysis model will enable optimization and parameter identification based on known crystal volume values.

1.3.4 Connecting the scales

To get a unified image of the crystallization reactor and all the steps needed to be carried out to obtain a complete reactor optimization model, the following plot can be constructed (Figure 1.4). The steps on the vertical axis are already explained in the beginning of Section 1.3. These steps should be applied to the cases described in the three Subsections before. At the nanopore-scale, the resolved crystallization model will deliver dependencies of the final crystal volume and its development dynamics, which can be formulated as a reduced-order model that can be used at the higher scales (**App. 4**). The homogeneous mixing and reaction processes at the micro-level should be computed correctly with an appropriate model to give an accurate species distribution around the microparticles (**App. 3**). These microparticles can be modeled as moving resolved porous bodies at the mesoscale between micro- and macro-levels (**App. 2**). The reduced-order model of the pore-scale crystallization can be used in the simulation of porous full-size particles, the number of which can be modeled using a fluid-structure interaction approach. By considering multiple resolved particles, their collision behavior in dependence on the carrier fluid flow regime can be defined. Finally, at the macroscale, the particles are regarded as a continuous phase as well as the dissolved species (**App. 1**). The particles' behavior from the previous stage with their collision frequency can be expressed as a diffusion coefficient for the particle transport equation. The novel reaction kinetics and mixing process insights can be as well incorporated

into the macroscale simulation. In a stirred tank reactor, the interaction with a rotating impeller and eventually needed turbulence modeling should be considered as well.

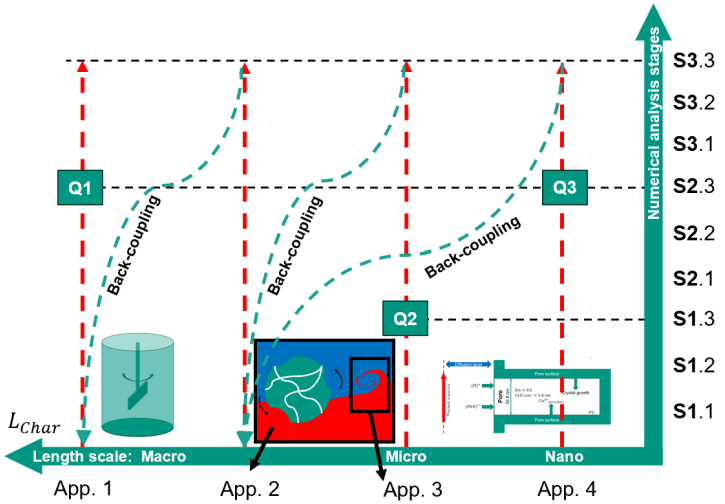

Figure 1.4.: Numerical analysis steps for building of a multiscale simulation model of the crystallization stirred tank reactor with main questions (Q1–Q3). Main steps (Y-axis): S1 – Modeling and discretization. S2 – Sensitivity assessment and optimization. S3 – Reduced-order model. Substeps (Y-axis): 1. Implementation. 2. Validation. 3. Application. Partial application cases for representation of the reactor (X-axis): App. 1 – Heterogeneous mixing and reaction on subgrid particles. App. 2 – Heterogeneous mixing and reactions on resolved particles. App. 3 – Homogeneous mixing and reaction in bulk. App. 4 – Surface reaction in resolved nano-pores.

1.4 Structure of the thesis

After the definition of approaches for answering the main questions, the structure of the thesis can be explained (also marked in Figure 1.4). All built models are based on the Eulerian multiphase or multicomponent approach, that is why firstly in the thesis the basic theory of Eulerian flow modeling with corresponding assumptions and restrictions is revealed (Chapter 2). Subsequently, the basics of LBM and an overview of existing multiphase LBM techniques

are given **based on [33]**. Afterwards, the validation methodology for the simulation model is explained.

Macro-level: As mentioned before, to find an answer to the first question (**Q1**), a macroscopic simulation model with the Eulerian method is presented (Chapter 3). The crystallization process is modeled at the macro-level at the subgrid-scale solid particles using adsorption approximation for reaction kinetics and the concept of driving force with different diffusion steps, **based on [34]**. This model is also validated on analytical solutions and applied to different reactor types.

Micro-level: In Chapter 4, question **Q2** is answered. Thereby, an Eulerian model discretized with LBM for microscale mixing and homogeneous reaction processes is created. This simulation model is validated on a laminar T-micromixer (Section 4.2, **based on [35]**) re-establishing the benchmark results, and also this model is applied to a turbulent micromixer with confined impinging jets (Section 4.3).

Nano-level: To find the parameters important for phosphate crystallization and their influence at the pore level (**Q3**) the phosphate diffusion into pores and OCP saturation at the pore surface are modeled in resolved nanoscopic pore volumes. For its investigation, an Eulerian solver coupled with a sensitivities calculation is built up and validated on analytical examples (Section 5.1, **based on [36]**). The saturation behavior of OCP in the nanopores of CSH is then investigated with an analysis of the sensitivities in simplified 2D and realistic 3D geometries (Section 5.2, **based on [37]**). The influences of carrier fluid velocity, surface electric potential, concentrations of reacting ions in bulk, pore width and depth, as well as the size of the chosen simulation domain are defined.

2 Basic theory and notation

This Chapter takes some contents from the publications 1, 2, 3, 11, 12, 13 listed in Appendix A.3.

In this Chapter, all the used model equations and LBM discretization techniques are described. The Chapter starts with the most important characteristic numbers in the current thesis, followed by single and multi-phase Eulerian models. After that, a discussion of LBM basics, LBM boundary conditions, and LBM approaches for multiphase models is given. The Chapter is concluded with validation methodology for simulation models.

2.1 Continuous Eulerian flow modeling

At the three spatial scales, even at the nanoscale, depending on the mean free path of the investigated species or the characteristic length of the transported particles, the assumption of a *continuous medium* can be met. This means that in the smallest taken control volume, there is a sufficient number of particles, allowing one to consider averaged characteristics of the behavior of the particles [38]. In the case of a continuum, Eulerian modeling approach is applicable to all three scales. Eulerian NSE for mass, momentum, and energy conservation can be used at these scales by adding some modifications, e.g. Knudsen diffusion by resolutions finer than the distance between two molecules at the nanoscale or momentum exchange forces by unresolved two-phase flows at the macroscale. This method is also perfectly suitable for the simulation of transported quantities, such as the concentration of chemical species or volume fraction of subgrid-scale second-phase particles, by applying an ADE. Even granular flows consisting of solid moving particles can be described with a modified Eulerian ansatz, which considers the solids as a continuous flowing phase with a special term for viscosity. From a modeling perspective, the Eulerian description of a process is identical at all regarded scales until the

additional terms appearing by coarse-graining or refinement of the control volume over the Knudsen limit.

2.1.1 Characteristic length scales and numbers

The first requirement for the Eulerian flow modeling is a valid continuum assumption for the considered control volume. It can be characterized by the cell *Knudsen number Kn*, which compares the distance that one molecule can freely move till collision with another molecule, also defined as *mean free path (MFP)* λ with the cell size $\triangle x$ [39]

$$\mathrm{Kn} = \frac{\lambda}{\triangle x} = \frac{(NQ_{\mathrm{cs}})^{-1}}{\triangle x} = \frac{M}{\rho N_{\mathrm{A}} \pi d_{\mathrm{m}}^2 \triangle x}. \tag{2.1}$$

The MFP can be computed from the number density of molecules $N = \frac{\rho N_{\mathrm{A}}}{M}$ and the cross-sectional area $Q_{\mathrm{cs}} = \pi d_{\mathrm{m}}^2$. The Knudsen number determines what kind of flow (Eulerian or Lagrangian, continuous or discrete) can be considered from the chosen size of the control volume. This flow type says how it behaves in the bulk and on boundaries depending on the chosen observation perspective. According to the theory of gas kinetics, there are several flow regimes depending on the Knudsen number (Figure 2.1):

- free molecular flow ($\mathrm{Kn} > 10$)
- transitional flow ($0.1 \leq \mathrm{Kn} \leq 10$)
- slip flow ($0.01 \leq \mathrm{Kn} \leq 0.1$)
- continuum flow ($\mathrm{Kn} < 0.01$)

After considering Knudsen diffusion for bulk flow and effects such as thermal creep and partial slip at the boundaries, NSE can even be applied for flow modeling in the transitional regime [40].

For complex reactive CFD modeling at the nano-level, as is done in Chapter 5 of the current thesis, understanding the flow regime depending on the chosen simulation grid size is one of the most important criteria for physical plausibility.

After MFP, the next important characteristic that influences the selection of an appropriate grid resolution for modeling chemical reactions and mixing

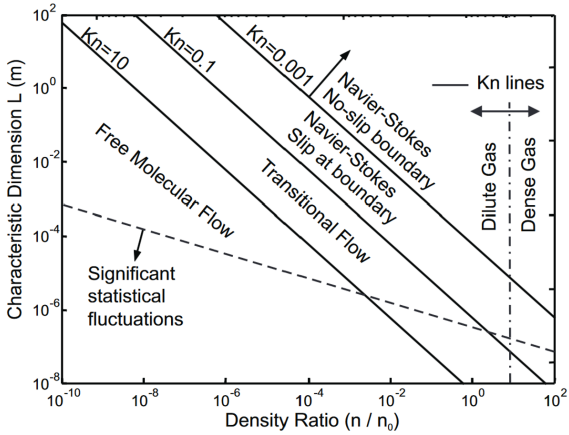

Figure 2.1.: Flow regimes of a gas depending on Knudsen number. n_0 is the reference number density by standard conditions [39].

processes is the *Batchelor length scale* [18]. This scale describes the size of the smallest fluctuations of a transported scalar (chemical species concentration, temperature, volume fraction, and others). In contrast to flow velocity fluctuations, the vortices built by resolved species can be much finer depending on the species diffusion constant D. Mathematically, Batchelor scale η_B is defined in relation to the Kolmogorov length scale η (explained further):

$$\eta_\mathrm{B} = \frac{\eta_\mathrm{K}}{\sqrt{\mathrm{Sc}}}. \tag{2.2}$$

This relation factor $\mathrm{Sc} = \frac{\nu}{D}$ is the *Schmidt number* [41], which represents the ratio of the kinematic viscosity of the carrier fluid $\nu = \frac{\mu}{\rho}$ to the diffusivity of the species. For $\mathrm{Sc} \geq 1$ the Batchelor scale is smaller than the Kolmogorov scale and the scalar vortices are then also finer than those of the carrier fluid flow. By thermal flow simulation, instead of the Schmidt number, the *Prandtl number* is used $\mathrm{Pr} = \frac{\nu}{\alpha_\mathrm{T}}$ which sets the viscosity in relation to the thermal diffusivity α_T [42].

By choosing the control volume size, η_B says after which vortex diameter the scalar interface vanishes and the region becomes fully mixed. Below this limit, in the case of numerical modeling, there is no numerical diffusion and no artificial production of scalar in the control volume. By coarser resolutions

that do not resolve the scalars' eddies, the numerical diffusion appears and grows depending on the difference between the cell size and Batchelor length scale.

In case of a chemical reaction like addition as in this thesis (Section 4.2), with coarser resolutions, the extent of the reaction becomes much higher due to the numerical diffusion of reactants and does not represent the experimental values.

The next important length scale in terms of CFD is the *Kolmogorov length scale*, which defines the smallest diameter of a carrier flow vortex, beneath which the kinetic energy becomes thermal due to friction and the eddies are resolved [17]

$$\eta_{\mathrm{K}} = \left(\frac{\nu^3}{\epsilon_{\mathrm{TKE}}}\right)^{\frac{1}{4}} \text{ with } \epsilon_{\mathrm{TKE}} = \frac{1}{2}\nu \sum_{\alpha,\beta} (\partial_\alpha u'_\beta + \partial_\beta u'_\alpha)^2, \tag{2.3}$$

$$u'_\alpha = u_\alpha - u_\beta. \tag{2.4}$$

Here, ϵ is the dissipation rate of the turbulent kinetic energy at which it is transformed into thermal energy.

By choosing a control volume size smaller than η, all the vortexes that appear are fully resolved, and the velocity profile is represented correctly. By coarser resolutions, the eddies are not resolved and the accuracy of the calculation is degraded, which is why some mathematical corrections are needed. There are multiple turbulence models that approximate the impact of unresolved eddies by local addition of turbulent viscosity, which represents the resistance of a turbulent eddy to the surrounding flow.

As follows from the turbulent kinetic energy dissipation rate formulation, with increasing velocity the Kolmogorov scale becomes smaller, which makes computation of a complete hydrodynamical apparatus resolving all vortexes in most cases impossible. That means for reactive flows simulation at the macro-level that special modeling is needed for carrier fluid turbulence as well as for numerical diffusion of transported species.

To estimate how turbulent the flow is and what kind of additional turbulence modeling in the bulk and at the boundaries is required, besides the Kolmogorov length scale the *Reynolds number* Re should be defined

$$\mathrm{Re} = \frac{UL}{\nu}. \tag{2.5}$$

In contrast to variables taken from the local control volume in previous characteristics, here the U and L are the characteristic velocity and the characteristic length assumed in each concrete case. For example, in a channel flow, L would be the hydrodynamic diameter or, by flow around an obstacle, L would be the size of this obstacle. Similarly to the Knudsen number, according to the Reynolds number, different flow regimes can be defined [43]:

- laminar flow ($\mathrm{Re} < 2300$)
- transitional flow ($2300 \leq \mathrm{Re} \leq 4000$)
- turbulent flow ($\mathrm{Re} > 4000$)

In the fully laminar regime, there exist no velocity fluctuations, which is why no special modifications to conservation equations are needed. Starting from a transitional flow, different turbulence modeling and simulation stabilization approaches are required depending on the chosen spatial resolution.

An interesting point is that even in laminar flows, there can be secondary circulating flow, where a transported scalar can build strong vortices at higher Schmidt numbers. This is the case in a micromixer, which is simulated in the current work.

This phenomenon of transported scalars can be characterized by *Peclet number* $\mathrm{Pe} = \mathrm{Re} \cdot \mathrm{Sc}$ or $\mathrm{Pe} = \mathrm{Re} \cdot \mathrm{Pr}$ for thermal flows. The regimes according to the Peclet number are [44]:

- diffusion dominated flow ($\mathrm{Pe} \ll 1$)
- transitional flow ($\mathrm{Pe} \approx 1$)
- advection dominated flow ($\mathrm{Pe} \gg 1$)

By advection-dominated flows, the arising inner scalar vortices are highly probable.

Finally, the last relation that will bring us back to the Knudsen number is the connection between the Knudsen number and the Reynolds number, also called the Von Karman ratio [39]:

$$\mathrm{Kn} = \frac{\mathrm{Ma}}{\mathrm{Re}} \sqrt{\frac{\gamma_\mathrm{T} \pi}{2}}, \tag{2.6}$$

where $\mathrm{Ma} = \frac{U}{c_\mathrm{s}}$ is the *Mach number* (the ratio of the characteristic velocity to the speed of sound) and γ_T is the specific heat ratio.

The named dimensionless numbers (Kn, Re, Pe, $\mathrm{Sc}(\mathrm{Pr})$, Ma) can describe each flow and also define similar flows that provide the same variable values when considering them at the same scale.

2.1.2 Conservation transport equations

In the current thesis, the Eulerian modeling is considered, which means a continuum assumption for the transported variables in the control volume. In the models regarded here at all the scales, the conservation laws for mass and momentum in the *Navier–Stokes* form are taken for the description of flow behavior. So, for macroscopic variables density ρ, velocity $\boldsymbol{u}$, pressure p, and force $\boldsymbol{F}$, the following equations for a single-phase Eulerian flow can be written [45]:

$$\partial_t \rho + \boldsymbol{\nabla} \cdot (\rho \boldsymbol{u}) = 0, \tag{2.7}$$

$$\partial_t (\rho \boldsymbol{u}) + \boldsymbol{\nabla} \cdot (\rho \boldsymbol{u}\boldsymbol{u}^T) + \boldsymbol{\nabla} p = \boldsymbol{\nabla} \cdot \left[\mu \left(\boldsymbol{\nabla} \boldsymbol{u} + (\boldsymbol{\nabla} \boldsymbol{u})^{\mathrm{T}} - \frac{2}{3} (\boldsymbol{\nabla} \cdot \boldsymbol{u}) \boldsymbol{I} \right) \right] + \boldsymbol{F}. \tag{2.8}$$

In case of low Knudsen and Mach numbers, these NSE can be rewritten in the form of *incompressible NSE*:

$$\boldsymbol{\nabla} \cdot \boldsymbol{u} = 0, \tag{2.9}$$

$$\partial_t \boldsymbol{u} + \boldsymbol{\nabla} \cdot \boldsymbol{u}\boldsymbol{u} + \frac{1}{\rho} \boldsymbol{\nabla} p = \nu \boldsymbol{\nabla} \cdot (\boldsymbol{\nabla} \boldsymbol{u} + (\boldsymbol{\nabla} \boldsymbol{u})^{\mathrm{T}}) + \frac{\boldsymbol{F}}{\rho}. \tag{2.10}$$

By chemical reactions, transported unresolved particles, or temperature, an *ADE* is used, where the scalar s is moved by the advection velocity $\boldsymbol{u}_{\mathrm{ad}}$ and the diffusion constant D (or the thermal diffusivity). Additionally, a source or sink Q_s term can be inserted into the equation, which can represent the reaction term, heating point or something else:

$$\partial_t s + \boldsymbol{u}_{\mathrm{ad}} \cdot \boldsymbol{\nabla} s = D \triangle s + Q_s. \tag{2.11}$$

To describe the distribution of certain variables (e.g. electric potential or pressure by multiphase flows) the *Poisson equation (PE)* is considered:

$$\triangle s = Q_s. \tag{2.12}$$

This equation can be regarded as a specific form of ADE, where the temporal scalar derivative and the advection velocity are set to zero. The diffusion coefficient is also missing or considered to be one.

2.1.3 Subgrid-scale (SGS) turbulence modeling

For turbulent fluctuating flows and a larger cell size than the Kolmogorov length scale, *filtered NSE* are applied where small unresolved eddies are modeled by additional turbulent viscosity. Filtering velocity and pressure means their decomposition into the filtered parts $\bar{\boldsymbol{u}}$, $\bar{p}$ and the subgrid-scale parts $\boldsymbol{u}^{\mathrm{SGS}}$, p^{SGS} that contain the impact of the unresolved small turbulent structures

$$\boldsymbol{u} = \bar{\boldsymbol{u}} + \boldsymbol{u}^{\mathrm{SGS}} = G\boldsymbol{u} + \boldsymbol{u}^{\mathrm{SGS}}, \tag{2.13}$$

$$p = \bar{p} + p^{\mathrm{SGS}} = Gp + p^{\mathrm{SGS}}. \tag{2.14}$$

The application of some mathematical filter, such as a cut-off or Gaussian, is shown by multiplication of G to the unfiltered variable. The *filtered NSE* are now rewritten as [46]

$$\boldsymbol{\nabla} \cdot \bar{\boldsymbol{u}} = 0, \tag{2.15}$$

$$\partial_t \bar{\boldsymbol{u}} + \boldsymbol{\nabla} \cdot \bar{\boldsymbol{u}}\bar{\boldsymbol{u}} + \frac{1}{\rho}\boldsymbol{\nabla}\bar{p} = \nu \boldsymbol{\nabla} \cdot (\boldsymbol{\nabla}\bar{\boldsymbol{u}} + (\boldsymbol{\nabla}\bar{\boldsymbol{u}})^{\mathrm{T}}) - \boldsymbol{T}^{\mathrm{SGS}} + \frac{\boldsymbol{F}}{\rho}, \tag{2.16}$$

$$\partial_t s + \boldsymbol{\nabla} \cdot (s\bar{\boldsymbol{u}}) = D \triangle s + Q_s. \tag{2.17}$$

The SGS stress tensor $\boldsymbol{T}^{\mathrm{SGS}} = \overline{\boldsymbol{u}\boldsymbol{u}} - \bar{\boldsymbol{u}}\bar{\boldsymbol{u}}$ should be modeled with a mathematical approach using the already filtered stress tensor, so that

$$\boldsymbol{T}^{\mathrm{SGS}} = -\nu_t^{\mathrm{SGS}}(\boldsymbol{\nabla}\bar{\boldsymbol{u}} + (\boldsymbol{\nabla}\bar{\boldsymbol{u}})^{\mathrm{T}}). \tag{2.18}$$

Approximation of the turbulent SGS viscosity ν_t^{SGS} can be done in various ways; the most common one is the *Smagorinsky-Lilly* ansatz [47, 48] where the turbulent viscosity is computed from the norm of the strain rate tensor $\bar{\boldsymbol{S}}$:

$$\nu_t^{\mathrm{SGS}} = c_{\mathrm{s}} \triangle x^2 \sqrt{2\bar{\boldsymbol{S}}\bar{\boldsymbol{S}}}, \tag{2.19}$$

with Smagorinsky constant c_{s} [49]. The numerical approximation of these filtered equations that resolve only the large turbulent eddies is called LES.

The additional SGS viscous stress tensor is necessary not only from the mathematical consistency perspective but also in the sense of simulation behavior stability. Without this term, at higher Reynolds numbers and coarser grid resolutions, velocity gradients are so strong that the simulation starts to diverge. Adding the turbulent viscosity smooths these gradients and makes the simulation more stable.

2.1.4 Scalar transport in turbulent and strong shearing flows

It is often the case when the diffusion coefficient in an ADE is low ($D < 10^{-5}$ $\mathrm{m^2\,s^{-1}}$), where the simulation becomes unstable and diverges in cells experiencing high shear stress. To overcome this problem, a Smagorinsky–Lilly-type stabilization or turbulence diffusion model described above is applied [47, 48]. This idea was realized using LBM e.g. by Siodlaczek *et al.* [50] for the temperature distribution simulation coupled to a turbulent LES. In high shear stress regions, the artificial stabilization viscosity ν_{st} can be calculated with the Smagorinsky–Lilly model and transformed to the stabilization or turbulent diffusion D_{st}, which is added to the molecular one. This conversion is performed with the chosen Smagorinsky constant C_{S} and the *stabilization or turbulent Schmidt number* $\mathrm{Sc_{st}}$ for chemical species transport or the *stabilization or turbulent Prandtl number* $\mathrm{Pr_{st}}$ for temperature distribution calculation, which can take different values, depending on cell size. Further description refers only to the Schmidt number stabilization, but it is identical in the Prandtl number case. A higher Smagorinsky constant and a smaller stabilization number lead to stronger artificial diffusion used at coarser mesh resolutions. With $D_{\mathrm{mol},i}$ denoting the molecular diffusivity, the effective diffusivity D_i used in the simulation is computed as

$$D_i = D_{\mathrm{mol},i} + D_{\mathrm{st/t}}, \tag{2.20}$$

$$D_{\mathrm{st/t}}(\boldsymbol{x}, t) = \frac{\nu_{\mathrm{st/t}}^{\mathrm{SGS}}}{\mathrm{Sc_{st/t}}}. \tag{2.21}$$

With the described model, the effective D_i, see (2.20), becomes space-time dependent. Specifically, D_i increases where simulation stability is endangered due to a strong shearing counter-flow. In turbulent flows, the added diffusion can be regarded as physically based and related to the diffusion effects in the unresolved vortexes.

2.1.5 Eulerian multiphase modeling

Multiphase simulations are in high demand both in industry and in science, especially in the field of process technology, where complex reactions and phase transitions need to be calculated. Exemplary applications are liquid-solid,

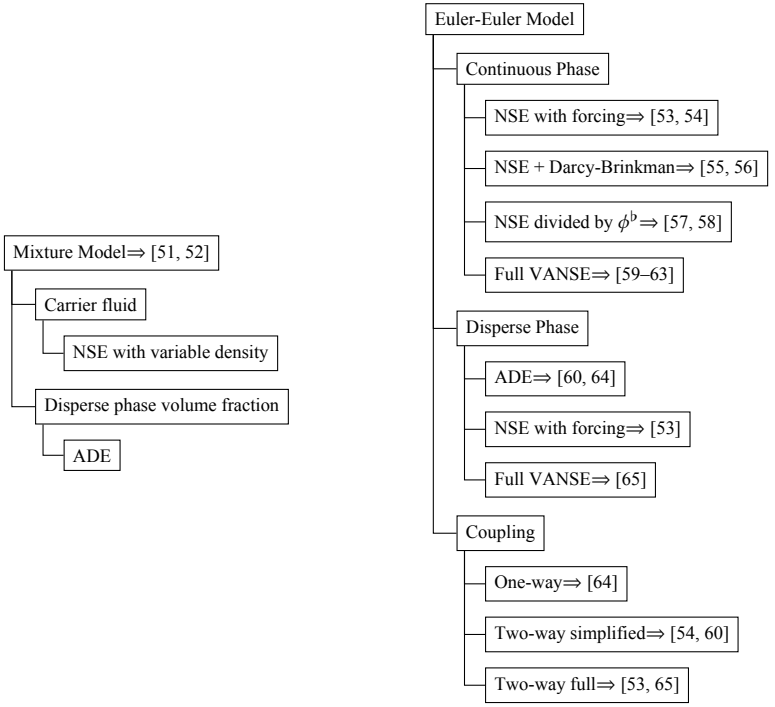

Figure 2.2.: Functional representation of the models for unresolved multiphase Eulerian flows with corresponding phasic equations and publications where they are used.

gas-solid, and gas-liquid reactors [66], phase separators, and transport units [67, 68].

Eulerian multiphase simulation schemes typically consider each phase as continuous and solve mass and momentum conservation equations for each of them.

Multiphase Eulerian models generally consider both phases as interpenetrating continua, whereby these phases can be presented by a single NSE system for mixture (*Mixture model*) or by separate equation systems (*Euler–Euler model*). The first option requires the solution of NSE with variable density, which is a combination of the phasic densities depending on the volume fraction solved in a separate ADE. In the other modeling method, both phases are

modeled with separate Eulerian systems. In that case, different options can be chosen for representation of the continuous phase, dispersed phase, and the coupling between them. For both phases, the VANSE are the starting point of modeling (Equations 2.26, 2.27), whereby the disperse secondary phase can be reduced to an ADE (Equation 2.11) where its concentration or number density is considered as a transported scalar.

For bubbly flows, Sokolichin *et al.* suggests using the Boussinesq force to exert influence on the dispersed phase and not using the volume fraction in the main part of the conservation equations under the assumption of low gas holdups under 10 % [54]. COMSOL code performs a manipulation with VANSE so that the void fraction exists only in the momentum exchange forces and the total mass equilibrium [53]. That model can be used for the whole range of gas holdups. In both cases, the VANSE is replaced by the standard NSE. A further approach for the continuous phase in a domain with volume fractions or porosities is the addition of the Darcy–Brinkmann term to the momentum equation. A further VANSE simplification with volume fraction only in velocity convection and pressure term was suggested by Nithiarasu *et al.*, whereby the volume fraction there should be constant in space and time [69].

Considering coupling between two phases, there exist three options:

1. *One–way* coupling for small volume fractions and particle radii [64], in which the information from the continuous phase is transmitted directly to the disperse phase without any response.
2. *Two–way simplified* coupling according to the proposal of Sokolichin *et al.* [54], where a response from the dispersed phase to the continuous one exists in form of a simple force.
3. *Two–way full* coupling with all momentum exchange forces as in [53, 65].

2.1.5.1 VANSE as multiphase Eulerian equation system

The coupling between phases can be performed by averaging the volume of the phase flow variables. The resulting VANSE [70] also involve the phase interaction forces in the momentum equation. In addition to multiphase flows, VANSE are suitable for the modeling of porous flows [71].

If subgrid particles are contained in the regarded control volume, any quantity of a fluid phase can be adjusted to the whole volume, which also includes these particles. Below, this adjustment is called volume averaging, denoted with $\langle\cdot\rangle$, and can be written as follows for any fluid quantity $s^\flat$, where $\flat$ indicates the corresponding phase.

Let V denote the entire cell volume and $V^\flat$ the volume which is occupied by phase $\flat$, hence

$$\sum_\flat V^\flat = V. \tag{2.22}$$

The ratio of these volumes is defined via the respective void fraction

$$\phi^\flat = \frac{V^\flat}{V}. \tag{2.23}$$

In the following, the volume-averaged scalars are denoted with $\widetilde{\cdot}$ and the volume-averaged vectors with $\overline{\cdot}$. Thus, for scalars s and vectors $\boldsymbol{s}$ the following is defined

$$\phi^\flat \widetilde{s^\flat} = \langle s^\flat \rangle \equiv \frac{1}{V} \int_{V^\flat} s^\flat \, \mathrm{d}V, \tag{2.24}$$

$$\phi^\flat \widetilde{\rho^\flat} \overline{\boldsymbol{s}^\flat} = \langle \rho^\flat \boldsymbol{s}^\flat \rangle. \tag{2.25}$$

By volume averaging all terms of the NSE, the VANSE are deduced [70, 72]

$$\partial_t(\phi^\flat \widetilde{\rho^\flat}) + \boldsymbol{\nabla} \cdot (\phi^\flat \widetilde{\rho^\flat} \overline{\boldsymbol{u}^\flat}) = 0, \tag{2.26}$$

$$\partial_t(\phi^\flat \widetilde{\rho^\flat} \overline{\boldsymbol{u}^\flat}) + \boldsymbol{\nabla} \cdot (\phi^\flat \widetilde{\rho^\flat} \overline{\boldsymbol{u}^\flat \boldsymbol{u}^\flat}) + \phi^\flat \boldsymbol{\nabla} \widetilde{p} = \nu \boldsymbol{\nabla} \cdot (\phi^\flat \widetilde{\rho^\flat} (\boldsymbol{\nabla} \overline{\boldsymbol{u}^\flat} + \overline{\boldsymbol{u}^\flat} \boldsymbol{\nabla})) + \phi^\flat \overline{\boldsymbol{F}^\flat}, \tag{2.27}$$

where $\widetilde{\rho^\flat}$ and $\overline{\boldsymbol{u}^\flat}$ denote the volume-averaged versions of the fluid density and velocity, respectively. The pressure $\widetilde{p}$ is common for all phases of the system.

2.1.5.2 Multiphase (VA)NSE-ADE models

Within this section, the (VA)NSE-ADE models for multiphase flow are presented. The works shown here use LBM discretization for built-up Eulerian models.

One-way coupling – Trunk *et al.* [64]
This work presented a NSE-ADE model for particulate flow (1–800 micron diameter spheres) in the tracheal bifurcation, as a cost-effective alternative to a well-established, but computationally exhaustive, Lagrangian model.

The continuous phase is described as in Eq. 2.7 and 2.8 whereby the back-coupling of the particulate phase to the main phase is ignored. Concerning the particulate phase—the way it is transported by the continuous fluid phase is determined by the Stokes number St, which is defined as the ratio between the particle's and fluid's response time and is evaluated as:

$$\mathrm{St} = \frac{\rho^{\mathrm{p}} \left(d^{\mathrm{p}}\right)^2 u^{\mathrm{c}}}{18 \nu^{\mathrm{c}} L}, \tag{2.28}$$

where d^{p} is the diameter of the particle and L is the relevant length scale of the domain. For $\mathrm{St} \gtrsim 0.1$ drag effects start to become relevant, and a delay occurs between the continuous phase's and dispersed phase's velocity. As such, $\boldsymbol{u}^{\mathrm{c}}$ in the ADE must be replaced with $\boldsymbol{u}^{\mathrm{p}}$, which must be determined from the drag force and Newton's second law. In this work, only the Stokes drag force $\boldsymbol{F}_{\mathrm{St}}$ was considered. Therefore, if the mass of a particle is defined as m^p:

$$m^{\mathrm{p}} \, \partial_t \boldsymbol{u}^{\mathrm{p}} = \boldsymbol{F}_{St} \left(\boldsymbol{u}^{\mathrm{c}}, \boldsymbol{u}^{\mathrm{p}}\right). \tag{2.29}$$

Artificial non-zero diffusivity ($D \sim 10^{-6}\ \mathrm{m^2\ s^{-1}}$) is applied to stabilize the ADE.

Two-way coupling for bubbly flows
In case of bubbly flows, the backcoupling can no longer be ignored. If the gas holdup is below 10%, the backcoupling can be approximated with a Boussinesq-like force [54]. This is implemented by adding an extra $\boldsymbol{F}_{\mathrm{B}}$ as the force term in equation 2.8:

$$\boldsymbol{F}_{\mathrm{B}} = -\phi^{\mathrm{p}} \rho^{\mathrm{c}} \boldsymbol{g}. \tag{2.30}$$

Höcker *et al.* [60]
Höcker *et al.* [60] modeled the Rayleigh-Taylor instability, where solid particles are evenly dispersed in the upper part of the domain at the start of the simulation. In the center of the interface between the pure water part and the particles-laden part, an instability is defined to initialize a flow. The dynamics of the carrier fluid is represented by VANSE (see Section 2.1.5.1), and the dynamics of the

dispersed phase is calculated with ADE. As a phase interaction force, Stokes drag was used. As a body force, standard gravity was chosen. Considering for water the Equation 2.27, following expression can be stated:

$$F = \rho \boldsymbol{g} + \phi^{\mathrm{p}} \frac{9\rho\nu}{2r_{\mathrm{p}}^2 \phi^{\mathrm{c}}} (\boldsymbol{u}^{\mathrm{c}} - \boldsymbol{u}^{\mathrm{p}}). \tag{2.31}$$

On the particle side, the particle velocity is computed using Eq. 2.29, where the sum of forces includes the Stokes drag (Eq. 2.31) and the buoyancy force $\boldsymbol{B} = \phi^{\mathrm{p}}(\rho - \phi^{\mathrm{p}} m^{\mathrm{p}})\boldsymbol{g}$.

2.2 Discretization in space and time

The Eulerian transport equations do not always have an analytical solution, which is why they are approximated numerically using various spatial and temporal discretization techniques.

To solve the Eulerian system numerically, there exist different methods in CFD, among them finite differences (FDM), finite volumes (FVM) or finite elements methods (FEM), which consider the equations always macroscopically and operate directly with variables from these equations. These methods are widely used and have gained popularity for their universality and adaptivity. The main disadvantage of those approaches is the complexity and sometimes implicitness of their algorithms, which limit the scalability of the calculations for large meshes. An alternative to the named approaches is the LBM. It can be regarded as the coarse-graining of Lagrangian molecular dynamics because this method is based on statistical consideration of gas kinetics. LBM is a mesoscopic approach that deals with particle distribution functions (PDF) that describe the position of molecules in space and time. Through mathematical expansion, LBM can approximate NSE with second–order consistency, whereby the moments of PDFs equal the macroscopic variables in NSE. LBM is a discretized version of the Boltzmann equation, formulated as a discrete velocity Boltzmann equation on a structured grid with a predefined set of streaming directions for molecules. In comparison to other calculation approaches, LBM is fully local and allows unlimited scaling on CPU-GPU HPC clusters for handling very large meshes [73].

2.2.1 LBM as kinetics-based discretization approach

Similarly to the mesoscale character of the Eulerian approach, the Boltzmann equation operates with statistical quantities that describe states of molecules in the velocity space, the molecular velocity distribution function or *PDFs* $f(\boldsymbol{x}, t, \boldsymbol{\xi})$ [74, 75]. Thereby, a volume dV where there is some number of molecules N that are moving with velocities between $\boldsymbol{\xi}$ and $\boldsymbol{\xi}+d\boldsymbol{\xi}$ is considered, so that:

$$f(\boldsymbol{x}, t, \boldsymbol{\xi}) = \frac{dN}{dV d\boldsymbol{\xi}}. \tag{2.32}$$

Boltzmann equation is derived from the conservation of particles in a control volume under the assumption of the Boltzmann-Grad limit [76], where particles are transported and which number is changed through molecular collision:

$$\frac{Df}{Dt}|Transport = \frac{Df}{Dt}|Collision. \tag{2.33}$$

through expanding of the transport term the *Boltzmann equation* can be written as:

$$\partial_t f + \boldsymbol{\xi}\boldsymbol{\nabla} f + \frac{\boldsymbol{F}}{\rho}\partial_{\boldsymbol{\xi}} f = \Omega^{\mathrm{C}}(f). \tag{2.34}$$

The right term is a collision operator $\Omega^{\mathrm{C}}(f)$. This collision operator prescribes how the populations relax towards the equilibrium population f^{eq}, also called the Maxwell-Boltzmann equilibrium function. The *collision operator moments* are fully conservative, namely

$$\text{mass conservation:} \quad \int \Omega^{\mathrm{C}}(f)\,\mathrm{d}^3\boldsymbol{\xi} = 0,$$

$$\text{momentum conservation:} \quad \int \boldsymbol{\xi}\,\Omega^{\mathrm{C}}(f)\,\mathrm{d}^3\boldsymbol{\xi} = 0,$$

$$\text{total energy conservation:} \quad \int |\boldsymbol{\xi}|^2\Omega^{\mathrm{C}}(f)\,\mathrm{d}^3\boldsymbol{\xi} = 0.$$

For an ideal monoatomic gas with perfectly colliding identical spherical particles, this probability function can be written as

$$f^{\mathrm{eq}} = \rho\left(\frac{1}{2\pi R_{\mathrm{g}} T}\right)^{\frac{3}{2}} exp\left(\frac{-|\boldsymbol{\xi}-\boldsymbol{u}|^2}{2R_{\mathrm{g}} T}\right). \tag{2.35}$$

R_g stands here for the universal gas constant. The equilibrium population can always be derived from the macroscopic gas density and mean velocity and the velocity of gas molecules by the given temperature T.

The Boltzmann equation has the following general *properties*:

- this is an equation for non-equilibrium processes,
- knowing the PDFs the macroscopic quantities like density and velocity can be derived,
- this equation is valid for all Knudsen numbers,
- for continuum regime macroscopic conservation equations can derived through the Chapman-Enskog expansion,

and *limitations*:

- influence of the intermolecular forces e.g. van der Waals or electorstatic is not considered,
- collision time is very short,
- only binary collisions are considered,
- only elastic hard spheres are considered as molecules.

The *Lattice Boltzmann Equation (LBE)* presupposes in a standard form a continuum Eulerian flow with $\mathrm{Kn} \ll 1$. LBE uses simplified collision operators, e.g. the *Bhatnagar-Gross-Krook (BGK)* collision operator (also used for the standard Boltzmann equation)

$$\Omega_j^{\mathrm{BGK}}(f_j) = \frac{1}{\tau}(f_j^{\mathrm{eq}} - f_j). \tag{2.36}$$

The relaxation time τ is the time between two molecule collisions, which can be regarded as the temporal analogue of the MFP. Macroscopically, the relaxation time determines the viscosity of the flow or diffusivity of a species. The LBE is valid for low Mach numbers where, by small Knudsen numbers, it reconstructs Navier-Stokes equations. LBE is applied to structured Cartesian lattices. LBE can be written as

$$f_j(\boldsymbol{x} + \boldsymbol{\xi}_i \triangle t, t + \triangle t) - f_j(\boldsymbol{x}, t) = \triangle t \left(\Omega_j^C + \left(1 - \frac{\triangle t}{2\tau}\right) \Omega_j^{\mathrm{S}} \right). \tag{2.37}$$

Here f_j is the PDF in a lattice direction and $\boldsymbol{\xi_j}$ is the normalized molecular velocity in the corresponding direction. The discrete equilibrium population approximates the Maxwell-Boltzmann equilibrium in the second order:

$$f_j^{\mathrm{eq}}(\boldsymbol{x},t) = w_j\rho\left(1+\frac{\xi_{j\alpha}u_\alpha}{c_s^2}+\frac{\left(\xi_{j\alpha}\xi_{j\beta}-c_s^2\delta_{\alpha\beta}\right)u_\alpha u_\beta}{2c_s^4}\right). \tag{2.38}$$

The w_j is the weighting coefficient of the Hermite quadrature, and $c_\mathrm{s}=\sqrt{RT}$ is the discrete normalized speed of sound, which comes from the ideal gas law.

These *equilibrium function moments* lead to the macroscopic quantities, namely NSE terms

$$M_0^{\mathrm{eq}} = \sum_j f_j^{\mathrm{eq}} = \rho\ (\text{density}),$$

$$M_{1\alpha}^{\mathrm{eq}} = \sum_j f_j^{\mathrm{eq}}\xi_{j\alpha} = \rho u_\alpha\ (\text{momentum}),$$

$$M_{2\alpha\beta}^{\mathrm{eq}} = \sum_j f_j^{\mathrm{eq}}\xi_{j\alpha}\xi_{j\beta} = \rho c_\mathrm{s}^2\delta_{\alpha\beta}+\rho u_\alpha u_\beta = p+\rho u_\alpha u_\beta\ (\text{pressure tensor}),$$

$$M_{3\alpha\beta\gamma}^{\mathrm{eq}} = \sum_j f_j^{\mathrm{eq}}\xi_{j\alpha}\xi_{j\beta}\xi_{j\gamma} = \rho c_\mathrm{s}^2\left(u_\alpha\delta_{\beta\gamma}+u_\beta\delta_{\alpha\gamma}+u_\gamma\delta_{\alpha\beta}\right).$$

2.2.2 LBM discretization for Eulerian flow PDEs

After presenting the basic definitions of LBM, equilibrium functions and source terms [77] for different equations are listed in Table 2.1 according to the increasing order of the functions.

Eq.	$f_j^{\mathrm{eq}}(\boldsymbol{x},t)$	$\Omega_j^{\mathrm{S}}(\boldsymbol{x},t)$
PE (2.12)	$w_j s$	$w_j Q_{s,\mathbf{PE}}$
ADE (2.11)	$w_j s\left(1+\frac{\xi_j\cdot\boldsymbol{u}_{\mathrm{ad}}}{c_\mathrm{s}^2}\right)$	$w_j Q_{s,\mathbf{ADE}}$
NSE (2.7, 2.8)	$w_j\rho\left(1+\frac{\xi_j\cdot\boldsymbol{u}}{c_\mathrm{s}^2}+\frac{(\xi_j\xi_j-\delta_{\alpha\beta}c_\mathrm{s}^2):\boldsymbol{uu}}{2c_\mathrm{s}^4}\right)$	$w_j\rho\left(\frac{\xi_j}{c_\mathrm{s}^2}+\frac{(\xi_j\xi_j-\delta_{\alpha\beta}c_\mathrm{s}^2)\cdot\boldsymbol{u}}{c_\mathrm{s}^4}\right)\cdot\frac{\boldsymbol{F}}{\rho}$

Table 2.1.: Used LBM equilibrium and source terms.

The w_j are the integration weighting Hermite coefficients (cf. Table 2.3).

In *PE* there is no time derivative of potential, which is why in the case of LBM discretization the apparent time derivative is eliminated by reaching the converged state.

The macrovariables are recovered through the moments of PDFs (Table 2.2).

Eq.	M_0	M_1
PE (2.12)	$s = \sum_j f_{j,\mathbf{PE}} + \frac{1}{2} Q_{s,\mathbf{PE}}$	$\boldsymbol{\nabla} s = -\frac{1}{\tau_s c_s^2 \triangle x} \sum_j \boldsymbol{\xi}_j f_{j,\mathbf{PE}}$
ADE (2.11)	$s = \sum_j f_{j,\mathbf{ADE}} + \frac{1}{2} Q_{s,\mathbf{ADE}}$	-
NSE (2.7, 2.8)	$\rho = \sum_j f_{j,\mathbf{NSE}}$	$\rho \boldsymbol{u} = \sum_j \boldsymbol{\xi}_j f_{j,\mathbf{NSE}} + \frac{1}{2} \boldsymbol{F}$

Table 2.2.: PDFs moments.

Shear stress terms are recovered through the second-order moment:

$$S_{\alpha\beta} = -\left(1 - \frac{\triangle t}{2\tau_{\mathbf{NSE}}}\right)\left[\sum_j \xi_{j,\alpha}\xi_{j,\beta} f^{\mathrm{neq}}_{j,\mathbf{NSE}} + \sum_j \xi_{j,\alpha}\xi_{j,\beta}\Omega^{\mathrm{S}}_j(\boldsymbol{F})\right]. \tag{2.39}$$

According to the Chapman-Enskog expansion [78] the relaxation time τ can be related to molecular viscosity or diffusivity:

$$\tau_{\mathrm{NSE}} = \frac{\nu}{c_s^2} + \frac{\triangle t}{2}, \tag{2.40}$$

$$\tau_{\mathrm{RADE}} = \frac{D_i(\boldsymbol{x}, t)}{c_s^2} + \frac{\triangle t}{2}. \tag{2.41}$$

The given here LBEs in terms of the current work are applied to following lattice types: 2D – $D2Q9$, 3D – $D3Q7$, $D3Q19$, $D3Q27$.

2.2.3 Boundary conditions in LBM

NSE boundary conditions

In LBM, boundary conditions are usually applied to the PDFs rather than to the macroscopic variables, which makes the entire procedure more complex.

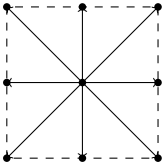

(a) $D2Q9$ lattice

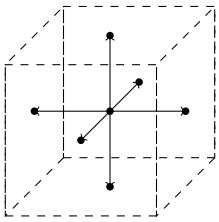

(b) $D3Q7$ lattice

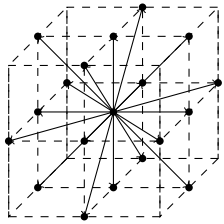

(c) $D3Q19$ lattice

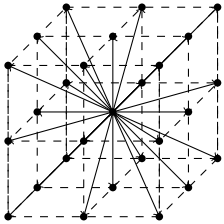

(d) $D3Q27$ lattice

Figure 2.3.: Comparison of lattice configurations with borders.

For *Dirichlet*-type boundary conditions from the LBM point of view, the *wet-node non-equilibrium approach* is used [79]. Thereby, populations at the boundary lattice points ($\boldsymbol{x}_\mathrm{p}$) are constructed from both equilibrium f_j^eq and non-equilibrium populations f_j^neq. If the velocity is fixed and the pressure is treated with the *Neumann* boundary condition, the following scheme is applied: in the equilibrium part, the velocity is prescribed from the macro-level and density ρ_rec is reconstructed from incoming populations. The non-equilibrium part is computed from stress tensor components received through finite differences in neighbor bulk cells $S_{\alpha\beta}^\mathrm{FD}$:

$$f_{j,\mathbf{NSE}}(\boldsymbol{x}_\mathrm{p}) = f_{j,\mathbf{NSE}}^\mathrm{eq}(\rho_\mathrm{rec}, u_n(\boldsymbol{x}_\mathrm{p})) + f_{j,\mathbf{NSE}}^\mathrm{neq}(S_{\alpha\beta}^\mathrm{FD}), \tag{2.42}$$

$$\rho_\mathrm{rec} = \frac{1}{1 - \boldsymbol{n}\cdot\boldsymbol{u}}\left(\sum_j^{\text{along boundary}} f_{j,\mathbf{NSE}} + 2\sum_j^{\text{towards boundary}} f_{j,\mathbf{NSE}}\right), \tag{2.43}$$

$$f_{j,\mathbf{NSE}}^\mathrm{neq}(S_{\alpha\beta}^\mathrm{FD}) = w_j \frac{(\xi_{j,\alpha}\xi_{j,\beta} - c_\mathrm{s}^2\delta_{\alpha\beta})}{2c_\mathrm{s}^4} S_{\alpha\beta}^\mathrm{FD}. \tag{2.44}$$

For a *fixed pressure* boundary combined with *zero-gradient velocity* boundary, a similar approach is used. Instead of a prescribed macroscopic velocity, a fixed

Directions j	Normalized lattice velocities ξ_j	Lattice weights w_j
	$D2Q9$	
0	$(0,0)$	$4/9$
$1,2,3,4$	$(\pm1,0),(0,\pm1)$	$1/9$
$5,6,7,8$	$(\pm1,\pm1)$	$1/36$
	$D3Q7$	
0	$(0,0,0)$	$1/4$
$1,2,\ldots,6$	$(\pm1,0,0),(0,\pm1,0),(0,0,\pm1)$	$1/8$
	$D3Q19$	
0	$(0,0,0)$	$1/3$
$1,2,\ldots,6$	$(\pm1,0,0),(0,\pm1,0),(0,0,\pm1)$	$1/18$
$7,8,\ldots,18$	$(\pm1,\pm1,0),(\pm1,0,\pm1),(0,\pm1,\pm1)$	$1/36$
	$D3Q27$	
0	$(0,0)$	$8/27$
$1,2,\ldots,6$	$(\pm1,0,0),(0,\pm1,0),(0,0,\pm1)$	$2/27$
$7,8,\ldots,18$	$(\pm1,\pm1,0),(\pm1,0,\pm1),(0,\pm1,\pm1)$	$1/54$
$19,20,\ldots,26$	$(\pm1,\pm1,\pm1)$	$1/216$

Table 2.3.: Lattice discretization parameters.

density ρ_{ref} of fluid is used. Velocities u_{rec} are reconstructed from incoming populations, and the non-equilibrium is also computed by finite differences:

$$f_{j,\mathbf{NSE}}(\boldsymbol{x}_{\text{p}}) = f^{\text{eq}}_{j,\mathbf{NSE}}(\rho_{\text{ref}}, u_{\text{rec}}) + f^{\text{neq}}_{j,\mathbf{NSE}}(S^{\text{FD}}_{\alpha\beta}), \tag{2.45}$$

$$u_{\text{rec}} = \frac{1}{\rho_{\text{ref}}}\left(\sum_{j}^{\text{along boundary}} \xi_j f_{j,\mathbf{NSE}} + 2 \sum_{j}^{\text{towards boundary}} \xi_j f_{j,\mathbf{NSE}}\right). \tag{2.46}$$

At the walls, *no-slip* boundary condition is often applied, which is realized through *bounce back* of incoming populations at the wall [80]:

$$f_{\bar{j}}(\boldsymbol{x}_p, t + \triangle t) = f_{j,\text{pre-stream}}(\boldsymbol{x}_p, t), \tag{2.47}$$

$$\xi_{\bar{j}} = -\xi_j. \tag{2.48}$$

2.2.3.1 ADE boundary conditions

At the mesoscopic level by ADE, the velocity is always known from the precomputed NSE. So, by the *Dirichlet* boundary condition, the transported scalar is fixed and is thus put in the PDFs with a moment-based approach [81]:

$$f_{i,\mathbf{ADE},\text{unknown}}(\boldsymbol{x}_\text{p}) = s(\boldsymbol{x}_\text{p}) - \sum_{j,\text{known}} f_{j,\mathbf{ADE}}. \tag{2.49}$$

Known populations are here those that come from neighboring bulk cells. The unknown is the population that comes from the wall. By the *Neumann* boundary condition, an average value of two neighboring cell populations in the current lattice direction is taken:

$$f_{j,\mathbf{ADE}}(\boldsymbol{x}_\text{p}) = \frac{1}{2}(f_{j,\mathbf{ADE}}(\boldsymbol{x} - \boldsymbol{\xi}_j \cdot \boldsymbol{n}) + f_{j,\mathbf{ADE}}(\boldsymbol{x} - 2\boldsymbol{\xi}_j \cdot \boldsymbol{n})). \tag{2.50}$$

More information on methods for boundary conditions in LBM is provided in [75] and references therein.

2.2.4 LBM discretization for multiphase Eulerian models

The multiphase *Mixture model* with a single NSE considers the mixture density, which is always a combination of the concentrations of the mixture components. This spatially and temporally changing density can be considered as compressible and cannot be solved with standard LBM. Shu *et al.* simplified the momentum conservation equation of the mixture model by dividing the whole equation by the mixture density, taking it off from all the gradients [52]. The mixture density is still preserved in the pressure term, which is corrected by solving the PE with FVM. This approach is applicable for cases with a mixture density that does not vary strongly.

In terms of LBM, the *Darcy–Brinkmann* approach was realized by Spaid *et al.* [55]. There, the LBM velocity in the equilibrium PDF is modified by a factor that includes the permeability of the medium. Simonis *et al.* expanded this approach and proved that it reconstructs the Darcy–Brinkmann term [56]. With LBM, *model of Nithiarasu et al.* [69] was discretized by Guo *et al.* and Wang *et al.* [57, 58].

The most complex task from the LBM perspective is to reconstruct the *complete VANSE* for the multiphase *Euler-Euler approach* due to the effective density $\phi^{\flat}\rho$, which is variable in space and time in many cases. Zhang *et al.*, Höcker *et al.*, and the author of the current work, as shown later, tried to use the effective density directly in the equilibrium PDF together with the correction forces for the pressure term [59, 60, 62]. Unfortunately, these approaches show stability problems when applied to realistic situations with sharp volume fraction gradients. Adjustment of the developed approach to handle these gradients is not performed in the scope of the current thesis.

Blais *et al.* and Fu *et al.* suggested other ansatzes to avoid these stability issues by using the volume fraction only in the zeroth population, which is not streamed to the neighbor cells [61, 63]. Blais *et al.* proposed using the effective density only in the zeroth population and the corresponding correction forces to reconstruct the right stress tensor and pressure term. Unfortunately, this approach is stable only at liquid volume fractions above 45%. The behavior of this method was not investigated for discontinuous volume fraction transitions. Recently, Fu *et al.* used LBM with externally calculated pressure. There is also a correction term computed using FDM in space and time. This approach was tested with temporally and spatially changing continuous volume fraction values. Realistic application simulations have not been conducted using this approach.

2.2.4.1 Overview of existing VANSE-LBM

In the current Section, VANSE-LBM discretization approaches are presented. All of them target the Equations 2.26 and 2.27.

Zhang *et al.* [59]
The first attempt to reconstruct full VANSE with LBM and investigate it with the Chapman-Enskog expansion was made by [59]. They proposed a scaled equilibrium distribution function

$$f_j^{\mathrm{eq}} = w_j\,\rho\phi^{\flat}\left(1 + \frac{\xi_{j\alpha}u_\alpha}{c_s^2} + \frac{\left(\xi_{j\alpha}\xi_{j\beta} - c_s^2\delta_{\alpha\beta}\right)u_\alpha u_\beta}{2c_s^4}\right). \tag{2.51}$$

This function leads to the correct VANSE, excluding the pressure term, which must be adjusted with an appropriate force

$$F^{\mathrm{P}} = p\nabla\phi^{\flat}. \tag{2.52}$$

This scheme was tested only on one case with a constant porosity of 0.1, which does not give a full impression of the scheme's behavior in realistic situations with changing values of ϕ^{b} in space and time.

Bukreev *et al.* [62]
[62] applied the previous scheme (equations 2.51, 2.52) to temporally and spatially changing porosity values in analytical examples constructed with manufactured solutions and identified unstable behavior of the [59] approach. The reason for that was streaming of local porosity values to the neighbor cells during the streaming step. [62] proposed a new pressure correction term which considers this streaming effect

$$F^{\mathrm{P}} = p\boldsymbol{\nabla}\phi^{\mathrm{b}} = \rho c_{\mathrm{s}}^2 \boldsymbol{\nabla}\phi^{\mathrm{b}} = \frac{\sum_i f_i}{\sum_j \varpi_j \phi(\triangle x + \boldsymbol{c}_j \triangle t)} c_{\mathrm{s}}^2 \boldsymbol{\nabla}\phi^{\mathrm{b}}. \tag{2.53}$$

Here, the coefficients ϖ_j are slightly different from the weights w_j and also depend on the chosen lattice type. Convergence tests on examples with values of ϕ^{b} changing in space and time showed an order of 2 in two-dimensional and three-dimensional cases. In this work, the impact of the discontinuous behavior of ϕ^{b} was not investigated. Later studies have shown unstable simulation behavior in realistic applications with sharp volume fraction gradients, which is why this scheme is not applied in the macroscopic adsorption simulation in this thesis. In future works, this scheme needs an appropriate stabilization approach.

Derivation of this approach is given in the Appendix A.1.

Höcker *et al.* [60]
In this work, the authors suggest using the equilibrium scheme of [59] with other correction terms. They propose using an extended LB equation, namely

$$\begin{aligned} f_j\left(\boldsymbol{x} + \boldsymbol{\xi}_j \triangle t,\, t + \triangle t\right) = f_j\left(\boldsymbol{x},\, t\right) - \frac{f_j\left(\boldsymbol{x},\, t\right) - f_i^{\mathrm{eq}}\left(\boldsymbol{x},\, t\right)}{\tau} \\ + w_j \sum_j f_j((\boldsymbol{x}, t)) \frac{\phi^{\mathrm{b}}(\boldsymbol{x} + \boldsymbol{\xi}_j \triangle t, t + \triangle t) - \phi^{\mathrm{b}}(\boldsymbol{x}, t)}{\phi^{\mathrm{b}}(\boldsymbol{x}, t)}. \end{aligned} \tag{2.54}$$

This equation can also be rewritten as

$$\begin{aligned} f_j\left(\boldsymbol{x} + \boldsymbol{\xi}_j \triangle t,\, t + \triangle t\right) = f_j\left(\boldsymbol{x},\, t\right) + f_i^{\mathrm{eq}}\left(\boldsymbol{x},\, t\right) + \left(1 - \frac{1}{\tau}\right) f_j^{\mathrm{neq}}\left(\boldsymbol{x},\, t\right) \\ + w_j \rho(\phi^{\mathrm{b}}(\boldsymbol{x} + \boldsymbol{\xi}_j \triangle t, t + \triangle t) - \phi^{\mathrm{b}}(\boldsymbol{x}, t)). \end{aligned} \tag{2.55}$$

This LBM for flow in porous media was tested on examples with analytical solutions as well. It has shown second order of convergency in the case with spatially variable volume fraction. By the temporally changing porosity the scheme behaved divergently, which was mentioned by the authors as a systematic error. In comparison to earlier other publications, [60] presented an Euler-Euler scheme using the developed approach for the Rayleigh-Taylor instability, which will be summarized in the next chapter.

Blais *et al.* [61]
In this work, the authors investigated the scheme of [59] in different cases and observed unstable behavior. That is why they constructed new LB equilibrium functions for the discretization of VANSE on a D2Q9 lattice using the method of moments and performed a Chapman-Enskog analysis of the resulting distributions.

$$f_0^{\mathrm{eq}} = w_0\left(\frac{9\rho\phi^{\mathrm{b}} - 5\rho + 5\rho_\infty}{4} - \rho\phi^{\mathrm{b}}\left(\frac{\boldsymbol{u}\cdot\boldsymbol{u}}{2c_{\mathrm{s}}^2}\right)\right), \tag{2.56}$$

$$f_j^{\mathrm{eq}} = w_j\left(\rho - \rho_\infty + \rho\phi^{\mathrm{b}}\left(\frac{\boldsymbol{u}\cdot\boldsymbol{\xi}_j}{c_{\mathrm{s}}^2} + \frac{(\boldsymbol{u}\cdot\boldsymbol{\xi}_j)^2 - c_{\mathrm{s}}^2 u^2}{2c_{\mathrm{s}}^4}\right)\right). \tag{2.57}$$

This scheme has an advantage in not streaming the effective density $\rho\phi^{\mathrm{b}}$ to neighbor cells, because it is stored in the zeroth equilibrium distribution which is excluded from the streaming step. Unfortunately, the provided scheme requires a case-specific parameter ρ_∞, so that the first term in Eq. 2.56 remains always positive. The second complication is the need for additional correction terms for the stress tensor and the pressure term

$$F^{\mathrm{P}} = (1-\phi^{\mathrm{b}})\boldsymbol{\nabla}(\rho c_{\mathrm{s}}^2). \tag{2.58}$$

The correction term for the stress tensor arises from the Chapman-Enskog expansion as

$$\begin{aligned}\partial_\beta\Theta_{\alpha\beta} = \partial_\beta\Big(&\nu u_\alpha(\partial_\beta(\rho\phi^{\mathrm{b}}) - \partial_\beta\rho) + \nu u_\beta(\partial_\alpha(\rho\phi^{\mathrm{b}}) - \partial_\alpha\rho)\\ &+ \nu\partial_\gamma(\rho\phi^{\mathrm{b}}u_\gamma)\delta_{\alpha\beta} - \frac{\nu}{\phi^{\mathrm{b}}}(\partial_\gamma(\rho\phi^{\mathrm{b}}u_\gamma) + \rho\partial_t\phi^{\mathrm{b}})\\ &+ \frac{2}{3}\nu\rho\phi^{\mathrm{b}}\partial_\gamma u_\gamma\delta_{\alpha\beta}\Big).\end{aligned} \tag{2.59}$$

The derivatives in this term are computed with finite differences.

Convergency tests of the presented approach showed stable behavior with second order convergency by liquid volume fractions greater than 0.45. By lower values of ϕ^{b} the authors suggest to rescale volume fractions in the whole domain. The performed test cases are all with continuous function of ϕ^{b}. The behavior of the proposed method by discontinuous development of the volume fraction was not investigated.

Fu *et al.* [63]
As already shown in the previous Section, the existing approaches lead to instabilities by application to discontinuous volume fraction distributions. The reason for this is the "compressible" effective density $\rho_{eff} = \phi^{\mathrm{b}}\rho$, which cannot be handled by standard LBM. Direct pressure–density coupling of the method leads to spurious velocities in the regions with high porosity differences between neighbor cells. To avoid that fact, [63] constructed new modified LB equations with appropriate new equilibrium PDFs where the pressure is considered already inside of the PDFs. This new approach is called pressure-based LBM and can be summarized as follows:

$$f_j\left(\boldsymbol{x} + \boldsymbol{\xi}_j \triangle t,\, t + \triangle t\right) = f_j\left(\boldsymbol{x},\, t\right) - \frac{f_j\left(\boldsymbol{x},\, t\right) - g_i^{\mathrm{eq}}\left(\boldsymbol{x},\, t\right)}{\tau} \tag{2.60}$$

$$+\triangle t\Big(G_j\left(\boldsymbol{x},\, t\right) + \frac{G_j\left(\boldsymbol{x} + \boldsymbol{\xi}_j \triangle t,\, t\right) - G_j\left(\boldsymbol{x}, t - \triangle t\right)}{2}\Big). \tag{2.61}$$

The corresponding equilibrium functions are:

$$g_0^{\mathrm{eq}} = \frac{p}{c_{\mathrm{s}}^2}(w_0 - 1) - w_j\rho\phi^{\mathrm{b}}\Big(\frac{\boldsymbol{u}\cdot\boldsymbol{u}}{2c_{\mathrm{s}}^2}\Big), \tag{2.62}$$

$$f_j^{\mathrm{eq}} = \frac{p}{c_{\mathrm{s}}^2}w_j + w_j\rho\phi^{\mathrm{b}}\Big(\frac{\boldsymbol{u}\cdot\boldsymbol{\xi}_j}{c_{\mathrm{s}}^2} + \frac{\left(\boldsymbol{u}\cdot\boldsymbol{\xi}_j\right)^2 - c_{\mathrm{s}}^2u^2}{2c_{\mathrm{s}}^4}\Big). \tag{2.63}$$

The correction term G_j that is necessary for the correct reconstruction of VANSE is written as:

$$G_j = w_j\Big(-\partial_t(\phi^{\mathrm{b}}\rho) + \frac{\boldsymbol{\xi}_j\left(\boldsymbol{F} + (1-\phi^{\mathrm{b}})\boldsymbol{\nabla}p\right)}{c_{\mathrm{s}}^2} + \frac{\left(\boldsymbol{\xi}_j\boldsymbol{\xi}_j - c_{\mathrm{s}}^2\boldsymbol{I}\right) : (A\boldsymbol{I} + \boldsymbol{M})}{2c_{\mathrm{s}}^4}\Big), \tag{2.64}$$

$$A = -\frac{2}{3}c_{\mathrm{s}}^2\Big(\partial_t(\phi^{\mathrm{b}}\rho) + \boldsymbol{u}\cdot\boldsymbol{\nabla}(\phi^{\mathrm{b}}\rho)\Big), \tag{2.65}$$

$$\boldsymbol{M} = c_{\mathrm{s}}^2\left(\boldsymbol{u}\boldsymbol{\nabla}(\phi^{\mathrm{b}}\rho) + \boldsymbol{\nabla}(\phi^{\mathrm{b}}\rho)\boldsymbol{u}\right). \tag{2.66}$$

The derivatives in this term are computed using FDM. The goal macro-moments are defined also differently compared to standard LBM:

$$\rho = const, \tag{2.67}$$

$$\boldsymbol{u} = \frac{1}{\phi^{\mathfrak{b}}\rho}\sum_{j}\boldsymbol{\xi}_j f_j, \tag{2.68}$$

$$p = \frac{c_{\mathrm{s}}^2}{1-w_0}\left(-w_0\rho\phi^{\mathfrak{b}}\left(\frac{\boldsymbol{u}\cdot\boldsymbol{u}}{2c_{\mathrm{s}}^2}\right) + \sum_{j\neq 0} f_j + \tau\triangle t G_0\right). \tag{2.69}$$

2.3 Methodology for validation of simulation models

In the current work, different novel simulation models and discretization approaches are presented. They are validated on reference data, which can be solutions of analytically solvable problems, established numerical benchmarks (e.g. results of DNS) or experimental measurements. In the simulations shown further in this work, the results are compared with these reference data optically (comparison of laser induced fluorescence pictures with the visualized simulation results) and quantitatively (comparison of *absolute and relative error norms*). These norms can be summarized to a convergence study by plotting the norms of simulations by distinct spatial resolutions. The errors correspond to L^1-, L^2- and L^∞-*absolute norms* over nodal values of a chosen variable deviations between the simulated and the prescribed data [82], i.e.

$$L^1_{\mathrm{abs}}\left(s^{\mathfrak{b}}\right) = \frac{1}{N_{\mathrm{node}}}\sum_{c=1}^{N_{\mathrm{node}}}\left|s_c^{\mathfrak{b}} - s_c^{\mathfrak{b},\star}\right|, \tag{2.70}$$

$$L^2_{\mathrm{abs}}\left(s^{\mathfrak{b}}\right) = \sqrt{\frac{1}{N_{\mathrm{node}}}\sum_{c=1}^{N_{\mathrm{node}}}\left|s_c^{\mathfrak{b}} - s_c^{\mathfrak{b},\star}\right|^2}, \tag{2.71}$$

$$L^\infty_{\mathrm{abs}}\left(s^{\mathfrak{b}}\right) = \max_{c=1,..,N_{\mathrm{node}}}\left|s_c^{\mathfrak{b}} - s_c^{\mathfrak{b},\star}\right|, \tag{2.72}$$

respectively, where $s^{\mathfrak{b},\star}$ denotes the corresponding reference value.

A better way to analyze the numerical deviations is to compute *relative norms*:

$$L^1_{\mathrm{rel}}\left(s^\flat\right) = \frac{\sum_{c=1}^{N_{\mathrm{node}}} \left|s_c^{\flat,\star} - s_c^\flat\right|}{\sum_{c=1}^{N_{\mathrm{node}}} \left|s_c^{\flat,\star}\right|}, \tag{2.73}$$

$$L^2_{\mathrm{rel}}\left(s^\flat\right) = \sqrt{\frac{\sum_{c=1}^{N_{\mathrm{node}}} \left|s_c^{\flat,\star} - s_c^\flat\right|^2}{\sum_{c=1}^{N_{\mathrm{node}}} \left|s_c^{\flat,\star}\right|^2}}, \tag{2.74}$$

$$L^\infty_{\mathrm{rel}}\left(s^\flat\right) = \frac{\max\limits_{c=1,..,N_{\mathrm{node}}} \left|s_c^{\flat,\star} - s_c^\flat\right|}{\max\limits_{c=1,..,N_{\mathrm{node}}} \left|s_c^{\flat,\star}\right|}. \tag{2.75}$$

Regarding the behavior of the error norms by refinement of spatial and temporal resolutions (*diffusive* or *acoustic scaling*), the *experimental order of convergence (EOC)* can be established [8]. This is a derivative of the logarithm of the error norms with respect to the logarithm of the cell size or resolution, and it says *how fast the simulation results approach the reference solution.*

After explaining the main definitions and model equations used further in this thesis, the macroscopic multiphase multicomponent Euler-Euler simulation model for a full-size reactor will be presented.

3 Modeling and simulation at the macro-level

This Section is based on a published article:
***Bukreev, F.**, Raichle, F., Nirschl, H., Krause, M. J. (2023). Simulation of adsorption processes on moving particles based on an Euler-Euler description using a lattice Boltzmann discretization. Chemical Engineering Science, 270, 118485. DOI:10.1016/j.ces.2023.118485*

A description of the applications used here is provided in Section A.2.1.1.

This Chapter aims to find an answer to the first question (Q1) defined in Section 1.2. Thereby, an Euler-Euler description of moving particles is combined with more detailed adsorption kinetics at unresolved subgrid microparticles. These equations are solved using the LBM with each component of the model represented by its own lattice. The fluid lattice is one-way coupled with all the other lattices, which themselves are coupled between each other according to the adsorption model, which is used to describe crystallization in the pores of microparticles including distinct diffusion levels. To the author's knowledge, this is the first use of a spatially variable particle concentration describing moving particles according to the Eulerian multicomponent approach as the basis for adsorption dynamics. It is also the first implementation of multiple mass transfer mechanisms for the LDF, evidenced by investigating the convergence behavior of the model using LBM discretization. The simulation model is implemented and tested in the *OpenLB* open-source software library [9].

The first part of this Chapter will introduce the underlying concepts and equations for describing adsorption and fluid dynamics. The chosen adsorption model is explained as well. The second part shows applications and validations of the model in a series of simulations ranging from a simple batch reactor to

the complex flow field in a static mixer. Finally, distinct parameters used in the simulation model are discussed from the optimization point of view. In this Chapter, the steps **S1.1–S1.3** are performed on a macroscopic application.

3.1 Multiphase multicomponent NSE-ADE model

Before starting the composition of a simulation model for a full-size adsorption reactor, several assumptions should be stated for the current application case:

- microparticles do not influence the carrier fluid flow,
- total solid volume of microparticles in each cell is much smaller then the fluid volume,
- all particles have the same size and density,
- concentration of solved phosphate do not influence density of the carrier fluid.

Based on them, the NSE-ADE model with one-way coupling (see Section 2.1.5) is built to represent the adsorption reactor in its full size.

3.1.1 Fluid dynamics modeling

The goal of this work is the coupling of fluid dynamics and adsorption dynamics. All components in the system are described by an Eulerian approach.

Carrier fluid

The incompressible NSE describe the carrier fluid dynamics (Eq. 2.9, 2.10).

Solute

The dissolved adsorbate is described by its own species mass balance [83, 84] in the RADE (Equation 2.11) with $s = C$ as the concentration and $q_\mathrm{s} = \dot{m}_\mathrm{ads}$ as a source term. The source term results from the change dC/dt in a volume element. However, in this thesis, the factor in (3.3) that includes the bed porosity is not considered.

Particles

The moving adsorbent particles are described also by the ADE (Equation 2.11), meaning they are not resolved individually but represented by a particle concentration $s = C_\mathrm{p}(\boldsymbol{x})$, which is used as a measure of the mass of particles per volume of flow, as opposed to ρ_p, which is the material density of the particles. Their motion is coupled to that of the fluid through the fluid velocity $\boldsymbol{u}_\mathrm{f}$ which is calculated using the NSE and updated with particle forces as in [64].

Particle loading

In addition to the particle density, the particle loading $C_{\bar{q}}$ is also tracked. Because the particle loading is treated as a transportable quantity with varying particle density, treating it as a concentration is more useful. $C_{\bar{q}} = C_\mathrm{p}\bar{q}$ is used with constant C_p taken from the previous equation in a further ADE, where $s = C_{\bar{q}}$ and a source term $q_\mathrm{s} = C_\mathrm{p}\dot{m}_\mathrm{ads}$ represent the change in loading from adsorption. $\dot{m}_\mathrm{ads}$ is the same as the source term in the solute transport equation.

The inclusion of diffusion for the particles makes the model a dispersive one. The coefficient D in the particle loading ADE can include contributions from different mechanisms, such as diffusion, mixing, etc. This makes it possible to be solved using LBM. Depending on the particle size, it may be more desirable to have no diffusion at all. This can only be approximated by a very small diffusion coefficient D.

3.1.2 Adsorption modeling

The adsorption model is based on the assumptions that mass transfer is the rate determining step and that the surface interaction can be disregarded [85]. There are several mass transfer mechanisms that can come into play, namely film diffusion, surface diffusion, and pore diffusion.

Because adsorption is primarily a surface phenomenon, its accurate description in an Euler-Euler model presents some challenges. It is impossible, for example, to maintain a detailed representation of the concentration gradients inside every single particle. To work around this issue, Glueckauf and Coates [86] proposed a linearized approach, called *LDF*, which is now widely used in adsorption modeling, especially in the description of fixed bed reactors [87, 88].

It postulates an area inside the particle with a linear concentration gradient similar to film diffusion and a core with a spatially constant concentration $\bar{q}(t)$. The model was also derived by Liaw *et al.* [89], who found that overall this is equivalent to a parabolic concentration profile in the particle. While the model was originally developed to simplify the surface diffusion model, it can be extended to include several transfer mechanisms, namely *film, surface and pore diffusion*. This separation will allow us to model different concentration gradients inside of the particle. It is assumed that all modeled particles are identical, have the same structure, and a homogeneous adsorption takes place in the dispersed phase.

The internal mass transport is modeled as

$$\frac{d\bar{q}}{dt} = k_{\mathrm{s}}^{*}\,(q_{\mathrm{s}} - \bar{q})\ , \tag{3.1}$$

with

$$k_{\mathrm{s}}^{*} = k_{\mathrm{s}}\frac{A_{\mathrm{s}}}{V_{\mathrm{A}}} = \frac{15 D_{\mathrm{s}}}{r_{\mathrm{p}}^{2}} \tag{3.2}$$

where q_{s} is the surface equilibrium loading, k_{s} and D_{s} the mass transfer and surface diffusion coefficient, A_{s} the particle surface area, r_{p} particle radius and V_{A} the adsorbent volume. The relation (3.2) for k_{s} was introduced by [86] for spherical particles.

Together with the mass balance for a particle as in (3.7), the change in concentration can be calculated with

$$-\frac{dC}{dt} = k_{\mathrm{s}}^{*}\frac{\rho_{\mathrm{p}}(1-\phi_{\mathrm{B}})}{\phi_{\mathrm{B}}}\,(q_{\mathrm{s}} - \bar{q})\,, \tag{3.3}$$

where the factor $\frac{\rho_{\mathrm{p}}(1-\varepsilon_{\mathrm{B}})}{\phi_{\mathrm{B}}} = \frac{m_{\mathrm{A}}}{V_{\mathrm{L}}}$ converts the adsorbate loading, which is defined per mass of adsorbent m_{A}, to concentration, which is defined per volume of liquid V_{L}. The particle's volume is included using the bed porosity ϕ_{B}. The particle density is denoted by ρ_{p}.

If the film diffusion is not incorporated into the model, the surface loading is simply the equilibrium loading corresponding to the bulk concentration:

$$q_{\mathrm{s}} = f(C). \tag{3.4}$$

It has been shown that this model can achieve impressive accuracy while reducing the computational effort [90, 91], which makes it especially useful for numerical simulations.

The model can be extended to include film diffusion on the outside of the particle as well. It acts as a boundary condition which is solved to get the surface concentration C_{s}. With the condition that the internal mass transfer equals the one through the film diffusion as a basis, it is

$$\rho_{\mathrm{p}} k_{\mathrm{s}}(q_{\mathrm{s}} - \bar{q}) = k_{\mathrm{f}}(C - C_{\mathrm{s}}), \tag{3.5}$$

where the surface loading q_{s} is a function of C_{s} via the equilibrium and the k_{s} and k_{f} are the surface and film mass transfer coefficients correspondingly. Once the new surface concentration has been found, the corresponding surface loading can be calculated and used as before in (3.1).

The LDF model can also be applied to pore diffusion with some simplifications. As shown by [92, 93], an effective mass transfer coefficient can be formulated to include the pore diffusion coefficient:

$$k_{\mathrm{s,eff}}^{*} = \frac{15 D_{\mathrm{s}}}{r_{\mathrm{p}}^{2}} + \frac{15 D_{\mathrm{p}}}{r_{\mathrm{p}}^{2}}\frac{C_0}{\rho_{\mathrm{p}}\, q_{0,\mathrm{eq}}}. \tag{3.6}$$

Here C_0 denotes the inlet solute concentration and $q_{0,\mathrm{eq}}$ the corresponding equilibrium loading. D_{p} is the pore diffusion coefficient. This new coefficient

can be substituted in (3.1) and (3.3) in cases where pore and surface diffusion both contribute significantly.

The summarized equation system according to the *LDF model for a batch reactor* consists of:

$$m_{\mathrm{A}} \frac{d\bar{q}}{dt} = -V_{\mathrm{L}} \frac{dC}{dt}, \tag{3.7}$$

$$\frac{d\bar{q}}{dt} = k_{\mathrm{s}}^{*} \left(q_{\mathrm{s}} - \bar{q}\right), \tag{3.8}$$

$$-\frac{dc}{dt} = k_{\mathrm{s}}^{*} \frac{(1-\varepsilon_{\mathrm{B}})}{\varepsilon_{\mathrm{B}}} \rho_{\mathrm{p}} \left(q_{\mathrm{s}} - \bar{q}\right), \tag{3.9}$$

$$\rho_{\mathrm{p}} k_{\mathrm{s}} (q_{\mathrm{s}} - \bar{q}) = k_{\mathrm{f}} (C - C_{\mathrm{s}}), \tag{3.10}$$

$$q_{\mathrm{s}} = f(C_{\mathrm{s}}), \tag{3.11}$$

$$\bar{q}(t=0) = 0, \quad C(t=0) = C_0. \tag{3.12}$$

Note that equation (3.10) only applies when film diffusion is included.

3.2 Discretization

The equations listed above are discretized using *LBM* with *BGK* collision operator on the *D*3*Q*19 lattice for NSE and *D*3*Q*7 lattice for ADEs (cf. Table 2.1, 2.2 and Figures 2.3c, 2.3b).

Coupling approach

Altogether the model requires four lattices which represent the different quantities that are being transported. These are: fluid density, solute concentration, particle density, and particle loading. The coupling scheme can be seen in Figure 3.1. The hexagons stand for the four lattices and the rounded rectangles for the equations or quantities that are being calculated by the model.

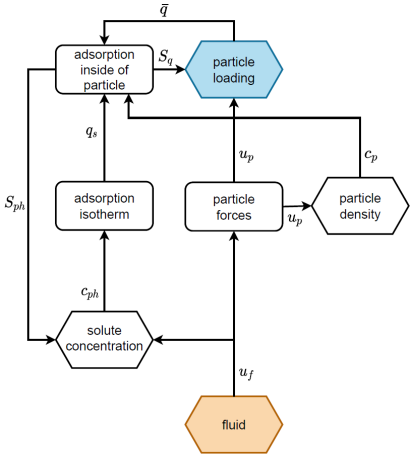

Figure 3.1.: Adsorption coupling scheme. Hexagons - lattices. Rectangles - postprocessors: particle forces convert carrier velocity to particle velocity, adsorption isotherm and adsorption inside of particle compute mass transport of the solute to particles (equations 3.7 - 3.12).

3.3 Numerical tests

The LDF model that was introduced in the previous sections is now used in several simulations to validate its accuracy and demonstrate its practical application.

In the cases discussed in this Chapter, the coupling between two types of lattices complicates the choice of parameters. Using the Schmidt number with the definitions of the viscosity and diffusivity in LBM the following expression is derived

$$\mathrm{Sc} = \frac{\nu}{D} = \frac{\Delta t_{\mathrm{ADE}}}{\Delta t_{\mathrm{NSE}}} \frac{(\tau_{\mathrm{NSE}} - 0.5)}{(\tau_{\mathrm{ADE}} - 0.5)} \,. \tag{3.13}$$

Assuming the same Δt for both lattices, this gives us the matching relaxation times for the ADE and the NSE lattices

$$\tau_{\mathrm{NSE}} = (\tau_{\mathrm{ADE}} - 0.5)\mathrm{Sc} + 0.5 \,. \tag{3.14}$$

With the values of Sc commonly being up to around 1000, this makes the relation very sensitive to the value of τ_{ADE}, and values very close to the minimum of 0.5 are often required.

3.3.1 Batch reactor

First, the adsorption model can easily be applied to a batch reactor, where using dimensionless quantities, an analytical solution for linear isotherms exists [92]. Following the linear driving force model, the dimensionless concentration $X = C/C_0$ evolves over time as

$$X(T) = \frac{1}{D_\mathrm{b} + 1} + \frac{D_\mathrm{b}}{D_\mathrm{b} + 1} \exp\left(-(D_\mathrm{b} + 1)T\right). \tag{3.15}$$

It uses a dimensionless time T with

$$T = k_\mathrm{s}^* \, t\,, \tag{3.16}$$

and a dispersion factor with

$$D_\mathrm{b} = \frac{m_\mathrm{A} \, q_{0,\mathrm{eq}}}{V_\mathrm{L} \, C_0}\,. \tag{3.17}$$

The model can also be made to include film diffusion. There is an analytical solution for pure film diffusion as well, it is structurally the same as eq. (3.15) but with a differently defined dimensionless time T. In the case of film diffusion

$$T = \frac{k_\mathrm{f}^*}{D_\mathrm{b}} t, \tag{3.18}$$

where, in the style of the surface diffusion coefficient, $k_\mathrm{f}^* = \frac{3k_\mathrm{f}}{r_\mathrm{p}}$. As previously stated, the new boundary condition for the surface concentration has to be solved numerically.

The batch reactor is realized as a cube $0.1 \times 0.1 \times 0.1$ m with periodic boundaries on all sides. The velocity for all components is zero, and perfect mixing or spatially uniform conditions are assumed. This results in a system that simply solves the differential equations for adsorption, without any fluid or particle interactions. First results are taken by the cell size of 2.4 mm and a relaxation time of 0.695. The process parameters and material properties that were used in the simulations are listed in the Table 3.1

Parameter		Value	Unit
Isotherm parameter	K	45	$\mathrm{L\,g^{-1}}$
Inlet concentration	C_0	1	$\mathrm{mg\,L^{-1}}$
Adsorbent concentration	C_p	0.94	$\mathrm{kg\,m^{-3}}$
Adsorbent density	ρ_p	1000	$\mathrm{kg\,m^{-3}}$
Side length	L	0.1	m
Particle radius	r_p	$1{,}5 \cdot 10^{-4}$	m
Surface diffusion coefficient	D_s	$5 \cdot 10^{-11}$	$\mathrm{m^2\,s^{-1}}$
Film diffusion coefficient	D_f	$7 \cdot 10^{-11}$	$\mathrm{m^2\,s^{-1}}$

Table 3.1.: Process parameters for batch reactor.

Results

The evolution of the concentration in the reactor C over time can be seen in Figure 3.2a. The concentration is homogeneous in the entire reactor because an only time-dependent equation is solved. The top x-axis shows the dimensionless time T, the bottom axis the time t in seconds. When using the dimensionless T, the shape of the curve only depends on the value of D_b which, for a linear isotherm, is a function of the slope of the isotherm K and the concentration of the adsorbent C_p alone. Specific kinetics are then introduced through the conversion to time t.

A good agreement with the analytical solution of the linear driving force model in eq. (3.15) as shown by Worch [92] is achieved. This demonstrates the correct implementation of the model and later the convergence of the discretized equations towards the model equation. On the topic of the accuracy of the model itself and the validity of the model in the first place, the reader may refer to existing literature [88, 90, 94].

Figure 3.2a also shows the amount of adsorbate taken up by the adsorbent. In the case of a batch reactor, this loading curve is a mirror of the concentration. The result of the simulation is the loading concentration C_q which can be transformed to the loading by dividing through the particle concentration C_p. The equilibrium loading q_eq is the amount of solute adsorbed in the state of equilibrium. For the system depicted above with a linear isotherm, C_eq was determined through the simulation to be $0.0231\ \mathrm{mg\,L^{-1}}$ which corresponds to an equilibrium loading of $1.0393\ \mathrm{mg\,g^{-1}}$.

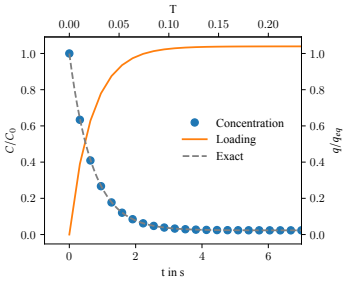

(a) Surface diffusion and linear isotherm.

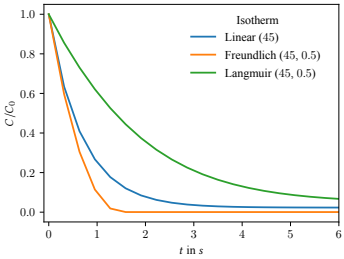

(b) The isotherm parameters are given in parentheses with the first one being the factor with the same unit as the loading (q_m and K).

Figure 3.2.: Concentration over time in batch reactor.

Experiments with different isotherms are shown in Figure 3.2b. With the kinetic (diffusion) parameters being the same, the influence of the equilibrium on the rate of the reaction is clearly visible. The same magnitude for the parameters was used (the units are different) and so the shape of the isotherms themselves and the equilibrium loading vary to a similar degree as the curves shown. Although the equilibrium concentration has not quite been reached yet after 6 seconds, it is higher for the Langmuir isotherm depicted in Figure 3.2b.

The LDF model was developed for surface diffusion, but film diffusion can be added as a boundary condition for the concentration. In order to test film diffusion on its own, a very small Biot number (Bi) can be used to eliminate the influence of surface diffusion. The results of pure film diffusion with Bi of order $1 \cdot 10^{-10}$ are shown in Figure 3.3 together with the previous result as a comparison. A good agreement with the analytical solution can be observed here as well, meaning that the addition of film diffusion was successful. The two mechanisms can, of course, be easily used in conjunction, just by setting their respective mass transfer coefficients to appropriate values.

Convergence

Because an analytical solution is known, the error of the simulation can be perfectly assessed. The $L^2(\frac{C}{C_0})$ error norm (Eq. 2.71) of the simulation relating to the analytical solution of (3.15) is shown in Figure 3.4a. If *diffusive scaling*

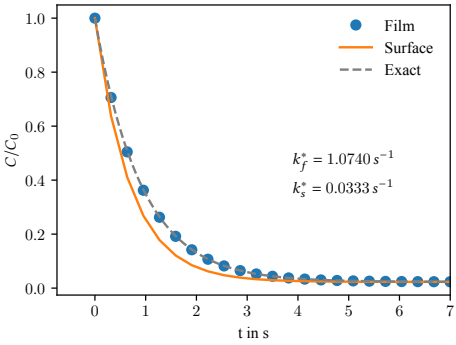

Figure 3.3.: Concentration in batch reactor with film diffusion and linear isotherm.

is used, which is the standard approach for LBM [8], an *EOC of 2* in L^2 is achieved. The relaxation time τ_{ADE} is 0,6.

In this case, the solution only depends on the time, and because the concentration is homogeneous at all times, diffusion does not play a role. So, additionally, the *error* is plotted *over the time step per spatial resolution* in Figure 3.4b. Now, a *convergence order of 1 for the time step* number is gained.

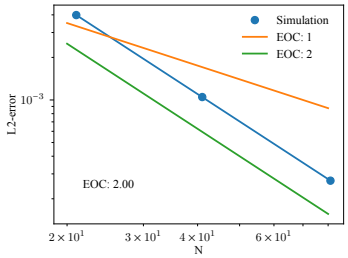

(a) Diffusive scaling with the cell number N in the cube side length on the abscissa.

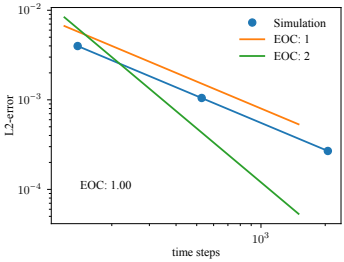

(b) Acoustic scaling with the number of time steps on the abscissa.

Figure 3.4.: L2-error for batch reactor. The simulation results for different resolutions are marked with blue dots.

Simulations with a prescribed source term as a function of time and an analytical solution, as it was used by Seta [95] were conducted and showed a similar convergence behavior.

3.3.2 Fixed bed reactor

After having validated the solution to the equations describing mass transfer of adsorption, the next step is to look at a fixed bed reactor with moving solute. The goal here is to validate the combination of the ADE with the source term from adsorption.

In a fixed bed reactor the solute travels from the inlet through the column and accumulates on the adsorbent particles until equilibrium is reached. A distinct concentration front forms as initially all the adsorbate can be removed from the solution, leading to a much lower concentration in most of the bed than at the inlet. The velocity of this concentration front is much slower than that of the fluid and depends (in the ideal case) only on the inlet concentration and the amount of adsorbent in the bed.

For adsorption where kinetics play a role, the equilibrium is not reached instantaneously and a characteristic *mass transfer zone (MTZ)* can be observed. Its shape depends both on the kinetics and the equilibrium [86]. The time it takes for the center of mass of the MTZ to reach the outlet is called *ideal breakthrough time* t_b^id. The balance equation in the ideal case of instantaneous equilibrium is

$$C_0 \dot{V} t_\mathrm{b}^\mathrm{id} = q_0 m_\mathrm{A} + C_0 \phi_\mathrm{B} V_\mathrm{R}\,, \tag{3.19}$$

with V_R as the reactor volume. This gives us the ideal breakthrough time as

$$t_\mathrm{b}^\mathrm{id} = \frac{q_0\, m_\mathrm{A}}{C_0 \dot{V}} + \frac{\phi_\mathrm{B}\, V_\mathrm{R}}{\dot{V}} = t_\mathrm{st} + t_\mathrm{r}\,, \tag{3.20}$$

which can be split into the *stoichiometric time* t_st and the *residence time* t_r. If $t_\mathrm{st} \gg t_\mathrm{r}$, the residence time can be neglected [92]. By substituting the column height h using $V_\mathrm{R} = hC_\mathrm{p}$, the *velocity of the MTZ* can be derived with

$$v_\mathrm{MTZ} = \frac{h}{t_b^{id}} = \frac{C_0 \dot{V}/Q_\mathrm{cs,R}}{q_0 C_\mathrm{p} + C_0 \phi_\mathrm{B}}\,. \tag{3.21}$$

Instead of the common *breakthrough curve (BTC)*, the concentration profile inside the column is used in the analysis. It is just a mirrored BTC but much easier to obtain in a simulation. The axes are related through the travelling velocity of the MTZ. Apart from the general shape, there are two values that are used to analyze the breakthrough behavior. The first is the real breakthrough

time t_b, which is the time at which the outlet concentration first rises, and the second is the stoichiometric time t_st as an approximation of the ideal breakthrough time.

Diffusion, amongst other factors, leads to a phenomenon called axial dispersion in fixed bed reactors. It will lead to a spreading of the MTZ and therefore a flatter breakthrough curve. Many models, including many implementations of the LDF, do not include this term. It is, however, important to keep in mind because the ADEs are used and diffusion cannot be entirely disregarded. There are ways to include the dispersion in the film diffusion coefficient [96] to account for this phenomenon in a model.

Once an equilibrium has been reached and the constant pattern behavior is established, the analytical solution found by [86] for both the Langmuir and Freundlich isotherm applies. Adapted to non-dimensional values [92] an implicit equation for the concentration X is constructed with

$$\frac{R}{1-R}\log(X) - \frac{1}{1-R}\log(1-X) = N_s(-T+1) + \delta_I, \tag{3.22}$$

where the dimensionless quantities T, X, and N_s are used, with

$$T = \frac{t}{t_\mathrm{st}}, \quad X = \frac{C}{C_0} \quad \text{and} \quad N_\mathrm{s} = k_\mathrm{s}^* t_\mathrm{st}, \tag{3.23}$$

and an integration constant δ_I. It is assumed that the residence time t_r can be neglected and only the adsorption equilibrium and initial concentration influence t_{st}. The separation factor R for the Langmuir isotherm is

$$R = \frac{1}{1 + b\,C_0}\,. \tag{3.24}$$

This is the solution to a plug-flow model, meaning dispersion (e.g. diffusion) is not accounted for. The approach used for the current simulation is a dispersed-flow model because it includes a diffusion term.

Analysis method

Eq. (3.22) is implicit and needs to be numerically solved for use in the error calculations. This was done using *scipy's fsolve* function, which uses a modified Powell method [97]. The integration constant δ_I can be found using the material

balance of a BTC. The method is described in [92], which also gives some exemplary values.

Once the constant pattern has been reached, the eventual breakthrough curve has already formed inside the column as the concentration front. The x-axis is transformed to convert between the two. Time and length along the column can be converted by mirroring around x_{st} using $t = 2x_{\mathrm{st}} - x$ and because the dimensionless time $T = t/t_{\mathrm{st}}$ is used with $t = \frac{q_{0,\mathrm{eq}} Q_{\mathrm{cs}} x}{C_0 \dot{V}}$, all factors cancel each other. In combination and additionally centering around $T = 1$ it is

$$T = \frac{t}{t_{\mathrm{st}}} = \frac{2x_{\mathrm{st}} - x}{x_{\mathrm{st}}}, \tag{3.25}$$

where x_{st} is the position of the center of mass of the BTC, approximated as the position x where $C/C_0 = 0.6$. This procedure removes any influence of the outlet boundary on the shape of the breakthrough curve because sampling starts from the center of the column.

Simulation setup

The reactor is realized as a three-dimensional cuboid with periodic boundary conditions on all sides except the inlet and outlet. A constant fluid velocity is set for the entire volume. The phosphate concentration is set to C_0 at the inlet and to zero in the rest of the reactor at the start of the simulation; particle mass concentration is set to $5\ \mathrm{kg\,m^{-3}}$. The particle loading is set for the start in the whole reactor volume to zero. All lattices have Dirichlet boundary conditions at the inlet and Neumann boundary conditions at the outlet. The process parameters are listed in the Table 3.2. The next breakthrough simulations are performed by the cell size of 0.76 mm and ADE relaxation time of 0.5005.

While the adsorbent bulk density may be uncharacteristically low for a fixed bed reactor, it is reasonable for a slurry reactor and reduces the simulation time considerably. The reason is twofold: first, the stoichiometric time t_{st} is proportional to the mass of adsorbent, so more adsorbent means later breakthrough, and secondly, the increased mass of adsorbent leads to larger reaction rates, which have implications for stability. To counteract this, the time step size must be decreased, which leads to a longer simulation time.

Parameter		Value	Unit
Isotherm parameter 1	q_m	20	$\mathrm{mg\,g^{-1}}$
Isotherm parameter 2	b	0.8	$\mathrm{mg\,g^{-1}}$
Inlet concentration	C_0	1	$\mathrm{mg\,L^{-1}}$
Adsorbent concentration	C_p	1	$\mathrm{kg\,m^{-3}}$
Reactor length	L	0.05	m
Reactor width	a	0.016	m
Particle radius	r_p	$3 \cdot 10^{-4}$	m
Surface diffusion coefficient	D_s	$5 \cdot 10^{-11}$	$\mathrm{m^2\,s^{-1}}$

Table 3.2.: Process parameters for fixed bed reactor.

Results

Figure 3.5a shows the concentration profile in the column after 3400 seconds. The stoichiometric time t_st in this case is about 6800 seconds, which leads to the MTZ being roughly centered and enables a clean plot. The intraparticle mass transfer rate $N_\mathrm{s} = 28$ is adjusted to reflect that the breakthrough curve was taken at the midpoint of the column. Had the full length of the column been used, the value would be 56.

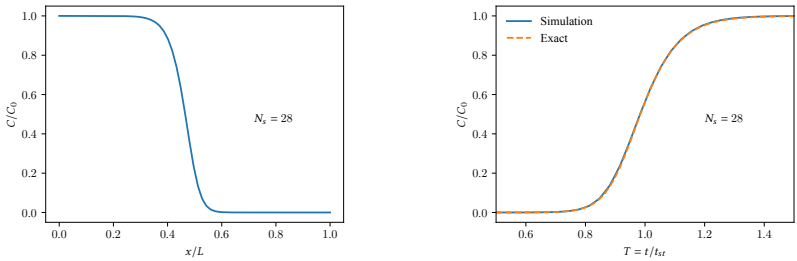

(a) Concentration profile at $t = 3400$s. (b) Breakthrough curve

Figure 3.5.: Concentration profile and breakthrough curve for fixed bed reactor with N=21.

The breakthrough curve that resulted from the transformation previously mentioned is shown in Figure 3.5b. It shows good agreement with the analytical solution. There are no obvious deviations in the shape of the curve. The characteristic shape of a breakthrough curve with dominating surface diffusion

can be seen: the curve is not symmetrical around $T = 1$, instead it is slightly flatter for larger concentrations.

Two ways to align the measured curves and the solution are possible. The first is to calculate the expected position of the center of mass and shift the curve by that value; the second is to try and find the center of mass of the actual measured curve. For symmetrical curves, this point is $0.5\,C_0$. Because in this case surface diffusion dominates, it is actually around $0.56\,C_0$. In this section all plots are aligned using the second method, so that they all cross exactly at $T = 1$, and only the differences in shape are important here. If the expected position and the undertaken approximation from the measured curve are compared, a relative error of around 2% is observed.

The influence of the kinetics and isotherm on the shape can be seen in Figure 3.6a. The surface diffusion mass transfer parameter k_s^* is proportional to D_S and determines the speed of the mass transfer. For larger values, which are shown by the green curve in Figure 3.6a, the curve comes closer to the ideal breakthrough curve with a vertical concentration front. All the curves in

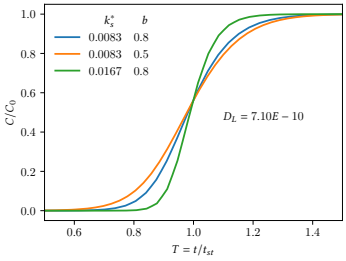

(a) Breakthrough curve in fixed bed reactor with different kinetic and isotherm parameters.

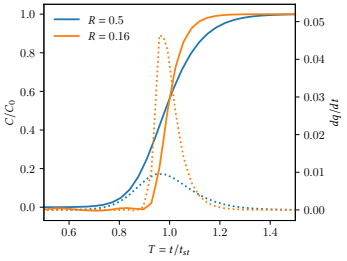

(b) Concentration and source term for different separation factors.

Figure 3.6.: Breakthrough curves for different parameters.

Figure 3.6a show a Langmuir isotherm, where a larger parameter b results in a steeper isotherm. As expected, the orange curve with the smallest value for b is indeed flatter.

Actual implementation allows easy access to the value of the source term at any point in time. This is depicted in Figure 3.6b for two separation factors R. A smaller value for R can be caused by a steeper isotherm or a larger initial concentration. The source term is shown as a dotted line. It is clearly visible that the peak's height as well as the shape of the curve are different. For larger

R, the curve is more asymmetrical with a steeper rise and a longer tail, which is typical for surface diffusion control. This is also visible in the breakthrough curve.

The solution given in eq. (3.22) does not include diffusion. This, however, is impossible to replicate with the approach used in this thesis, since the ADE is solved. The influence of diffusion can be seen in Figure 3.7. For larger values

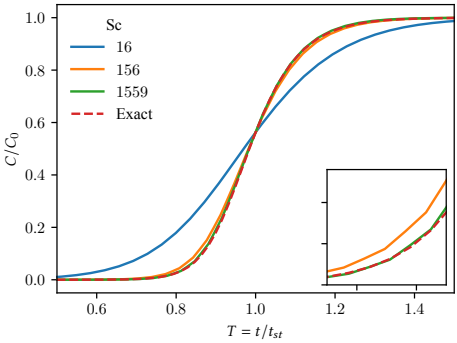

Figure 3.7.: Breakthrough curve for different diffusion coefficients with N=21.

of D (small Sc) the curve flattens and the breakthrough point appears earlier. It can be seen that for value of $D = 5 \cdot 10^{-11}$ m^2 s^{-1}, which corresponds to Sc = 1559, a very good agreement with the analytical solution is already achieved. Although in this example the particles are fixed in place, and therefore the advection part of particles' ADE is irrelevant, diffusion does play a large role. The diffusion coefficient of the loading lattice also has an impact on the result. Since the convergence to $D \rightarrow 0$ is investigated and not any specific substance, all ADE lattices used the same diffusion coefficient.

Convergence

A series of simulations with a fixed diffusion coefficient will in this case not converge to the analytic solution. For this reason Δx, Δt and Sc are scaled together. When scaling in a ratio of 1:1:1, this will keep the relaxation parameter τ constant, similar to diffusive scaling. In this case $\tau_{ADV} = 0.501$. The resulting errors are shown in Figure 3.8a shown over the grid number $N = a/\Delta x$, where a is the column width.

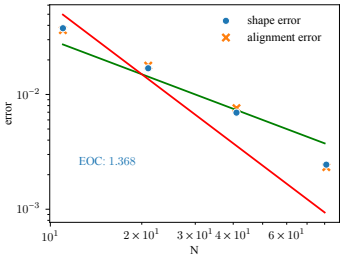

(a) Error for different resolutions N.

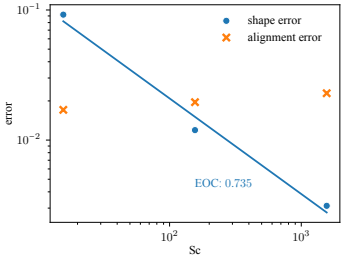

(b) Error for different Sc and fixed resolution.

Figure 3.8.: Error based on shape and position along the column.

It shows both the error caused by differing shapes and the difference in the position of the center of mass of the curve, called alignment error. Surprisingly, they both have very similar values as well as convergence behavior. The *order of convergence is around* 1,37. This means that convergence towards a non-dispersive solution, even when using a dispersed-flow model, is obtained.

Just looking at the fluid diffusion, it contributes an error around order 0,75. Interestingly, the alignment error increases with increasing Sc. This can be seen in Figure 3.8b, which shows the convergence purely based on diffusion with no changes in Δx or Δt, instead with changing relaxation parameters τ_{ADV} ranging from 0,52 to 0,5002.

Fixed bed reactors can be modelled very well by the linear driving force model [88] and the built model demonstrates it as well.

3.3.3 Static mixer

As an example for an industrial application, a static mixer was chosen. This showcases all aspects of the model with moving solute and fluid and moving particles, which means a variable particle concentration. While the linear driving model is especially suitable for a fixed bed reactor, using the modifications proposed in this thesis it can also be applied to such other scenarios. For this significantly more complicated setup, there were no analytical solutions or experimental results available for comparison – nevertheless, it can be used as a more illustrative example of the possibilities of the model.

Simulation setup

The geometry of the mixer can be seen in Figure 3.9. Particles are injected on the left-hand side and the solute on the right side.

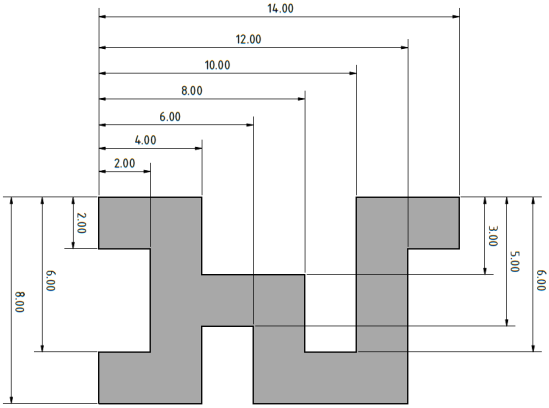

Figure 3.9.: Static mixer with separate inlets for particles (left) and solute (right).

At the upper outlet, a velocity boundary is set with a velocity such that the fluid flows out at the top. The fluid velocity is one-way coupled with the other lattices, effectively dragging the solute and particles with it.

In this setup, the choice of simulation parameters is restricted by coupling demands and stability concerns. The time steps of all lattices need to match, which can only be achieved by carefully selecting the relaxation parameters and diffusion coefficients.

The simulation parameters can be found in the Table 3.3.

Results

The resulting particle loading can be seen in Figure 3.10. It shows a gradual mixing of the two phases and the resulting reaction product. This image shows a steady state, so all particles will experience the loading shown in the image. Because the setup has laminar flow, the mixing is relatively low and particles do not experience fast changing conditions.

Parameter		Value	Unit
Isotherm parameter 1	q_m	20	$\mathrm{mg\,g^{-1}}$
Isotherm parameter 2	b	0.5	$\mathrm{mg\,L^{-1}}$
Inlet concentration	C_0	1	$\mathrm{mg\,L^{-1}}$
Adsorbent concentration	C_p	1	$\mathrm{kg\,m^{-3}}$
Reactor length	L	0.014	m
Particle radius	r_p	$5 \cdot 10^{-5}$	m
Surface diffusion coefficient	D_s	$5 \cdot 10^{-11}$	$\mathrm{m^2\,s^{-1}}$
Film mass transfer coefficient	k_f	$1{,}37 \cdot 10^{-2}$	$\mathrm{m^2\,s^{-1}}$
Relaxation time	τ	0.6125	–

Table 3.3.: Process and simulation parameters for static mixer.

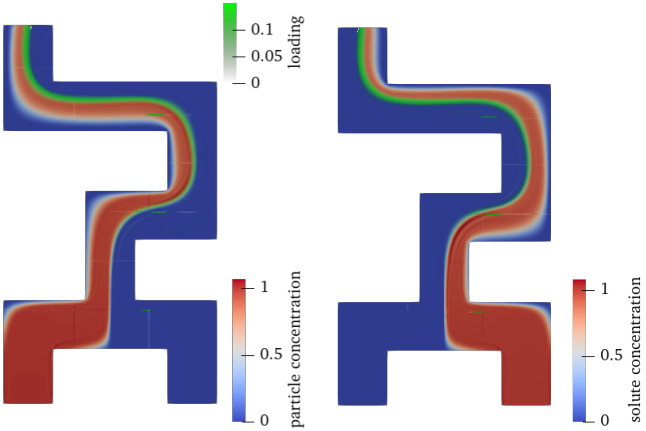

(a) Loading with particle density. (b) Loading with solute concentration.

Figure 3.10.: Loading (green) in a static mixer.

With a setup like this, the limits of the linear driving force model need to be kept in mind. A cyclical absorption and desorption that would occur if particles moved in and out of areas of high solute concentration might not be captured accurately. In this laminar case, this inaccuracy should not be very large, because the particles and solute are coupled to the fluid and move the same way.

In conclusion, the adsorption model can be successfully applied to moving particle systems but it is affected by stability problems of the advection diffusion solution.

With respect to the latter, a closed form equation can be constructed for LBM [98, 99] which reveals the effect of the added relaxation terms. These terms are potentially tunable to balance added numerical diffusion and stability with multiple relaxation time collision [100–103]. Besides, various other efforts to enhance LBM approximations in terms of accuracy and robustness have been proposed for NSE-RADE coupled systems, e.g. via adding correction terms [104, 105], finite difference schemes [106] or (adaptive) filtering [107, 108]. Such optimizations of the here presented model is defered to future studies.

3.4 Summary and answer to the first open question

In this Chapter, steps **S1.1–S1.3** of the numerical analysis (Section 1.3) of the crystallization process at the macroscale are performed. An Eulerian model for adsorption on moving particles using LDF was developed and incorporated into the RADE. The model is discretized using the LBM with separate lattices for fluid, solute, particles, and particle loading. The primary mass transport mechanism describing adsorption is surface diffusion, but both external mass transfer in the form of film diffusion and alternative internal transfer mechanisms, namely pore diffusion, are available as well. Different isotherms are possible as well. Comparison with an analytic solution for the adsorption kinetics in a batch reactor has shown good accuracy. A convergence study showed first-order convergence for the time step number per spatial resolution and EOC of two for the cell size by diffusive scaling. The model predicts breakthrough curves in a fixed bed reactor well, and convergence towards the exact solution was demonstrated. The influence of different adsorption parameters and dispersion caused by diffusion was explored as well.

Finally, the approach was applied to a more complex fluid flow problem in a static mixer with moving particles to demonstrate its potential for use in investigations of the influence of fluid flow on adsorption performance.

In conclusion, the built model can be considered as valid and suitable for use in an algorithmic optimization solver. All provided equations are differentiable, which is a crucial requirement for algorithmic sensitivity assessment. The first main question at the macroscale is:

Q1: Which crystallization process parameters are significant and can be optimized by a stirred tank crystallization reactor?

In this concrete case of a crystallization reactor, it can be stated that the following parameters can be adjusted: particle size and porosity by choosing different types of CSH microparticles, carrier fluid velocity, and concentration of particles. The concentration of phosphate is predefined by the process steps before the crystallization reactor. The addition of some concentration of pH-changing species (acids or bases) that do not react with phosphate or CSH microparticles can also improve phosphate adsorption [5]. Diffusion coefficients in different mass transfer steps are taken from experimental measurements, as well as the adsorption isotherms. The named parameters can be optimized or derived from known experimental measurements using the optimization solver already validated by Ito *et al.* [109]. Thereby, the model presented here is combined with gradient-based optimization and is validated using a benchmark batch reactor case with both analytical and simulated data. Results show grid independence with simulated input and second-order convergence with analytical input. The framework for inverse problems accurately recovers the isotherm constant, reducing the initial error to machine precision. The same solver can be used for optimization of chosen parameters.

To understand whether parameters such as diffusion constants and macroscopic reaction kinetics constants are modifiable or predictable without complex experiments, modeling and simulation at smaller scales are required. This will be covered in the next two chapters.

4 Modeling and simulation at the micro-level

This Chapter is partially based on a published article:
***Bukreev, F.**, Kummerländer, A., Jeßberger, J., Teutscher, D., Simonis, S., Bothe, D., Krause, M. J. (2024). Benchmark Simulation of Laminar Reactive Micromixing Using Lattice Boltzmann Methods. AIAA Journal, DOI: 10.2514/1.J064234*

Description of the used application code is given in the Section A.2.2.1.

The aim of this Chapter is to answer how the species mixing and reaction processes can be correctly calculated. As soon as the size of the CSH particles used in the P-RoC process is microscopic as well as the relevant length scale for the mass transport, the two named phenomena should be accurately predicted at this scale.

As mentioned in the Introduction (Chapter 1), firstly, the multicomponent Eulerian model is built and validated by re-establishing the T-micromixer benchmark, conducting the 3D simulation approaching the resolution of the Batchelor scale. After that, the same model with LES extension for the carrier fluid is applied to a turbulent micromixer.

The T-shaped micromixer is the most simple setup. Correspondingly, it has received close experimental and numerical attention [110]. The cell size is the most important parameter and main obstacle for the highly resolved calculations. The resulting fine meshes exceed the capabilities of local workstations and thus are only seldomly used. Existing FVM CFD software also reaches their limit at some mesh size. The discretized integration over each cell by FVM requires communication with other cells, implying permanently increas-

ing computation costs and loss of efficiency. An overview of existing CFD publications regarding T-micromixers is provided in Table 4.1.

Publication	Cell size [μm]	N_{cell} (cut)	Discretiz.
Bothe *et al.* [111]	0.3 to 2.5	*	FVM
Galletti *et al.* [112]	25	3200	FVM
Lobasov *et al.* [113]	5	3200	FVM
Tokas *et al.* [114]	3, 33	1800	FVM
Fonte *et al.* [115]	25	1600	FVM
Jeßberger *et al.* [116]	12, 31	19199	LBM

* adaptive refinement in direction of the concentration gradient

Table 4.1.: Comparison of fine resolved simulations of T-micromixers in the literature.

It can be noticed that the used cell sizes are in most cases much larger than the Batchelor length scale, especially at high Schmidt numbers ($Sc > 1000$), which is why they cannot be called DNS in the sense of the coupled transport equation. Numerical diffusion compromises the accuracy of simulations and makes the realistic visualization of concentration vortices impossible. Bothe *et al.* [111, 117, 118] managed to resolve the computation domain with adaptive refinement on a 2D lattice even below the $0{,}25\,\mu\text{m}$. The velocity field in the micromixer was calculated using the 3D FVM simulation in the mixing zone and using the exponential extrapolation of the secondary flow field after the mixing zone in the flow direction. Subsequently, the RADEs were numerically solved in the 2D sections. The performed literature analysis does not show any existing CFD simulation of the 3D micromixer with cell size equal to or below the Batchelor scale.

The LBM is used in the current research because of its unique amenability to massively parallel execution on modern high performance computers. In this work, the reactive T-micromixer setup, as considered firstly by Bothe *et al.* [111, 117, 118], is computed in a series of ULES refining till DNS with LBM utilizing up to 160 state-of-the-art GPUs of the HoreKa supercomputer using *OpenLB*'s transparent GPU support [9, 119]. The Dean vortices are investigated and qualified by an extra finely resolved structured lattice and relatively high Knudsen number. The very low diffusion coefficients (10^{-10} to $10^{-9}\text{m}^2\,\text{s}^{-1}$) are treated locally by a special Schmidt number-based stabilization method, similar to the Smagorinsky–Lilly ansatz [47, 48]. To the knowledge of the authors, this is the first Schmidt number-based stabilization method for LBM

applied to micromixing simulations. Moreover, the influence of the resolution on the average product concentration is examined in a convergence study (Table 4.4).

The Chapter is structured as follows. Section 4.1 summarizes the methodology used for the computations. Section 4.2 describes the considered micromixer setup, physically and numerically. The computational results are presented and discussed in Section 4.2.6. Afterwards, the simulation model with an additional turbulence model by carrier fluid is applied to a turbulent micromixer in Section 4.3. Finally, answer to the question **Q2** is given in Section 4.4. In this Chapter, the steps **S1.1–S1.3** are performed on a microscopic application.

4.1 Simulation model

In this work, a coupled system of incompressible NSE (Eq. 2.9, 2.10 without force) and RADE (Eq. 2.11 with $s = C_i$ and $Q_s = \upsilon_i R$) is numerically solved, complemented with initial and boundary conditions. In this model, the carrier fluid density remains constant and is not affected by the solved species. The fluid velocity is computed by the mass and momentum conservation equations and inserted in the RADE. Further, the kinematic viscosity is assumed to be constant. The concentration field C_i is calculated for each species separately with the corresponding diffusion coefficient $D_i > 0$, stoichiometric coefficient υ_i, and reaction rate R common for the whole reaction.

The system of equations (2.9), (2.10), (2.11) are discretized with LBM (Tables 2.1, 2.2) on the $D3Q19$ lattice for NSE and $D3Q7$ lattice for ADEs (cf. Figures 2.3c and 2.3b).

4.1.1 Schmidt number stabilization

For a stable simulation run using LBM for approximating nonlinear partial differential equations with diffusion terms, it is necessary to ensure that the relaxation time is always greater than 0.5 [98, 99]. Due to the low diffusion coefficients of the transported species, ranging from 10^{-10} to $10^{-9}\mathrm{m}^2/\mathrm{s}$, the RADE simulation becomes unstable and diverges in cells experiencing high shear stress. In the case of a laminar micromixer, turbulence is not an issue, but *the existing Dean vortices induce high shear stress* S *between the flow layers*. In

these regions, the artificial stabilization viscosity is calculated using *the Schmidt number-based stabilization approach*, for the first time applied to a laminar flow (Section 2.1.4). Smagorinsky constant C_{S} and stabilization Schmidt number $\mathrm{Sc}_{\mathrm{st}}$ take values between $0.1 - 0.2$ and $0.001 - 0.654$, respectively, depending on the cell size. D_i is increased where the simulation stability is endangered due to a strong shearing counter-flow. The cells without this kind of flow feature retain their molecular diffusivity. The overall accuracy of the species transport is high enough to reproduce the experimental and reference values, which is shown in the remainder of this Chapter.

4.2 Laminar reactive T-micromixer

In this work, a *simple one-way reaction of second order* is considered based on the publications of Bothe *et al.* [111, 117, 118] and Lojewski [120].

$$A + B \xrightarrow{k_{\mathrm{f}}} C \tag{4.1}$$

The corresponding reaction rate R is then $k_{\mathrm{f}} C_A C_B$, where k_{f} is the forward reaction rate constant with a value of $10^5\ \mathrm{m^3\,mol^{-1}\,s^{-1}}$ that is held unchanged in the current research. The stoichiometric coefficients of the educts υ_A and υ_B are -1, whereby the υ_C is $+1$. The simulated T-shaped micromixer has the following dimensions: two $100 \times 100 \times 300\ \mu\mathrm{m}$ inlet channels from the sides and $100 \times 200 \times 1600\ \mu\mathrm{m}$ mixing channel in the center (Figure 4.1).

4.2.1 NSE boundary conditions

Through the Dirichlet inlets of the micromixer, the carrier fluid is streaming with a Poiseuille type velocity profile given by the formula

$$u_n(x_p, y_p) = 16 U_{\max} \frac{x_p (l_x - x_p) y_p (l_y - y_p)}{l_x^2 l_y^2}. \tag{4.2}$$

Here, u_n is local velocity normal to the plane at plane coordinates (x_p, y_p). It is calculated from the maximal inlet velocity U_{max} and inlet plane dimensions l_x, l_y. The maximal velocity is chosen such that the Reynolds number in the mixing channel is 186 as in [111]. At the outlet, the constant zero Dirichlet boundary condition for pressure (fixed pressure difference value of zero or

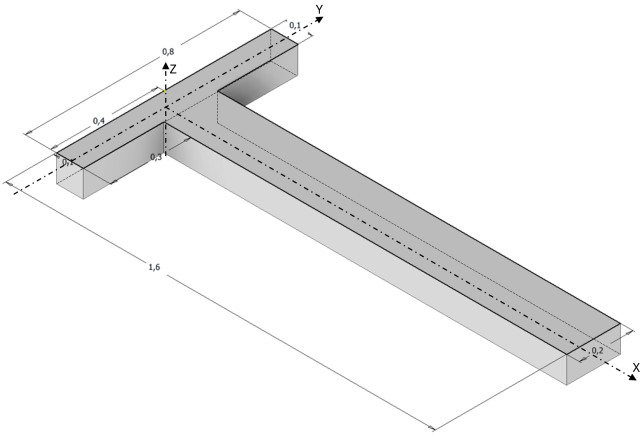

Figure 4.1.: T-micromixer geometry [111] used in the present study.

fixed lattice density of one in lattice units) and Neumann boundary condition for velocity are set.

4.2.2 RADE boundary conditions

Each reaction component is simulated on its own *D*3*Q*7 lattice. The educt *A* enters through the left inlet with constant concentration $1\,\mathrm{mol\,m^{-3}}$ (*B* set to zero), whereas the educt *B* is set to $0{,}001\,\mathrm{mol\,m^{-3}}$ at the right inlet (*A* set to zero). The product *C* does not exist at the inlets (concentration set to zero) and appears only due to the reaction in the mixing channel. The mixer outlet is modeled via the Neumann boundary condition.

4.2.3 Material properties

The carrier fluid is water with a density of $1000\,\mathrm{kg\,m^{-3}}$ and a kinematic viscosity of $1.002 \cdot 10^{-6}\ \mathrm{m^2\,s^{-1}}$. The diffusion coefficients of the species *A*, *B*, and *C* are $1.6 \cdot 10^{-9}$, $2 \cdot 10^{-10}$ and $2 \cdot 10^{-10}\ \mathrm{m^2\,s^{-1}}$ accordingly. The Schmidt numbers are then 626, 5010, and 5010.

4.2.4 Simulation parameters overview

The NSE is computed until a physical time of $0{,}0257\,\mathrm{s}$ to reach a steady state with secondary flow. During this, the RADEs are calculated for the last $0{,}01\,\mathrm{s}$ until reaching the steady state as well. The overview of boundary conditions, material and chemical properties used in the simulation is summarized in Table 4.2. The calculation was performed with different resolutions, corresponding relaxation times, and stabilization parameters (Table 4.3). The chosen size of C_S and Sc_{st} corresponds to minimal added artificial diffusion needed for a stable, non-divergent simulation. Their values were found by a separate study performed in terms of the current research. The overview of simulation size and achieved efficiency on distinct numbers of GPUs NVIDIA A100 is shown in Table 4.4.

Variable	Value	SI units	Variable	Value	SI units
Left inlet (-Y)			Right inlet (+Y)		
$U_{\max}$	2.94	$\mathrm{m\,s^{-1}}$	$U_{\max}$	2.94	$\mathrm{m\,s^{-1}}$
p	$\nabla p = 0$	Pa	p	$\nabla p = 0$	Pa
C_A	1	$\mathrm{mol\,m^{-3}}$	C_A	0	$\mathrm{mol\,m^{-3}}$
C_B	0	$\mathrm{mol\,m^{-3}}$	C_B	0.001	$\mathrm{mol\,m^{-3}}$
C_C	0	$\mathrm{mol\,m^{-3}}$	C_C	0	$\mathrm{mol\,m^{-3}}$
Outlet			Material properties		
$\nabla \cdot \boldsymbol{u}$	0	$\mathrm{m\,s^{-1}}$	ν	$1.002 \cdot 10^{-6}$	$\mathrm{m^2\,s^{-1}}$
p	0	Pa	ρ	1000	$\mathrm{kg\,m^{-3}}$
C_A	0	$\mathrm{mol\,m^{-3}}$	D_A	$1.6 \cdot 10^{-9}$	$\mathrm{m^2\,s^{-1}}$
C_B	0	$\mathrm{mol\,m^{-3}}$	D_B	$2 \cdot 10^{-10}$	$\mathrm{m^2\,s^{-1}}$
C_C	0	$\mathrm{mol\,m^{-3}}$	D_C	$2 \cdot 10^{-10}$	$\mathrm{m^2\,s^{-1}}$
Chemical reaction properties			Simulated physical times		
ν_A	-1	–	t_{NSE}	0.0257	s
ν_B	-1	–	t_{RADE}	0.01	s
ν_C	1	–			
k_{f}	10^5	$\mathrm{m^3\,mol^{-1}\,s^{-1}}$			

Table 4.2.: Simulation boundary conditions and material properties.

Cell size [µm]	$\triangle t$ [µs]	C_S	Sc_{st}
3.33	0.119048	0.2	0.001
0.83	0.029761	0.2	0.035
0.42	0.014881	0.2	0.094
0.28	0.009920	0.1	0.431
0.22	0.007936	0.1	0.654

Table 4.3.: Relaxation times and stabilization parameters.

$\triangle x$ [µm]	N_{cell}	N_{GPU}	MLUPs*	t_{sim} [h]
3.33	$1.08 \cdot 10^6$	4	1400	0.06
0.83	$6.91 \cdot 10^7$	12	3681	3.04
0.42	$5.53 \cdot 10^8$	21	8200	28.6
0.28	$1.87 \cdot 10^9$	100	53512	22.3
0.22	$3.65 \cdot 10^9$	160	68340	34.3

* MLUPs: Millions of Cell Updates per Second

Table 4.4.: Computation parameters.

4.2.5 Simulation algorithm

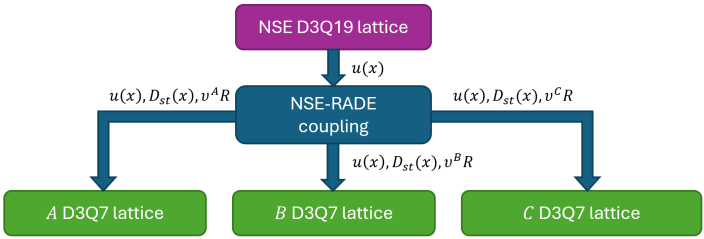

Figure 4.2.: Simulation system with dependencies.

Algorithm 1 Global time step *// Strang splitting assumption*

for each lattice point **do**
  if $t < 0.02 \cdot t_{\mathrm{NSE}}$ **then**
    Updating of velocity boundary conditions at inlets from 0 till U_{max}
  end if
  Collision and streaming for NSE lattice
  for each specie j **do** *// Coupling*
    Compute $D_{\mathrm{mol},j} + D_{st}$
    Compute $v_j R$
  end for
  if $t \geq (t_{\mathrm{NSE}} - t_{\mathrm{RADE}})$ **then**
    for each specie j **do**
      Collision and streaming for RADE lattice of corresponding specie j
    end for
  end if
end for

4.2.6 Results

Firstly, the described setup is validated against the results of Bothe *et al.* [111]. Subsequently, the simulation outcomes obtained at the finest resolution are discussed and analyzed.

4.2.6.1 Validation

The performed simulations are validated visually and numerically against the data given in publications of Bothe *et al.* [111] and Lojewski [120]. The results of NSE and RADE can be validated separately. For the NSE verification, the pressure distribution and magnitude of the secondary flow along the micromixer axis are compared numerically to the FVM simulation of Bothe *et al.* [111] (Figure 4.3). The streamlines at the beginning of the mixing zone are visually compared to the results of Lojewski [120], cf. Figure 4.4.

The magnitude of the secondary flow is computed cell-wise as $\sqrt{u_y^2 + u_z^2}$, where u_y and u_z are velocities parallel to the mixer cross-sections, and then averaged

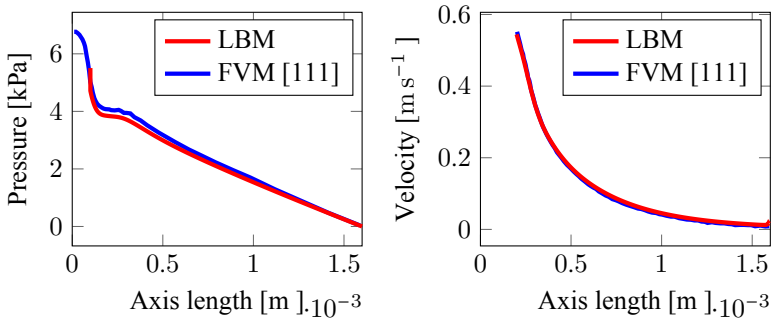

(a) Pressure along axis (b) Secondary flow magnitude along axis

Figure 4.3.: Numerical validation of NSE simulation results at $t = 0.0257$ s and $\triangle x = 0.22$ µm.

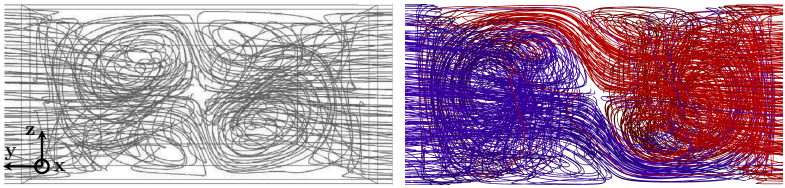

(a) FVM [120] (b) LBM

Figure 4.4.: Comparison of streamlines in the beginning of mixing zone at $t = 0.0257$ s and $\triangle x = 0.22$ µm.

along the mixer axis. The streamlines from the LBM simulation are marked with different colors for flows from distinct inlets.

The numerical and visual comparison of FVM and LBM NSE simulation results shows a good agreement between the data, which is why the RADE calculations can be now juxtaposed. They are also compared optically and numerically. The experiment shot shown in the figure 4.5 (a) is the distribution of a tracer taken by the laser induced fluorescence (μ-LIF) combined with micro-resolution confocal microscopy. The picture (b) is the middle slice of the FVM simulation performed for a single component with Sc = 3600. The LBM (c) result shows the distribution of the component A with Sc = 626.25. Although the molecular diffusivity in the LBM simulation is higher than in the FVM one, the numerical diffusion is much lower due to a higher uniform resolution. That is why the right picture is optically sharper than the central figure. The position of the Dean

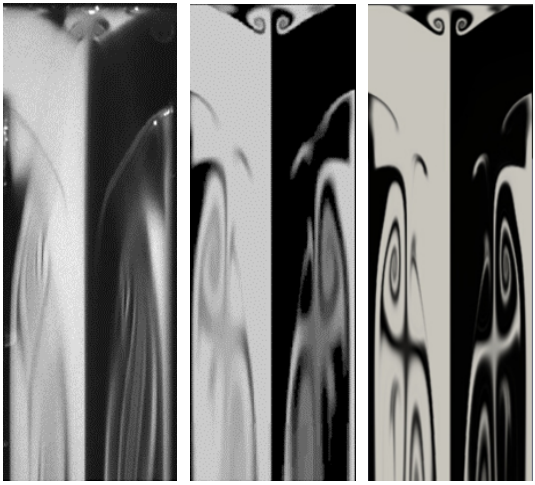

(a) Experiment [117] (b) FVM [117] (c) LBM

Figure 4.5.: Comparison of the tracer distribution in the middle slice of the micromixer, where LBM results are plotted at $t = 0.0257$ s and $\triangle x = 0.22$ µm.

vortices is the same in all three pictures; their form is also similar. The next image is a cross section of the mixing zone at the 750 µm axis length colored with species *B*. *The figures are very similar* even though the FVM simulation

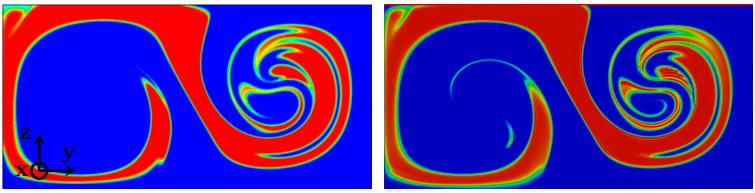

(a) FVM [111] (b) LBM

Figure 4.6.: Comparison of the component *B* distribution in the mixer cross section at 750 µm axis length at $t = 0.0257$ s and $\triangle x = 0.22$ µm.

is done on the 2D mesh of this concrete cross section with extrapolated velocity values and RADE computed therewith and cell size of 0,156 25 µm. The LBM upshot is a slice of the 3D lattice of the whole micromixer with a uniform cell size of 0,22 µm.

The numerical evaluation of the product C average concentration shows a stronger difference between FVM and LBM simulations (Figure 4.7). The

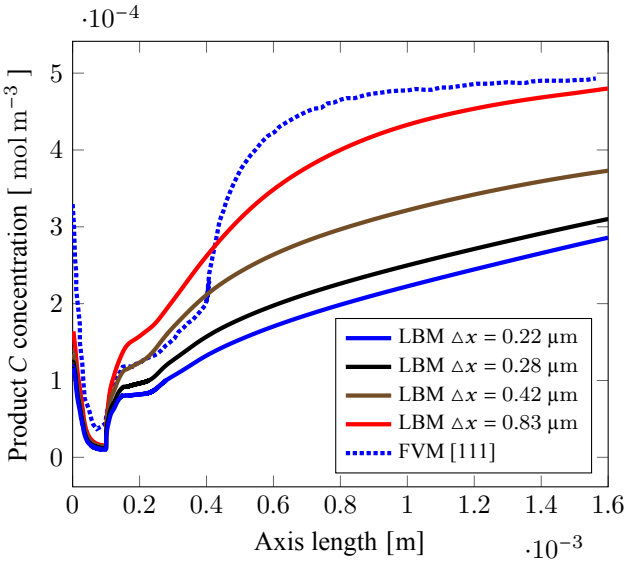

Figure 4.7.: Numerical comparison of RADE simulation results at t = 0.0257 s.

FVM concentration curve starts a rapid growth after $400\,\mu\mathrm{m}$ because of a coarse grid in this region with a uniform cell size of $2{,}5\,\mu\mathrm{m}$. The LBM results show a decrease in the product concentration with lattice resolution refinement. It is caused by the shrinkage of the artificial numerical diffusion of components, which is why the overlap of educts A and B is thinner and the reaction outcome is smaller. *The complete prevention of this diffusion can be achieved only by resolving the computational domain finer than the Batchelor scale.*

4.2.6.2 Discussion

The comparison of experimental, FVM, and LBM simulation data allows one to state that the setup developed in the current research is correct and verified.

The added artificial diffusion used for the stabilization of the simulation is plotted in Figure 4.8. The added diffusion is taken along the central axis

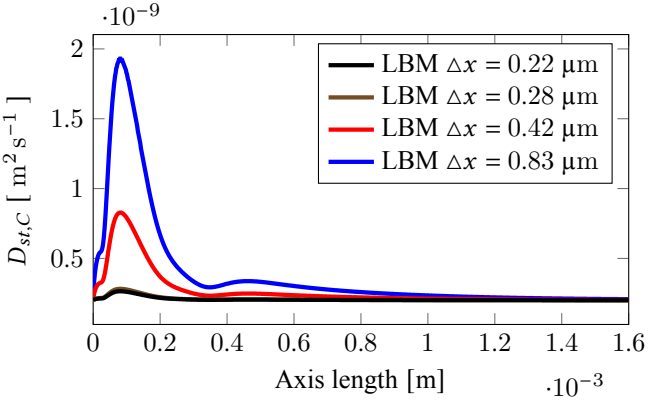

Figure 4.8.: Added diffusion D_{st} to the reaction product locally along the mixer axis at t = 0.0257 s.

of the micromixer, where two flows from different inlets come together and create a zone of the highest shear stress in the simulation. The molecular diffusion coefficient of the reaction product C is $2 \cdot 10^{-10}$ $m^2 s^{-1}$. *Even for the finest cell size, the added numerical diffusion becomes* 1.25 *times higher than the molecular one.* That fact determines all the conducted simulations to the category of ULES in the sense of the transported species flow structures, which are still the finest as far as the authors know.

The necessity of such a fine resolution can be seen as well in the visualized cell edges on one vortex in the beginning of the mixing zone (Figure 4.9). The

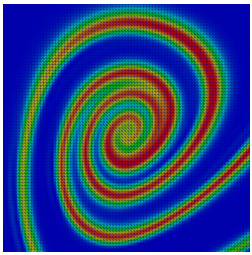

Figure 4.9.: Resolved concentration vortex in the middle slice of micromixer at t = 0.0257 s and $\triangle x$ = 0.22 µm.

species concentration curves are only four cells wide at the thinnest regions,

even by the cell size of 0,22 µm. *A coarser grid would discard information of that vortex, which is why the scaling power of a LBM simulation is vital for the starting section of the mixer.* The LBM simulation at high resolutions leads to the most precise species distributions in the microreactor.

An important setting in the current simulations is the choice of the C_S and Sc_{st}. In the Figures 4.10 and 4.11 is shown on the left an example of divergent RADE simulation by a too high stabilization Schmidt number. On the right side is a plot with two curves that display how the product concentration increases through higher artificial diffusion by a too high Sc_{st}.

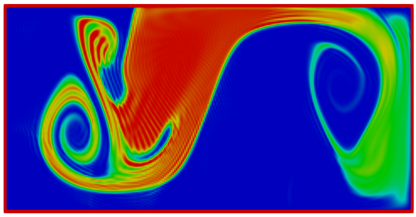

Figure 4.10.: Concentration of species B on a cross section at 250 µm with $\triangle x = 0.83$ µm and $Sc_{\mathrm{st}} = 0.3$.

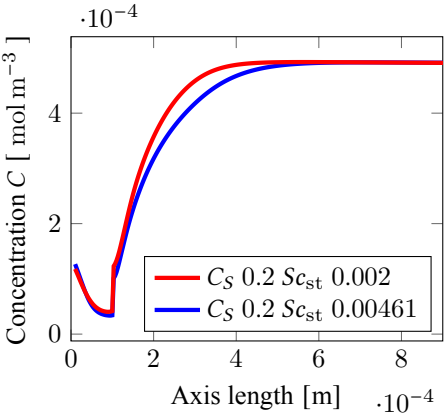

Figure 4.11.: Effect of varying Sc_{st} on concentration profiles with $\triangle x = 3.33$ µm.

Since one goal of this work is to reestablish a T-micromixer benchmark, the detailed evaluation of the species concentrations along different axes of the

micromixer at the finest resolution can be found in the **Supplementary materials** of the published paper [35]. *The gained precise simulation results can be used as a newly re-established benchmark case for reactive micromixers.*

4.3 Turbulent impinging jets micromixer

Description of the used application code is given in Section A.2.2.2.

The algorithm described in the previous Section and applied to a laminar T-shaped micromixer can also be used for the calculation of turbulent mixing flows. For that, a ULES is also applied to a turbulent micromixer with confined impinging jets.

The micromixer tested with turbulent flow is described by Johnson & Prud'homme [24]. The geometry used is shown in Figure 4.12.

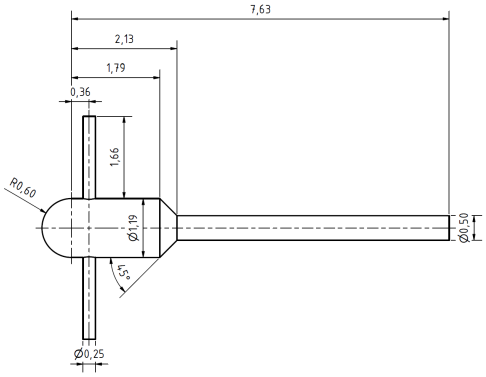

Figure 4.12.: Turbulent micromixer geometry.

The micromixer was simulated using water at a Reynolds number of 3000 and a Smagorinsky constant of 0.15. A vortex method boundary was applied at both inlets [121], with a turbulent intensity of 5%, while a Neumann boundary condition was imposed for pressure. The no-slip boundary conditions were enforced on the walls, while the outlet used a Dirichlet boundary condition for pressure set to 0 Pa and a Neumann condition for velocity.

The chosen spatial resolution was 2.5 μm, resulting in a total of approximately $247 \cdot 10^6$ lattice points. The collision operator used for the NSE simulation was the Smagorinsky-modified BGK operator, with a lattice relaxation time of 0.51.

Parallel to the NSE simulation, an ADE lattice was computed to evaluate the feasibility of the ADE stabilization technique in the turbulent regime. Scalar values of -0.5 and $+0.5$ were applied to the inlets. Zero-gradient conditions were used on the walls, and a Neumann boundary condition was imposed on the outlet. The Schmidt number for the ADE was set to 1000, while the turbulent Schmidt number for stabilization was set to 0.05.

After the development of the ”quasi-steady” turbulence, the scalar distribution in the middle cut of the mixer takes the following form:

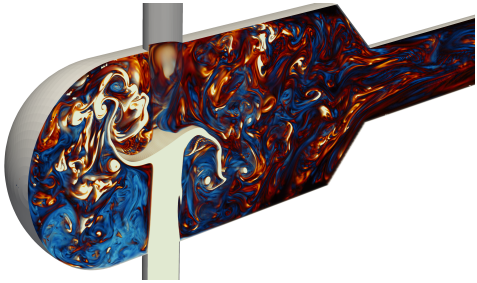

Figure 4.13.: Instantaneous ADE scalar distribution in the turbulent micromixer.

The simulation results demonstrate the successful effectiveness of the ADE stabilization approach in turbulent conditions. The current mixer was optimized for efficient calculation on CPU-GPU machines [122].

4.4 Summary and answer to the second open question

In this Chapter, steps **S1.1–S1.3** of the numerical analysis (Section 1.3) of homogeneous mixing and reaction at the microscale are performed. To reproduce mixing and reaction processes at that scale, an Eulerian NSE-RADE model, similar to the model from the Chapter 3 is built and validated on a laminar reacting T-micromixer benchmark, whereafter it is extended with the Smagorinsky turbulent model for carrier fluid and applied to a turbulent micromixer.

The micromixers are chemical devices for precise mixing and reaction of species. The fluid dynamics inside of a microdevice is a complex process which can be analyzed and designed only by means of LES that narrows the hydrodynamic scale of the transport equation. That requires the calculation of large meshes with fine cell size around the Batchelor length scale, which can be orders of magnitude smaller than the Kolmogorov length scale, depending on the Schmidt number, i.e., on the species diffusivities. The most popular FVM CFD softwares allow one to simulate only limited cell numbers in reasonable times, so that the computational domain needs to be very small or there must be applied some mathematical simplifications. In contrast to that, the LBM implemented in *OpenLB* allows parallel calculations on HPC clusters with multiple GPUs due to the fully local simulation algorithm and code optimization.

In this chapter, a T-micromixer with a simple reaction of second order and Reynolds number of 186 is simulated within *OpenLB* and validated against the published data of Bothe *et al.* [111] and Lojewski [120]. The instabilities induced by a high shear rate between the rotating Dean vortex layers and low relaxation numbers are locally compensated with a stabilization Schmidt number-related artificial additional diffusivity. The comparison of NSE and RADE results with experiment and published FVM simulation data shows good agreement. The simulation data provided (see the **Supplementary materials** in [35]) can be used as a new and precise benchmark for similar CFD applications or software libraries.

In addition, a feasibility study of the Schmidt number stabilization method in turbulent flows coupled with ADE is performed in the turbulent micromixer of impinging jets [24]. Thereby, the SGS turbulence model is applied to NSE. The study has shown successful functionality of the stabilization approach. In the future works, the turbulent micromixer will be validated on the results of [24].

The second main question of the thesis is

Q2: Reaction happens at the level of microparticles within their nanopores, so how can the species mixing and reaction be correctly predicted?

In this Chapter, it has been shown that the transported species with low diffusivity generate flow structures reaching nanoscale, depending on the specific

Batchelor scale. To predict the mixing efficiency or reaction conversion correctly, simulation should be resolved close to this scale, being LES or DNS from the ADE point of view. To stabilize ADEs in the regions with high shear stress, an appropriate stabilization or turbulent Schmidt number for the ADE stabilization should be found. At the coarse resolutions, the added diffusion in these regions becomes much higher than in the cells with weaker shear stress (see Figure 4.8). By lower additional diffusion, the simulation starts to diverge (Figure 4.10). From some cell number, it is impossible to resolve finer, which is why for the future works the species concentration produced by the numerical diffusion can be subtracted from the transport equation.

$$Q_s = v_i R - D_{\mathrm{num}}(\triangle x)\Delta C_i, \tag{4.3}$$

where the second spatial derivative of specie concentration can be computed using FDM. The numerical diffusion is dependent on the current spatial resolution of the simulation and the approach how to calculate the numerical diffusion constant D_{num} should be found in future studies.

Thinking about the macroscopic full-size reactor simulation, transport of the particulate phase with ADE can also be extended by this correction term.

The microscopic simulation does not give insight into the crystallization reaction kinetics happening inside of the nanoscopic pores that are not resolved at the currently described stage. This insight will be developed in the next Chapter.

5 Modeling and simulation at the nano-level

This Chapter is based on published articles:

***Bukreev, F.**, Kummerländer, A., Jeßberger, J., Teutscher, D., Ito, S., Simonis, S., Dapelo, D., Nezhad, M. M., Nirschl, H., Krause, M. J. (2025). A Hybrid Lattice-Boltzmann Model for Hydro-Electrochemical Modeling and Sensitivity Analysis of Crystallization Potential in Nanoporous Media. Part I: Simulation Model. Engineering with Computers, 2025, ISSN: 1435-5663. DOI:10.1007/s00366-025-02216-x*

***Bukreev, F.**, Kummerländer, A., Jeßberger, J., Teutscher, D., Ito, S., Simonis, S., Dapelo, D., Nezhad, M. M., Nirschl, H., Krause, M. J. (2025). A Hybrid Lattice-Boltzmann Model for Hydro-Electrochemical Modeling and Sensitivity Analysis of Crystallization Potential in Nanoporous Media. Part II: Application to the Identification and Quantification of Influencing Factors of Phosphate Saturation. Engineering with Computers, 2025, ISSN: 1435-5663. DOI:10.1007/s00366-025-02217-w*

The last main question (**Q3**) from the Section 1.2 requires the development of a nanoscopic simulation model of the crystallization reaction on the pore surface and coupling of this model with a sensitivity calculation approach to get the influence strength of distinct parameters, which is realized in the Section 5.1. After that, the created model is applied to simplified 2D and realistic 3D porous geometries for the definition of OCP oversaturation dependencies (Section 5.2). In this Chapter, the steps **S1.1–S2.3** are performed on a nanoscopic application.

5.1 Electrochemical hydrodynamics simulation approach

In this Section, the development of a sensitivity assessing LBM-based Eulerian solver for surface electrochemical processes on the example of crystallization in the nano-pores is presented. The numerical simulation of this phenomenon is typically based on a crystallization model, a system of equations describing the species dynamics in the surrounding liquid bulk, and its numerical discretization. Physical adsorption with subsequent crystallization as an example of a standard pore-scale chemical process can be divided into the 6 general steps already listed in the Section 1.3.1 and schematically visualized in the Figure 1.3.

The present work considers the first four steps. To do so, the chemical species are modeled as ions that are influenced by fluid motion and an electric field. Previously, Kler *et al.* [123] have investigated the electrodynamic system on a microfluidic chip using finite element methods with a free-slip boundary condition for the carrier fluid motion. Barnett *et al.* [124] discretized the pore-scale electrochemical ionic flow, described by the Stokes-Poisson-Nernst-Planck equation system, using the finite volume method. Fuel cells with multiphase (water/air) flow and dissolved ions have been modeled with the LBM by Ryan *et al.* [125]. An LBM discretization of a full set of formulations describing an electro-reactive system with chemical-reaction-driven phase change has been presented by Zhang and Wang. [126] and used to model precipitation and dissolution cases. Notably, the use of LBM has become popular in battery modeling [127, 128]. The electro-kinetic system discretized with LBM was also validated analytically by Tian *et al.* [129]. The principles of electric double layer (EDL) theory relevant to surface reactions at the nano- and micro-levels can be found in [130]. Nevertheless, these surface reactions have not yet been investigated numerically at the pore level considering the full system complexity, i.e. hydro-, electro-, and chemo-dynamics. This work intends to fill this research gap by presenting an integrated model within the LBM framework. As LBM is well-suited for modeling nano- and micro-level multiphysics problems [40, 56, 131–133] due to its capability to efficiently simulate such systems, leveraging its parallelizability and the simplicity of its algorithm [73, 119].

In the current Section, the electro-dynamic model for a nanoscale porous geometry is proposed (Section 5.1.1). The three-dimensional model is discretized with LBM and coupled to the AD algorithm (Section 5.1.2). In Section 5.1.4.2

the system components are validated step-wise on analytical solutions. Starting with Poisson equation solver validation, going through Poisson-Nernst-Planck system, and ending by electro-osmosis analytical example computed using the Navier–Stokes–Poisson–Nernst–Planck equation system. Section 5.1.4.2 presents the validation of the AD sensitivity calculation approach against a set of results achieved from FDM. To the best of the author's knowledge, there is no tool for automatic sensitivity analysis of adsorption or saturation reaction systems at the pore-level.

5.1.1 Methodology

5.1.1.1 Governing conservation equations

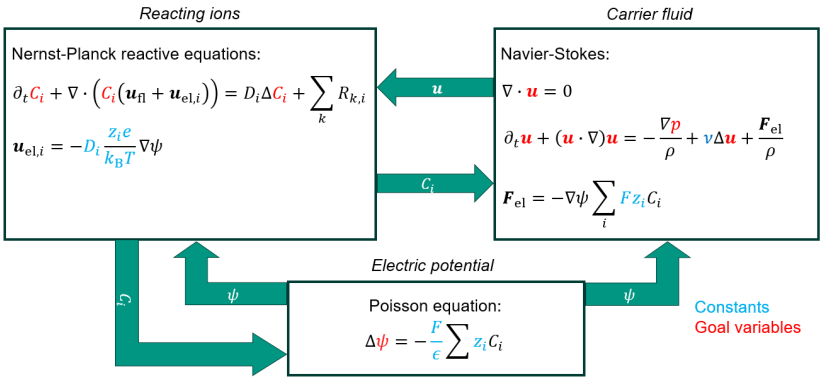

Figure 5.1.: Full Eulerian equation system.

The model development starts with choosing the global approach, which is in the current case the Eulerian ansatz with bidirectional coupling and Strang splitting assumption. It means that inside one time step, variables from other equations are held constant during the solution of the current equation. There is only one liquid phase with three solved ionic components without explicit interface modelling. Each ion is indicated by i. Its concentration C_i is distributed by diffusion, which is described by the diffusion coefficient D_i, and by advection, which consists of movement induced by the carrier fluid $\boldsymbol{u}_{\mathrm{fl}}$ and by the electric field $\boldsymbol{u}_{\mathrm{el},i}$. In the boundary cells, ion concentration is changed

by summarized reaction terms $\sum_k R_{k,i}$, where k is the reaction index. So, the *sourced ADE* (Equation 2.11) gets $s = C_i$, $\boldsymbol{u}_{\mathrm{ad}} = \boldsymbol{u}_{\mathrm{fl}} + \boldsymbol{u}_{\mathrm{el},i}$, and $Q_s = \sum_k R_{k,i}$. This equation type is called *reactive Nernst-Planck equation (RNPE)*.

The carrier fluid velocity is taken from the usual *incompressible NSE* forced by electric term $\boldsymbol{F} = \boldsymbol{F}_{\mathrm{el}}$ as well (Equations 2.9, 2.10). Assuming relatively small concentrations of ions, the liquid characteristics are left unchanged.

The electric field is computed in the form of the potential difference ψ described by the *PE* (Equation 2.12), where $s = \psi$ and the source $Q_s = -\frac{F}{\epsilon}\sum_i z_i C_i$. In the source, F is the Faraday constant, ϵ is the total carrier fluid permittivity, and z_i the ion valence. Knowing the potential distribution, the coupling terms $\boldsymbol{u}_{\mathrm{el},i}$ and $\boldsymbol{F}_{\mathrm{el}}$ can be determined as follows

$$\boldsymbol{u}_{\mathrm{el},i} = -D_i \frac{z_i e}{k_{\mathrm{B}} T} \boldsymbol{\nabla}\psi, \tag{5.1}$$

$$\boldsymbol{F}_{\mathrm{el}} = -(\boldsymbol{\nabla}\psi) F \sum_i z_i C_i. \tag{5.2}$$

The $k_{\mathrm{B}}T$ term is the product of the Boltzmann constant and temperature.

The total resulting system is called *reactive Navier-Stokes-Poisson-Nernst-Planck equation system (RNSPNPE)*.

5.1.1.2 Reaction system

In the present work, two parallel processes are considered as an example application: the dissolution of calcium cations from the pore surface (5.3), and the saturation of phosphate, hydrogen, and calcium ions, which enable the formation of OCP there (5.4). The reaction system can be written in ionic form as follows:

$$CSH + 1.66H^+ \leftrightarrows 0.83Ca^{2+}, \tag{5.3}$$

$$8Ca^{2+} + 6PO_4^{3-} + 2H^+ \xrightarrow{\textbf{saturation}} Ca_8H_2(PO_4)_6 \downarrow . \tag{5.4}$$

The stoichiometric dissolution coefficients are set according to [134]. More information about OCP and its further conversion to hydroxyapatite can be found in [135].

The common form for the crystallization and dissolution reaction rates used in this work is [27, 31]

$$r = \frac{k_{\mathrm{sr}}}{\triangle x}(\Omega - 1)^n. \tag{5.5}$$

Here, k_{sr} is the surface specific reaction rate constant $[\mathrm{mol\,m^{-3}\,s^{-1}}]$, the *saturation product* $\Omega = \left(\mathrm{IAP}/K_{\mathrm{sp}}\right)^{1/\sigma_{\mathrm{T}}}$ with ionic activity product $\mathrm{IAP} = \prod_i a_i^{\vartheta_i}$ and saturation point constant K_{sp}. n is the order of crystallization; in the case of dissolution, it is just one. The parameters k_{sr} and K_{sp} can be defined experimentally, by molecular dynamics simulation or special chemical software, like PHREEQC [136]. σ_{T} is the Temkin coefficient taken for the saturation product estimation. The ion activity a_i is calculated by the Debye-Hückel extended theory [137]:

$$a_i = \gamma_i C_i, \tag{5.6}$$

$$\log \gamma_i = -Az_i^2 \frac{\sqrt{I}}{1 + Ba_0\sqrt{I}}, \tag{5.7}$$

$$I = \frac{1}{2}\sum_i z_i^2 C_i. \tag{5.8}$$

The γ_i is the ion activity coefficient, which is computed with ionic strength I, smallest distance between interacting ions a_0, and case-specific constants A and B, which can be found in sum with all other used parameters in the Table 5.1.

5.1.2 Discretization

The given *RNSPNPE* system is discretized with LBM according to the Table 2.1 on the $D3Q19$ lattice (Figure 2.3c). Thereby in the *PE* scalar s is substituted by ψ. For the *RNPE*, sourced ADE is taken, where $s = C_i$, $\boldsymbol{u}_{\mathrm{ad}} = \boldsymbol{u}_{\mathrm{fl}} + \boldsymbol{u}_{\mathrm{el},i}$ and $Q_s = \sum_k R_{k,i}$. By NSE, $\boldsymbol{F} = \boldsymbol{F}_{\mathrm{el}}$ is set.

5.1.2.1 Algorithmic differentiation (AD) with operator overloading

The goal of the current work is to determine the influence of the model parameters and to understand which particle and which process settings lead to

Parameter	Value
Dielectric constant ϵ [$\mathrm{C\,V^{-1}\,m^{-1}}$]	$6.95 \cdot 10^{-10}$ [138]
Faraday constant F [$\mathrm{C\,mol^{-1}}$]	96485.33
Boltzmann constant k_B [$\mathrm{V\,C\,K^{-1}}$]	$1.38065 \cdot 10^{-23}$
Elementary charge e [C]	$1.602177 \cdot 10^{-19}$
Surface potential ψ_0 [V]	-0.01
Inlet velocity u_i [$\mathrm{m\,s^{-1}}$]	0.2
Fluid viscosity ν [$\mathrm{m^2\,s^{-1}}$]	10^{-6} [138]
Water mean free path λ_H2O [m]	$1.26 \cdot 10^{-10}$ [139]
Avogadro number N_A [$\mathrm{mol^{-1}}$]	$6.02 \cdot 10^{23}$
Hydrogen ion diffusion constant $D_{\mathrm{H^+}}$ [$\mathrm{m^2\,s^{-1}}$]	$9.31 \cdot 10^{-9}$ [140]
Phosphate ion diffusion constant $D_{\mathrm{PO_4^{3-}}}$ [$\mathrm{m^2\,s^{-1}}$]	$0.612 \cdot 10^{-9}$ [140]
Calcium ion diffusion constant $D_{\mathrm{Ca^{2+}}}$ [$\mathrm{m^2\,s^{-1}}$]	$0.792 \cdot 10^{-9}$ [140]
OCP saturation constant $K_{\mathrm{sp,OCP}}$ [$(\mathrm{mol\,m^{-3}})^{16}$]	$10^{-48.86}$ [141]
OCP Temkin coefficient $\sigma_{\mathrm{T,OCP}}$	1 [134]
CSH dissolution rate coefficient k_CSH [$\mathrm{mol\,m^{-2}\,s^{-1}}$]	$3.1 \cdot 10^{-11}$ [134]
CSH saturation constant $K_{\mathrm{sp,CSH}}$ [$(\mathrm{mol\,m^{-3}})^x$]	$10^{11.15}$ [134]
CSH Temkin coefficient $\sigma_{\mathrm{T,CSH}}$	16 [142]
Phosphor acid concentration $C_{\mathrm{H_3PO_4}}$ [$\mathrm{mol\,m^{-3}}$]	0.1
Temperature T [K]	298.15
Debye-Hückel coefficent A [$\sqrt{(\mathrm{m^3\,mol^{-1}})}$]	0.016102
Debye-Hückel coefficent B [$\sqrt{(\mathrm{m^3\,m^{-2}\,mol^{-1}})}$]	$1.0391 \cdot 10^{8}$
Molecular distance Ca-w [m]	$2.33 \cdot 10^{-10}$ [143]
Knudsen number Kn	0.09
Discretization parameters	
Cell size $\triangle x$ [m]	$1.40045 \cdot 10^{-9}$
Time step Poisson lattice $\triangle t_\mathrm{PE}$ [s]	$2.45159 \cdot 10^{-19}$
Time step momentum lattice $\triangle t_\mathrm{NSE}$ [s]	$2.61503 \cdot 10^{-13}$
Time step ions lattice $\triangle t_\mathrm{NPE}$ [s]	$4.80703 \cdot 10^{-11}$

Table 5.1.: Simulation parameters and constants.

the highest adsorption efficiency. Several approaches are available for the numerical computation of the *sensitivities* $\frac{ds}{db_d}$, $d = 1, \ldots, D$, of a quantity s with respect to design variables $b_1, ..., b_d$ (in this context called control variables). Here is a brief recapitulation of them. For a concise introduction, please look into [144].

- The least invasive method is the computation of *forward difference quotients*, where the derivative $\frac{ds}{db_d}$ is approximated as

$$\frac{ds}{db_d} \approx \frac{s(b + \mu|b_d|v_d) - s(b)}{\mu} \tag{5.9}$$

  for $d = 1, \ldots, D$, respectively. Here, v_d denotes the dth unit vector and μ is a small number. The optimal choice $\mu \approx \eta^{1/2}$, where η is the machine precision, yields a numerical error of size $\epsilon^{1/2}$. The scheme results is executing the primal simulation D times.

- Computation of *central difference quotients* is a more accurate, but also more expensive variant of the one described above. Here, the approximation is

$$\frac{ds}{db_d} \approx \frac{s(b + \mu|b_d|v_d) - s(b - \mu|b_d|v_d)}{2\mu} \tag{5.10}$$

  for $d = 1, \ldots, D$ with $\mu \approx \eta^{1/3}$, which results in $2D$ primal simulations and a numerical error of size $\eta^{2/3}$.

- *Forward algorithmic differentiation* (AD) treats each variable X as a vector $\left[X, \frac{\partial X}{\partial b_1}, ..., \frac{\partial X}{\partial b_d}\right] \in \mathbb{R}^{D+1}$, which contains the value as well as the sensitivities with respect to the control variables. For initialization, the sensitivity of a control parameter b_d with respect to another control $b_{d'}$, $d, d' = 1, \ldots, D$, is $\delta_{d,d'}$. The derivative components are then processed according to the derivation combination rules during all mathematical operations. E.g., the product Z of two variables X, Y is

$$\left[Z, \frac{\partial Z}{\partial b_1}, ..., \frac{\partial Z}{\partial b_d}\right] := \left[XY, X\frac{\partial Y}{\partial b_1} + Y\frac{\partial X}{\partial b_1}, ..., X\frac{\partial Y}{\partial b_d} + Y\frac{\partial X}{\partial b_d}\right].$$

  The whole program is executed similar to the standard program. At the end, one arrives to the quantity of interest s and its sensitivities $\frac{ds}{db_d}$, $d = 1, \ldots, D$. The computational costs grow proportionally to D and, in contrast to finite difference methods, optimal accuracy at

machine precision is observed. Similarly to the above methods, this method is generic and well-suited for time-dependent problems, coupled problems and nonstandard boundary conditions. Both numerical and computational performance of AD in the context of (LBM) fluid flow problems is evaluated in [116, 145–147].

- *Adjoint methods* solve the adjoint PDE system in order to compute the sensitivities $\frac{ds}{db_d}$ from the adjoint solution. Unlike the above approaches, solving one adjoint system allows to compute arbitrarily many sensitivities. Hence, the computational effort is independent from D. The approach is less generic, e.g., for different boundary conditions, a new adjoint system needs to be deduced. Moreover, since the adjoint system evolves backwards in time, complex and costly checkpointing methods have to be employed in order to treat time-dependent problems.

Keeping in mind the requirements of time dependence and accuracy (cf. Section 5.1.4.2), forward AD is employed in this work. To do so, it needs to be guaranteed that each single mathematical operation used in the program is differentiable (at least in a subdifferential sense). Implementation details are shown in the Appendix A.2.3.4.

5.1.2.2 Simulation algorithm for RNSPNPE with AD

In the following, the global time step with AD w.r.t. variable α is reported.

1: *// Lattice Boltzmann (LB) steps*
2: **while** $\frac{\frac{1}{N_t}\sum_l^{N_t}(\psi_{\mathrm{avg},l}-\sum_m^{N_t}\psi_{\mathrm{avg},m})^2}{\sum_m^{N_t}\psi_{\mathrm{avg},m}} > \varepsilon$ **do** ▷ Poisson loop
3: Collision and streaming for *PE* with vector $\left(f_{j,\mathrm{PE}}, \partial_\alpha f_{j,\mathrm{PE}}\right)$ ▷ Eq. (2.12)
4: **end while**
5: **for each** solved ion **do**
6: Collision and streaming for *RNPE* with vector $\left(f_{j,i,\mathrm{RNPE}}, \partial_\alpha f_{j,i,\mathrm{RNPE}}\right)$ ▷ Eq. (2.11)
7: **end for**
8: Collision and streaming for carrier fluid *NSE* with vector $\left(f_{j,\mathrm{NSE}}, \partial_\alpha f_{j,\mathrm{NSE}}\right)$ ▷ Eq. (2.8)
9: *// Post-processing*
10: Compute Poisson source term S_{PE} and its derivative $\partial_\alpha S_{\mathrm{PE}}$ ▷ Eq. (2.12)

for each solved ion **do**
    Compute electric velocity and its derivative w.r.t. α ▷ Eq. (5.1)
end for
Compute electric force for the carrier fluid and its derivative w.r.t. α ▷ Eq. (5.2)
for each boundary cell **do**
    Calculate r_{diss}, $\partial_\alpha r_{\text{diss}}$ ▷ Eq. (5.5)
    Calculate saturation product $\Omega = \left(\frac{\text{IAP}}{K_{\text{sp}}}\right)^{\frac{1}{\sigma_{\text{T}}}}$ and $\partial_\alpha \Omega$ for OCP
end for

5.1.3 Validation and analysis of the LBM model

Due to the complexity of the described model, its parts are validated separately against analytical solutions. All the test cases are one-dimensional, but they are solved on three-dimensional lattices with periodic boundaries in the other directions. All the examples are computed until convergence of the spatially averaged electric potential is achieved based on the following criterion:

$$\frac{\frac{1}{N_t}\sum_l^{N_t}(\psi_{\text{avg},l} - \sum_m^{N_t}\psi_{\text{avg},m})^2}{\sum_m^{N_t}\psi_{\text{avg},m}} < 10^{-9}, \tag{5.11}$$

where N_t is the number of time steps at which the convergence of *PE* was checked. All the cases are steady-state without time dependence, so that there is no need for an internal *PE* simulation loop. All the discretized equations are calculated once per time step.

5.1.3.1 Poisson equation

Description of the used here application code is given in the Section A.2.3.1.

The *PE* for validation test, which is taken from [78], is defined as

$$\Delta\psi = h^2\psi, \tag{5.12}$$

with according boundaries

$$\psi_{x=0} = \psi_{x=1} = 1, \tag{5.13}$$

$$h = 27.79, \tag{5.14}$$

and analytical solution

$$\psi(x) = \frac{e^h - 1}{e^h - e^{-h}} e^{-hx} + \frac{1 - e^{-h}}{e^h - e^{-h}} e^{hx}. \tag{5.15}$$

The convergence behavior of the discretized *PE* is shown in Figure 5.2. Three different relative error norms ($L^1, L^2, L^\infty - Eq.\ 2.73, 2.74, 2.75$) between the analytical ψ_a and numerical solutions ψ_n of the equation 5.12 are shown.

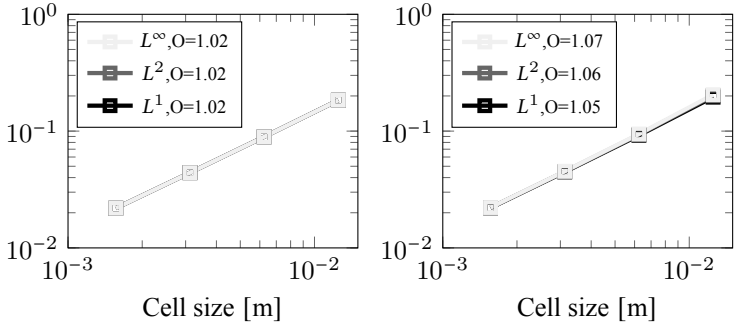

(a) $\tau = 1$ (b) $\tau = 0.6$

Figure 5.2.: Errors plot of the discretized Poisson equation.

It can be seen that the lines have a *slope of approximately one*, independent of the chosen relaxation time τ. According to these results, the simulation ansatz is considered as *convergent*.

5.1.3.2 Poisson-Nernst-Planck equation system

Description of the used here application code is given in the Section A.2.3.2.

The ideal case for the *PNPE* system is the analytically solvable Poisson-Boltzmann equation, which describes the Gouy-Chapman model for ionic

solutions close to a charged surface [130]. The *PNPE* system can be written for monovalent cations and anions as:

$$\Delta\psi + \frac{F}{\epsilon}(C_+ - C_-) = 0, \tag{5.16}$$

$$\partial_t C_+ - \left(\frac{De}{k_\mathrm{B}T}\nabla\psi\right)\nabla C_+ = D\Delta C_+, \tag{5.17}$$

$$\partial_t C_- + \left(\frac{De}{k_\mathrm{B}T}\nabla\psi\right)\nabla C_- = D\Delta C_-, \tag{5.18}$$

whereas the boundary conditions are described as:

$$\psi_{x=0} = -0.02V, \qquad \psi_{x=L} = 0V, \tag{5.19}$$

$$\nabla C_{\pm,x=0} = 0\ (bounce - back), \qquad C_{\pm,x=L} = 0.01\mathrm{mol\,m^{-3}}. \tag{5.20}$$

The diffusion constant D is set to $10^{-8}\ \mathrm{m^2\,s^{-1}}$, temperature T to 298 K, dielectric constant ϵ to $6.95\cdot10^{-10}\ \mathrm{C\,V^{-1}\,m^{-1}}$. The Faraday constant F is $9.649\cdot10^4\ \mathrm{C\,mol^{-1}}$, the elementary charge e equals $1.602\cdot10^{-19}$ C. The computation domain length L is set to 13 *Debye lengths* λ_D, which is

$$\lambda_\mathrm{D} = \sqrt{\frac{\epsilon k_\mathrm{B}T}{2e^2 C_{x=L} N_\mathrm{A}}}. \tag{5.21}$$

This characteristic length represents the distance at which the electric potential ψ falls by $\frac{1}{e}$. The Avogadro number N_A is defined as $6.02\cdot10^{23}\ 1/\mathrm{mol}$. The λ_D and L for this simulation are 2.98 and 35.8 $\mu\mathrm{m}$ respectively.

The analytical solution for this setup is the solution for the Poisson-Boltzmann equation [130]:

$$\psi(x) = \psi_{x=0}\exp\left(-\frac{x}{\lambda_\mathrm{D}}\right), \tag{5.22}$$

$$C_\pm(x) = C_{\pm,x=L}\exp\left(\mp\frac{e\psi(x)}{k_\mathrm{B}T}\right). \tag{5.23}$$

A comparison of the analytical solutions above with the simulation results is shown in Figure 5.3. This plot shows a perfect agreement of simulated and analytical solutions of both counter-ions concentrations and the potential along the surface normal. The convergence orders of error norms can be found in the Figure 5.4, demonstrating approximately *first order convergence* of the system.

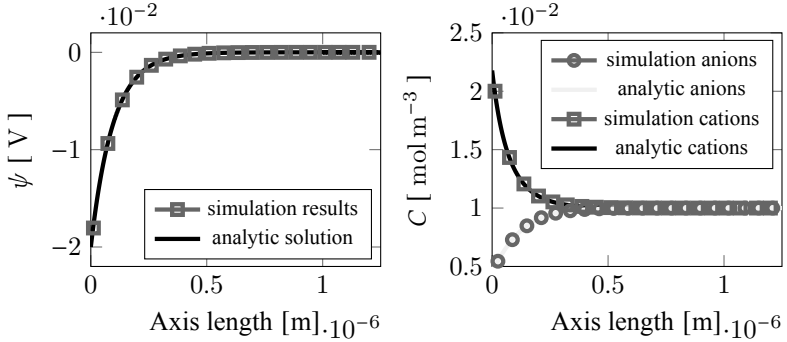

(a) Potential along the axis (b) Concentrations along the axis

Figure 5.3.: PNPE variable profiles.

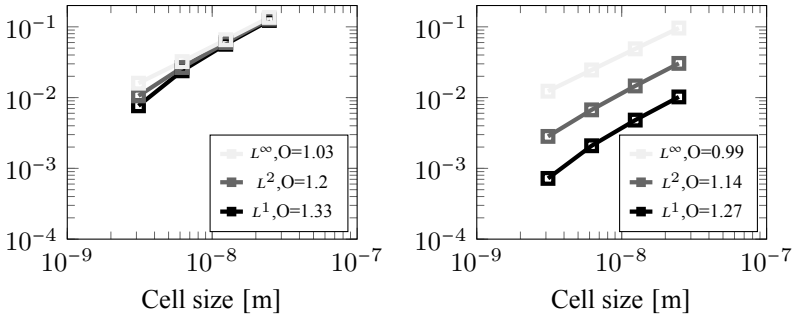

(a) Potential ψ convergence (b) Cation concentration C_+ relative errors plot

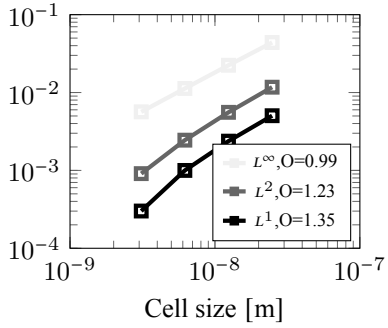

(c) Anion concentration C_- relative errors plot

Figure 5.4.: Relative errors plot of the *PNPE* system.

5.1.3.3 Navier-Stokes-Poisson-Nernst-Planck equation system

Description of the used here application code is given in the Section A.2.3.3.

The full elektro-dynamic system for two monovalent counter-ions is the same as in the previous example, with the addition of equations (2.7) and (2.8). The reference solution is also the Poisson-Boltzmann equation. The electric force present in the momentum equation is much smaller than the advection term in the Nernst-Planck equations, and therefore the influence of the carrier fluid without an external electric field in the Gouy-Chapman model is assumed to be negligible. The convergence order in the system remains the same as above.

To check the convergence behavior of the complete *NSPNPE* system, the steady-state one-dimensional electro-osmotic flow is reproduced:

$$\Delta\psi + \frac{F}{\epsilon}(C_+ - C_-) = 0, \tag{5.24}$$

$$\partial_t C_+ - \left(\frac{De}{k_\mathrm{B}T}\boldsymbol{\nabla}\psi\right)\boldsymbol{\nabla}C_+ = D\Delta C_+, \tag{5.25}$$

$$\partial_t C_- + \left(\frac{De}{k_\mathrm{B}T}\boldsymbol{\nabla}\psi\right)\boldsymbol{\nabla}C_- = D\Delta C_-, \tag{5.26}$$

$$\partial_t u_y + u_x\partial_y u_y + u_y\partial_x u_y + \frac{1}{\rho}\partial_y p = \nu(\partial_x^2 u_y + \partial_y^2 u_y) + \frac{F_{\mathrm{el},y}}{\rho}. \tag{5.27}$$

The boundary conditions are similar to the previous case (Eq. 5.19, 5.20). For the carrier fluid, the velocity on the wall is set to a bounce-back condition, whereby in the bulk it is set as zero-gradient. Instead of the internal electric field based on the potential gradients, a constant external field is applied in the y-direction, parallel to the wall. The only force acting within the system is also directed towards the y direction:

$$F_{\mathrm{el},y} = E_y F \sum_i z_i C_i. \tag{5.28}$$

In the current case $E_y = 250\ \mathrm{V\,m^{-1}}$. The analytical solution for carrier fluid velocity in the normal-to-wall direction is

$$u_y(x) = -\frac{\epsilon\psi_{x=0}E_y}{\nu\rho}\left(1 - \frac{e^{\frac{x}{\lambda_\mathrm{D}}} + e^{\frac{2L-x}{\lambda_\mathrm{D}}}}{1 + e^{\frac{2L}{\lambda_\mathrm{D}}}}\right). \tag{5.29}$$

The convergence plot of the velocity error norms is shown below (Figure 5.5).

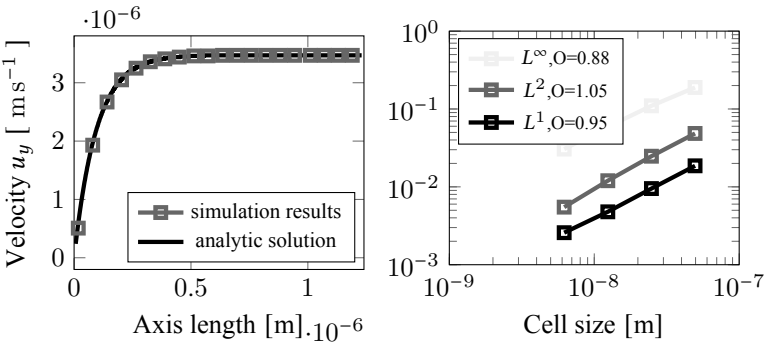

(a) *NSPNPE* velocity validation

(b) Relative errors plot of the discretized *NSPNPE* system

Figure 5.5.: *NSPNPE* model validation.

The velocity shows a convergent behavior as well, and therefore the full *NSPNPE* system can now be held as validated. All the system components and all variables show *first-order convergence*, and therefore the full system is considered a consistent model for a saturation electro-dynamic simulation. Such an order of convergence is caused by the boundary conditions, which reduce the second-order convergence of the BGK collision down to the first order. In future works, the boundary conditions will be enhanced in order to achieve a global second-order convergence.

5.1.4 Sensitivity assessing algorithm test

Validation of the AD sensitivity calculation on FDM results is performed using the two-dimensional simulation domain shown in Figure 5.8 a). The simulation setup description is given in Section 5.2.1.1.

5.1.4.1 Necessity of internal Poisson equation loop

To improve simulation efficiency, only one *PE* step per global time step is performed instead of iterating through the entire loop. This is permissible

because changes in local ion concentrations during a single global time step are minimal. The *PE* quickly adapts to new ion configurations in response to changes of the source term, due to its short reaction time. This immediate adaptation is demonstrated in Figure 5.6, which compares the averaged saturation products calculated with and without the full Poisson convergence loop.

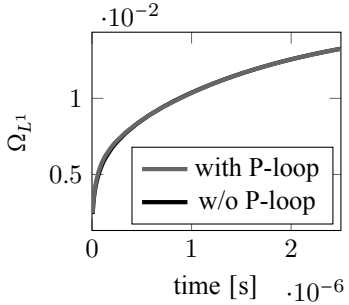

Figure 5.6.: Saturation product Ω_{OCP} with and without *PE* full convergence per global time step.

5.1.4.2 Validation of AD with FDM applied to phosphate saturation

Figure 5.7 shows a comparison of the spatially averaged saturation product sensitivity to the carrier fluid inlet velocity u_{in} calculated using both central FDM with a step size of 10^{-6} and the AD algorithm. The values associated with the FD analysis have been computed in the following way:

$$\left(\partial_{u_{\text{in}}} \Omega\right)_{L^1}(t) = \frac{\Omega_{L^1}\left(t, u_{\text{in}} + 10^{-6} \cdot u_{\text{in}}\right) - \Omega_{L^1}\left(t, u_{\text{in}} - 10^{-6} \cdot u_{\text{in}}\right)}{2 \cdot 10^{-6} \cdot u_{\text{in}}}. \quad (5.30)$$

Both the curves presented in Figure 5.7 have similar behavior and overlapping values, and therefore, the *AD algorithm is validated*. These curves indicate a negative falling sensitivity of the average saturation product with respect to the inlet carrier fluid velocity. Firstly, this means that the system has not yet reached a steady state within the observed time frame. Secondly, the negative sensitivity highlights the need to reduce the inlet velocity to achieve a higher saturation product. In the case of an open-pores setup, this can be explained by the fact that higher fluid velocities cause ions to be swept away, preventing

their accumulation at a single point, which is essential for maximizing the saturation probability. More details can be found in the next Section 5.2.

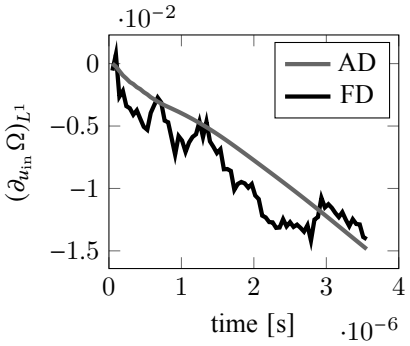

Figure 5.7.: Sensitivity of the saturation product with respect to the inlet velocity calculated using FD and AD.

5.2 Analysis of phosphate saturation in nanopores

Description of the used here application code is given in the Section A.2.3.5.

The present Section uses the integrated hydro-electro-chemo-dynamics sensitivity assessing solver presented in the previous Section, to perform comprehensive simulations of the phosphate crystallization reaction—more specifically, to the OCP saturation. The developed algorithm described in the previous Section is applied to perform the first-ever integrated simulations of phosphate saturation, complemented by a sensitivity analysis to identify key influencing factors like pore dimensions and impact of pore shape types, carrier fluid velocity, Helmholtz potential, and reacting ion concentrations.

This Section is structured as follows. First, 2D simulations of simplified models are performed (Section 5.2.1). A two-dimensional parameterized simplified simulation domain, which represents a resolved nano-porous system, is analyzed with the AD-based sensitivity assessment solver (Section 5.2.1.2). The following influence factors are investigated: surface electric potential, pore

dimensions, bulk concentrations and carrier fluid inlet velocity. Two geometries, respectively representing blind and open pores, are used (Section 5.2.1.3). Then, the same approach is applied to investigate a realistic three-dimensional porous system (Section 5.2.2). Special attention is paid to the electric surface potential, as it allows to differentiate between pore types, and to the size of the simulated geometry. The results of the 3D analysis are tested by varying the simulation setup parameters in Section 5.2.2.5.

5.2.1 2D simulations

Each micro-particle has contact with the bulk on both outer and inner surfaces, necessitating the consideration of both in this research. According to IUPAC [148], the inner surfaces or inter-particle pores can be categorized into *closed*, *blind*, and *open pores*, each with distinct geometrical shapes. Closed pores, being inaccessible to dissolved ions from outside, are excluded from the simulations. Open and the blind pores will be investigated separately, focusing on the following parameters: surface Helmholtz potential, pore dimensions, ion concentrations, and carrier fluid inlet velocity.

In this Section, the geometry of single particles—each featuring either *open* or *blind pores*—in a simplified 2D setup is resolved.

5.2.1.1 Simulation setup and boundary conditions for 2D geometries

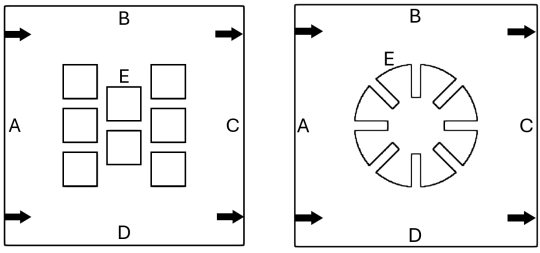

(a) Open pores (b) Blind pores

Figure 5.8.: Simulation domains. Open pores – 42.8 nm wide, 84 nm length-per-block. Blind pores – 42.8 nm wide, 123.5 nm deep.

In the current research, ion accumulation at nano-scale on solid walls in porous micro-systems is investigated. For the two-dimensional investigations, two square domains with arbitrarily designed schematic porous geometries are created (Figure 5.8). The geometry **(a)** represents **open pore** test case, whereby the option *(b)* is designed for *blind pores* investigation. The two options are simulated with coupled sensitivity analysis, starting by nano-pores diameter of 42.8 nm. The distance between the outer solid bodies and the domain boundaries is set to 12 Debye lengths computed for 0.1 $\mathrm{mol\,m^{-3}}$ of phosphate anion. Such distance is chosen in order to make sure that the electric potential at the domain boundaries remains negligible. At the small simulation scales, the cell size has influence on the physical computation model. At higher Knudsen numbers [139], the additional Knudsen diffusion and some other effects should be considered, which would complicate the existing model much more and are not included into current research. Here, d_{m} is the molecule diameter, and M is the molar mass of water, which is the specie with the highest concentration. Water is also the carrier fluid, and has the largest mean free path among all considered components (Table 5.1) in the solution and its concentration is incomparably higher than the other ones. The cell size $\triangle x$ is set to $0.09 \cdot \mathrm{Kn}$. The solid body corner length is set to 60 cells.

The domain boundaries **A**, **B**, **C**, and **D** are treated identically, with the electric potential set to zero. The carrier fluid is assigned a constant flow velocity in the positive x-direction (**A**, **B**, **C**, **D**), and these outer boundaries are handled uniformly to avoid any influence from differing boundary conditions and to prevent instabilities. Hydrogen and phosphate ions are each given fixed concentrations of 0.3 and 0.1 $\mathrm{mol\,m^{-3}}$, respectively, while their concentrations inside the domain are initialized to zero to capture the diffusion of ions from the bulk to the pore openings and into the pores. The concentration of calcium cations, on the other hand, is set to zero at the boundaries to avoid undesirable backflow of these ions and improve boundary stability.

At the Helmholtz layer next to the solid surface (boundary **E**), the electric potential is set to a constant value of ± 0.01 V. Its impact is investigated in the current work as well. The transported ions are reflected at the solid walls, whereby in the bulk cells touching the boundaries their concentration can be changed according to the corresponding reaction term $\sum_k R_{k,i}$. In LBM this corresponds to the bounce-back boundary condition together with a source term applied in the boundary cells. At the Knudsen number of 0.09 the slip regime for the carrier fluid velocity is considered [123].

The full list of used setup parameters and constants is shown in Table 5.1.

5.2.1.2 Investigation of saturation on the 2D porous object

Given the significant uncertainty surrounding the Helmholtz electric potential at solid surfaces, two scenarios are considered, with potentials being set at -0.01 and +0.01 V. Then, the sensitivities of the corresponding parameters are investigated. The variables for which derivatives are calculated include carrier fluid inlet velocity, pore width, initial concentrations of hydrogen and phosphate ions, and electric potential at the block's solid surface (boundary **E**).

The primary evaluation criterion for crystal formation is the *saturation product* Ω. If it is larger than one, nucleation and crystallization on the surface are enabled. Of particular interest is the temporal development of the spatially averaged and maximal saturation products, along with their partial derivatives. The spatially averaged values are computed as follows:

$$\Omega_{L^1}(t) = \frac{1}{N_{\text{node}}} \sum_{x_i=1,\Omega(x_i)>0}^{N_{\text{node}}} \Omega(x_i, t), \tag{5.31}$$

$$(\partial_\phi \Omega)_{L^1}(t) = \frac{1}{N_{\text{node}}} \sum_{x_i=1,\Omega(x_i)>0}^{N_{\text{node}}} \partial_\phi \Omega(x_i, t), \tag{5.32}$$

where ϕ represents the variable with respect to which the derivative is taken.

Figures 5.9 and 5.10 illustrate the saturation products and their sensitivities for different Helmholtz potentials across geometries **(a)** and **(b)**. The left column presents the spatially averaged values, while the right column shows the behavior of the maximal values.

Saturation product development

Averaged and maximal saturation product development are shown in Figures 5.9a and 5.9b. The development of the saturation product varies significantly between geometries **(a)** and **(b)**. Despite their shallower depth (for the same width), blind pores exhibit significantly higher saturation levels, which do not reach equilibrium within the investigated time frame. Conversely, in the case of open pores, the Helmholtz surface potential has no significant impact on the

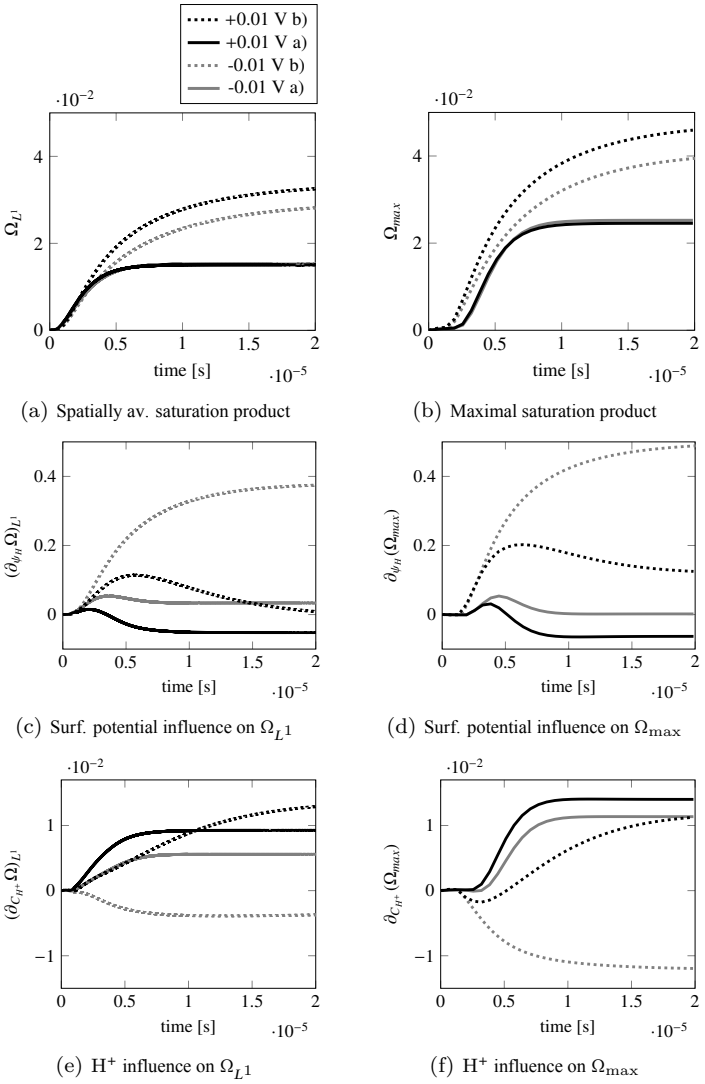

(a) Spatially av. saturation product

(b) Maximal saturation product

(c) Surf. potential influence on Ω_{L1}

(d) Surf. potential influence on $\Omega_{\max}$

(e) H^+ influence on Ω_{L1}

(f) H^+ influence on $\Omega_{\max}$

Figure 5.9.: Maximal and spatially averaged developments of saturation product Ω and its derivatives with respect to surface potential ψ_{H}, hydrogen and phosphate concentrations H^+, PO_4^{3-}, pore width and inlet carrier fluid velocity u_{in} on the a) and b) geometries by opposite Helmholtz potentials of ±0.01 V. Part I/II.

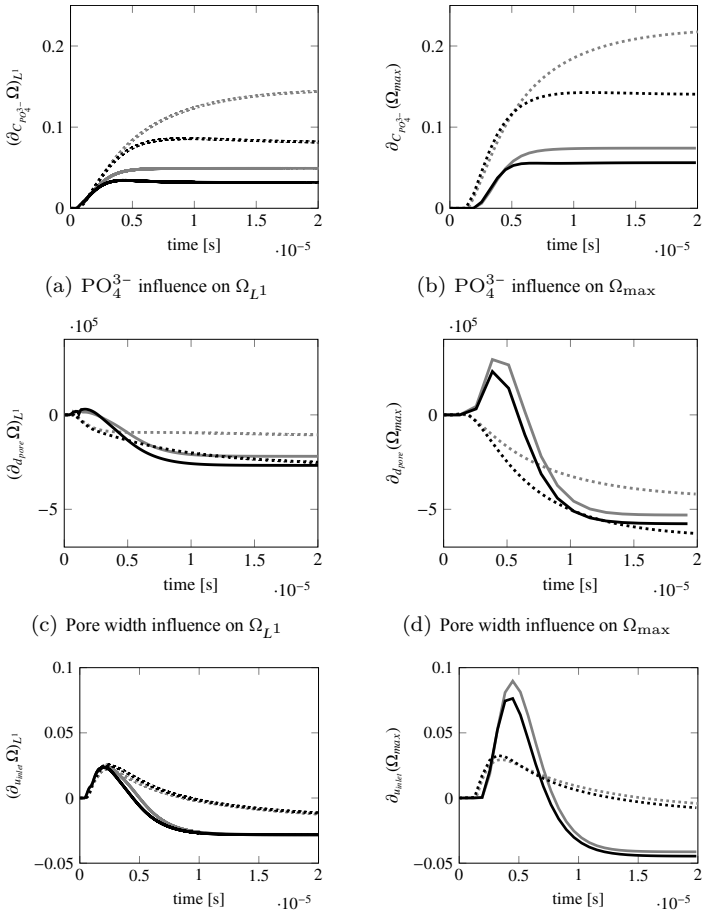

(a) PO_4^{3-} influence on Ω_{L1}

(b) PO_4^{3-} influence on $\Omega_{\max}$

(c) Pore width influence on Ω_{L1}

(d) Pore width influence on $\Omega_{\max}$

(e) Inlet velocity influence on Ω_{L1}

(f) Inlet velocity influence on $\Omega_{\max}$

Figure 5.10.: Maximal and spatially averaged developments of saturation product Ω and its derivatives with respect to surface potential ψ_{H}, hydrogen and phosphate concentrations H^+, PO_4^{3-}, pore width and inlet carrier fluid velocity u_{in} on the a) and b) geometries by opposite Helmholtz potentials of ±0.01 V. Part II/II.

saturation product value. However, in blind pores with a positive potential, the saturation of OCP is significantly enhanced.

Figure 5.11 displays the spatial distribution of the saturation product at time t=20 μs. It is evident that saturation within the pores is much higher than on the outer particle surface. The maximal values of the saturation product are located closer to the center of the geometry in the case of open pores and at the ends of blind pores. Consequently, further investigation focuses on the behavior of saturation within the pores.

To conclude, saturation within the pores is significantly higher for both Helmholtz potentials compared to the outer particle surfaces, especially high it is in the blind pore dead-ends.

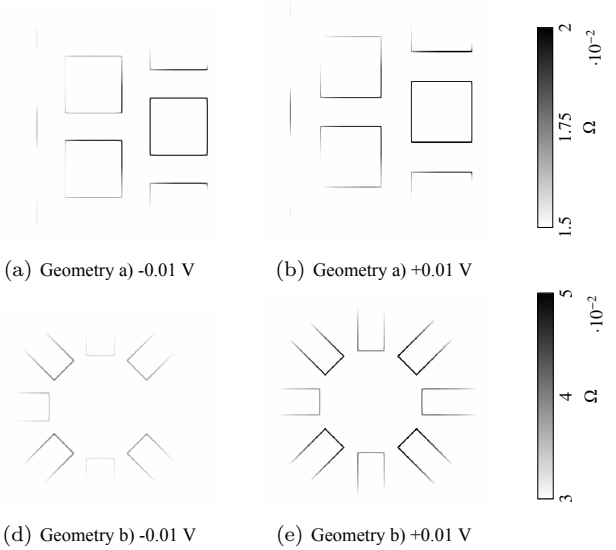

Figure 5.11.: Saturation product spatial distribution by geometries a) and b) by negative and positive Helmholtz potentials at the simulation final (20 μs).

Helmholtz potential influence

Figures 5.9c and 5.9d show the influence of the surface electric potential of solid blocks on the saturation product development. For open pores, the sensitivities

indicate that to increase the average saturation product, the Helmholtz surface potential should be set closer to zero. However, the maximal saturation value is achieved at a slightly negative potential (cfr. Figure 5.9b). In contrast, for blind pores, a different behavior is observed. To maximize the average saturation product, the potential should be slightly positive, as can be observed in further simulations with 0.02 V and 0.2 V as surface potential values. Moreover, increasing the positive potential value at the point of maximum saturation within the pore enhances the probability of oversaturation.

In synthesis, a positive Helmholtz surface potential enhances saturation at the point inside a pore where the saturation product reaches its maximum.

Hydrogen cations concentration influence

The averaged and maximal sensitivities with respect to hydrogen ion concentration are shown in Figures 5.9e and 5.9f. In open pores, ion accumulation increases with rising hydrogen concentration for both negative and positive surface potentials. However, a positive potential leads to a higher derivative with respect to the hydrogen ion concentration. This phenomenon can be explained by the fact that cations are repelled from the surface, which is counterbalanced by diffusive transport. Higher concentrations enhance the diffusive transport of ions. In blind pores with a positive surface potential, the sensitivity to hydrogen concentration is consistently positive. Conversely, with a negative potential, the sensitivity is always negative, indicating that hydrogen is attracted to the surface by the electric force, and this force is sufficient to achieve OCP oversaturation even at lower concentrations.

Thus, because a positive surface potential is preferable based on the observations in the previous section, it is recommended to increase hydrogen concentration whenever feasible.

Phosphate anions concentration influence

Figures 5.10a and 5.10b illustrate the impact of phosphate anions concentration. In all cases, an increase in phosphate concentration consistently promotes a rise in the saturation product. As illustrated above, the sign of the surface potential influences the sensitivity. For anions, diffusive transport must overcome

the resistance of electric force in the case of a negative Helmholtz potential, resulting in higher sensitivity.

As such, it is recommended to increase the phosphate concentration whenever feasible, irrespective of the value of the surface potential.

Pore dimensions influence

The pore dimensions deliver the highest impact on the saturation product. In the 2D case, the parameters considered for sensitivity analysis are pore width and length.

Pore width.

Figures 5.10c and 5.10d illustrate the influence of pore width over the saturation product. In all the considered scenarios, pore width consistently shows negative sensitivity towards the end of the simulation. Initially, the derivative curves increase until the maximum possible volume filling of hydrogen and phosphate ions is achieved. The maxima are significantly smaller for blind pores compared to open ones due to geometric differences. In geometry **(a)**, the total length of open pores is greater than the combined length of the blind ones, requiring more time to fill the open pores with ions from the bulk. This time can be determined from the plot by reading the time where the curves cut the x-axis. After reaching the sensitivity maxima, the curves decline to relatively constant negative values because narrow pores restrict the outflow of dissolved calcium cations.

Therefore, minimizing pore width is recommended. Although this slows ion transport from the bulk, it leads to a higher saturation product.

Pore length.

Figure 5.12 shows the saturation product derivative with respect to pore length, calculated for geometry **(b)** with a positive Helmholtz potential, as this setup yields the highest saturation among those tested. Initially, while the pores have not yet reached the maximum possible concentration of incoming ions, the derivative is negative. After this point, the derivative starts to increase

and becomes positive, resulting in a higher maximum achieved saturation product.

Concluding, pores should be deeper to accumulate more reacting ions inside them.

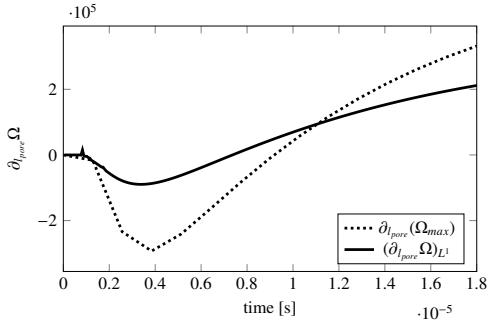

Figure 5.12.: Development of the average and maximal saturation product sensitivity with respect to pore depth by geometry b) and positive Helmholtz potential.

Influence of the inlet velocity

The sensitivity analysis with respect to inlet velocity is shown in Figures 5.10e and 5.10f. Depending on the pore type and its specific arrangement within the geometry, the carrier fluid velocity can influence saturation behavior in various ways.

Open pores

The impact of carrier fluid inlet velocity is more pronounced in open pores compared to blind pores. An analysis of the maximum of the derivative graph provides insight into the time required to fill the pore volume with reacting ions, similarly to the case of the influence of pore size. The carrier fluid, moving at a velocity determined by the choice of the boundary conditions, reduces the accumulation of dissolved calcium ions in the boundary cells from a certain moment onwards. At the beginning, the carrier fluid fills the pore volume with ions, which is why the sensitivity is positive, but after that it sweeps the ions

away and hinders the rise of saturation product. This negative effect is more pronounced in open pores, where the fluid can pass through the entire geometry with less resistance. Figure 5.13 illustrates the distribution of calcium cations in open pores for setups with 0.2 $\mathrm{m\,s^{-1}}$ inlet velocity and without. It is clear

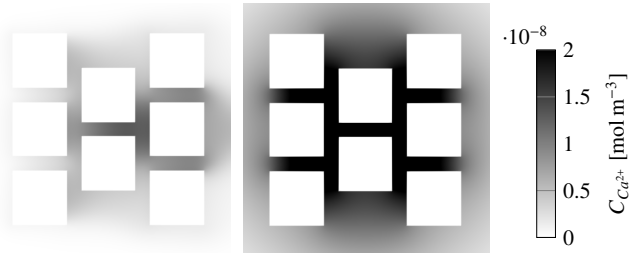

(a) With inlet velocity (b) W/o inlet velocity

Figure 5.13.: Accumulation of the calcium cation concentration at 13.46 µs with and without carrier fluid inlet velocity.

that the absence of the carrier fluid movement promotes the accumulation of the ions and the increase of the saturation product.

Blind pores

For the blind pores (geometry **b**), the sensitivities and saturation product among the pore-end centers on the right, upper, left, and bottom sides are compared, as illustrated in Figure 5.14. A dead zone forms leeward of the geometry, allowing phosphate ions to accumulate and leading to the highest saturation product at point C. Towards the end of the simulation, all derivatives with respect to the velocity tend towards negative values or zero. At point C, the influence of surface potential also turns negative, unlike in other pores. The reduction of the size of the dead zone in geometries with deeper and narrower pores can be attributed to spatial interactions among ions in the dead zone. Calcium and hydrogen ions are compelled to exit the pore, leading to a lower saturation product at point C. The development of the saturation product and spatial ion distribution at the end of the simulation is depicted in Figure 5.15. The calcium spatial distribution plays the largest part in determining the spatial distribution of the saturation product despite its very low concentration compared to hydrogen and phosphate; indeed, the cell with maximal calcium concentration is at the same time the cell with the highest saturation product. Therefore, to achieve

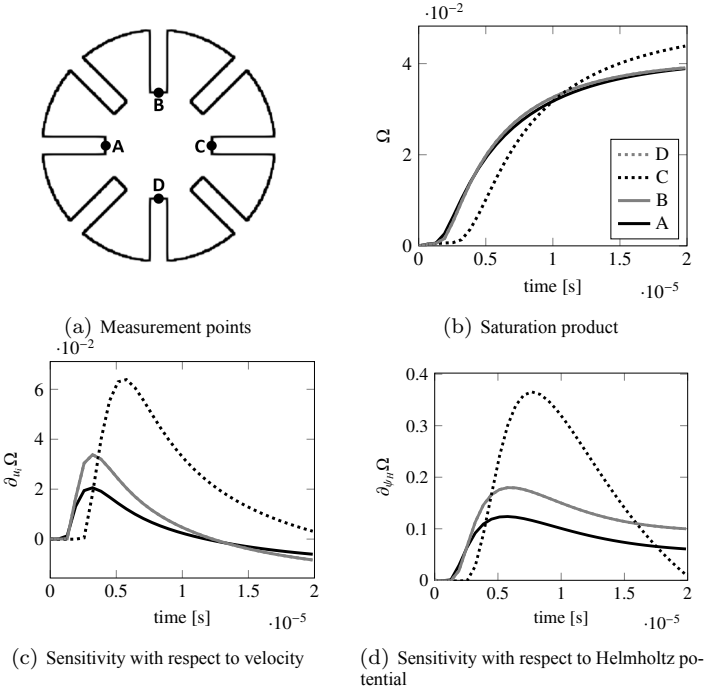

(a) Measurement points

(b) Saturation product

(c) Sensitivity with respect to velocity

(d) Sensitivity with respect to Helmholtz potential

Figure 5.14.: Velocity influence on the saturation product and its sensitivities at the ends of blind pores by geometry b).

oversaturation, conditions should be optimized for maximal accumulation of calcium in the pores.

It can be deduced that a high inlet carrier fluid velocity accelerates the filling of pores with reactants, but at the same time, reduces the overall saturation product in the entire domain for open pores. In blind pores, the carrier fluid can redistribute ions such that saturation may increase in shallower pores while decreasing in others.

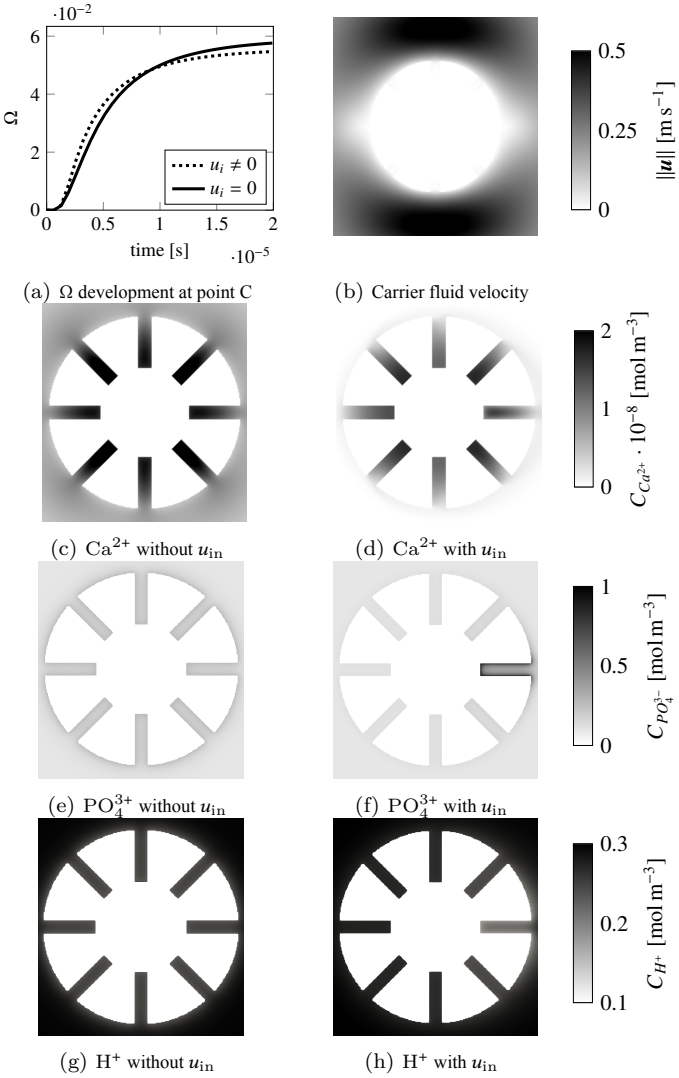

(a) Ω development at point C

(b) Carrier fluid velocity

(c) Ca^{2+} without u_{in}

(d) Ca^{2+} with u_{in}

(e) PO_4^{3+} without u_{in}

(f) PO_4^{3+} with u_{in}

(g) H^+ without u_{in}

(h) H^+ with u_{in}

Figure 5.15.: Comparison of the saturation product behavior and ions concentrations at the calculation end by simulations with and without carrier fluid velocity. Velocity direction is from left to right.

5.2.1.3 Validation of 2D analysis results on modified geometries

In order to test the generality of the observations traced above, two parameterized simulations—with one *open* (**a**) and one *blind pore* (**b**)—are performed (Figure 5.16). These geometries are created so that the outer particle dimensions are the same as in the previous geometries, but there is only one long open or blind pore. The parameters are varied according to the sensitivities in Table 5.2.

Setup	I	II
d_{pore} [nm]	42.8	10.7
ψ_{H} [V]	+0.01	+0.01
$C(\mathrm{H}^{+})$ [mol m^{-3}]	0.3	6
$C(\mathrm{PO}_4^{3+})$ [mol m^{-3}]	0.1	1
u_{in} [m s^{-1}]	0.2	0

Table 5.2.: Parameter optimization.

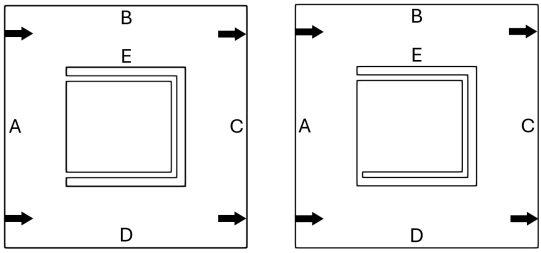

(a) Open pores - II (b) Blind pores - II

Figure 5.16.: Simulation domains.

The temporal development of average and maximal saturation products is shown in the Figure 5.17. The modified boundary parameters and pore shapes in the modified 2D geometries lead to a much higher saturation. The maximal saturation product observed in the blind pore surpasses the value of 1 after 550 µs and induces nucleation and crystallization in that lattice cell. The saturation in the open pore reaches a steady state twice as fast as in the blind-

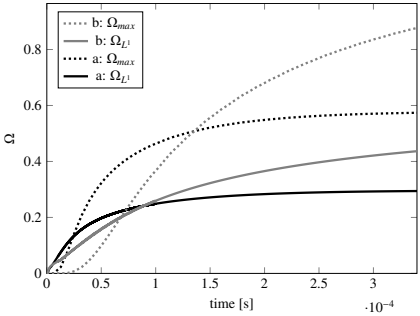

Figure 5.17.: Average and maximal saturation product development by modified pore geometries (a – open pore, b – blind pore).

pore case due to the presence of two inlets that allow hydrogen and phosphate to diffuse in while calcium ions diffuse out.

Figure 5.18 depicts the saturation product and ion concentration distributions at the end of the simulation. In the open pore, the maximum saturation product is observed at the center, equidistant from both ends. In contrast, in the blind pore, the maximum occurs at the blind end. To understand these distributions, the individual ion concentrations must be considered. By the end of the simulation, the hydrogen cation concentration is uniformly distributed throughout the computational domain due to its relatively high diffusion coefficient, which overcomes the influence of the electric force. In contrast, phosphate anions are attracted to the solid surface, resulting in higher concentrations at the boundary cells compared to the bulk. The main difference between the two considered geometries lies in the distribution of calcium ion concentration. In an open pore, calcium ions flow out and accumulate only at the pore center, where the total transport velocity $\boldsymbol{u}_{\mathrm{t},i} = \boldsymbol{u}_{\mathrm{fl}} + \boldsymbol{u}_{\mathrm{el},i} - D_i \frac{\boldsymbol{\nabla} C_i}{C_i}$ approaches zero. In a blind pore, the transport path is approximately twice as long, and the calcium velocity remains low over a greater distance. Since the outlet direction is singular, the calcium removal rate is halved, allowing for more efficient ion accumulation. The total velocity at the end of the simulation is visualized in Figure 5.19.

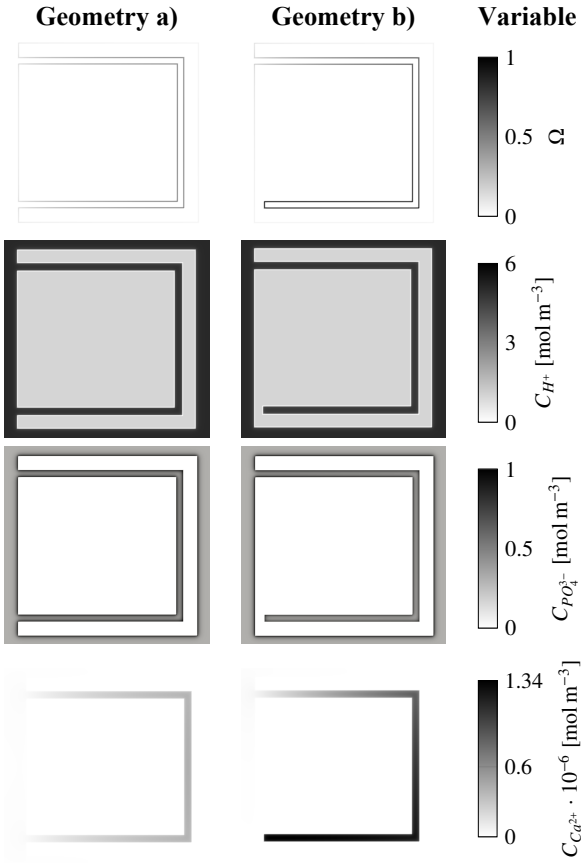

Figure 5.18.: Spatial distribution of saturation product Ω and ion concentrations of H^+, PO_4^{3+}, Ca^{2+} for geometries a) and b) at simulation final (345 µs).

The step-wise parameter optimization of geometries a) and b) is provided in the supplementary materials. The applied changes lead to oversaturation in the blind pore and the onset of crystallization, confirming the conclusions of the sensitivity analysis.

It can also be stated that there is a minimal surface-area-to-volume ratio (in 2D, perimeter-to-area) needed in order to reach an oversaturated solution state after which precipitation or crystallization can occur. Also, oversaturation

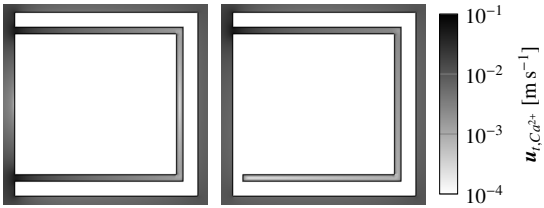

(a) Open pore a) (b) Blind pore b)

Figure 5.19.: Calcium cation total velocity distribution ($\boldsymbol{u}_{\mathrm{t},i} = \boldsymbol{u}_{\mathrm{fl}} + \boldsymbol{u}_{\mathrm{el},i} - D_i \frac{\nabla C_i}{C_i}$) at the simulation final (345 µs).

probability grows with this ratio. Increasing the Helmholtz potential can increase this ratio to some degree. Considering the phosphate binding to CSH, the probability of achieving oversaturation and following crystallization grows with the pH factor. In contrast, an increase in the carrier fluid velocity hinders the accumulation of calcium cations at the boundary cells above a certain threshold, and for this reason, increasing this value is not advisable.

5.2.2 Investigation of saturation on a realistic 3D geometry

Due to the lack of available CT scan data for CSH microparticles, the Estaillades carbonate CT scan [149] – freely accessible via the rock database (https://digitalporousmedia.org/) – was used as a representative example of a porous rock downscaled to a microparticle size to investigate the saturation behavior of a real three-dimensional porous micro-system. This setup maintains the same cell size and Knudsen number as the 2D simulation. A quarter of the microstructure file ($\alpha_{\mathrm{geom}} = \frac{V_{\mathrm{sim}}}{V_{\mu\mathrm{CT}}} = 25\%$), with a length of 180 nanometers and resolved with 114 cells, is surrounded by 50 pure fluid cells on each side. The same boundary conditions as the previous 2D setup are applied. The new boundary planes which have not existed in the 2D case are treated in the same way as the boundaries **A,B,C,D**. The geometry and pore size distribution of the system are shown in Figure 5.20.

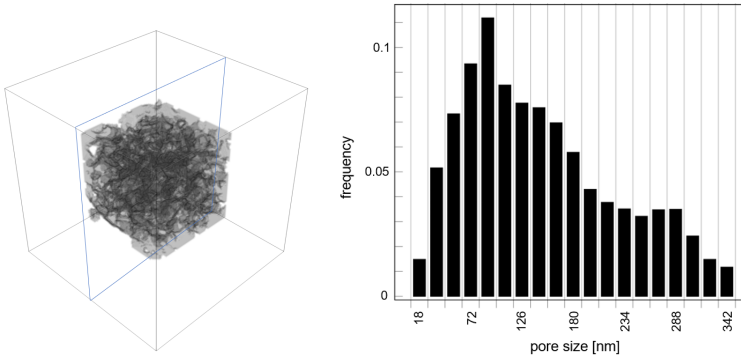

(a) 3D setup geometry (b) Pore size distribution

Figure 5.20.: 3D geometry with porous body and its pore size distribution [149]. The blue lines show the cut plane used for the further evaluation.

To investigate the effects of surface Helmholtz potential, ion concentrations, and carrier fluid inlet velocity on adsorption within the nanoporous microstructure, the temporal evolution of both maximal and spatially averaged saturation product sensitivities is analyzed. Additionally, the instantaneous spatial distributions of these sensitivities are examined, as in Figures 5.21 and 5.22.

5.2.2.1 Helmholtz potential influence

The sensitivity with respect to surface electric potential (Figures 5.21c and 5.21d) distinguishes between different types of pores in the realistic geometry. Pores exhibiting a negative derivative are identified as open pores, while those with a positive sensitivity are classified as blind pores, which also exhibit the highest saturation product. Given that the average sensitivity is negative, most pores are of the open type, explaining the significant difference between average and maximal saturation products. This sensitivity also has the highest norm among others, indicating that an increase in potential can lead to stronger saturation.

It can be concluded that using sensitivity analysis with respect to surface potential in a realistic geometry, allows for categorizing pores according to their types.

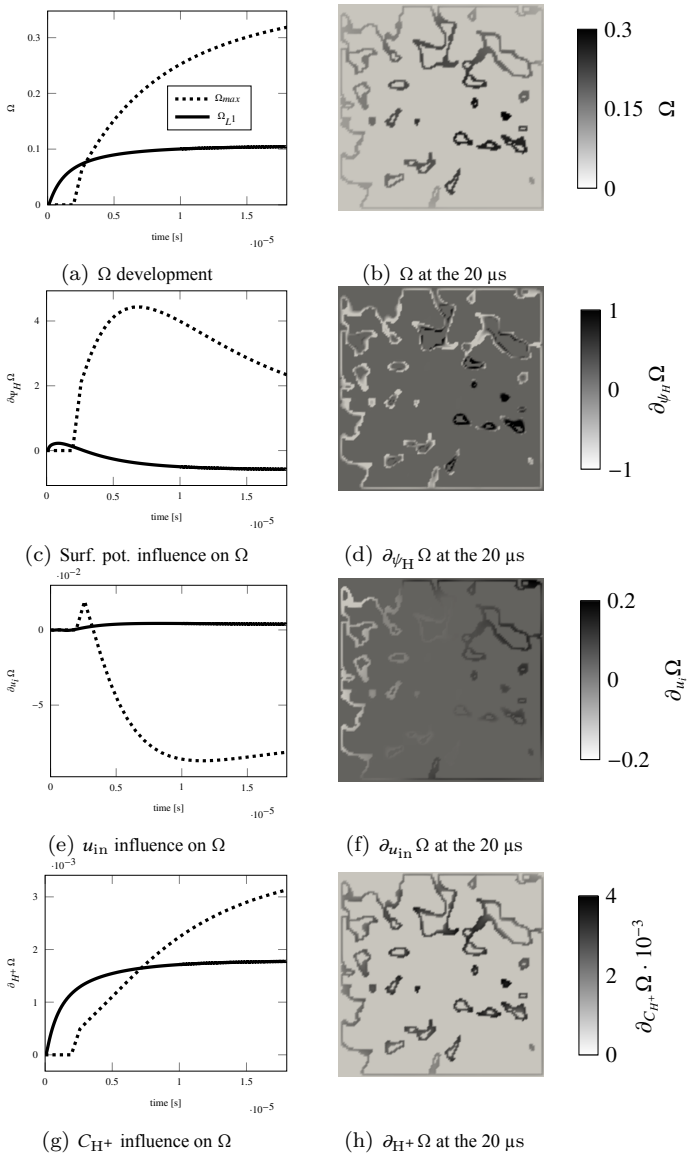

(a) Ω development (b) Ω at the 20 µs

(c) Surf. pot. influence on Ω (d) $\partial_{\psi_H}\Omega$ at the 20 µs

(e) u_{in} influence on Ω (f) $\partial_{u_{in}}\Omega$ at the 20 µs

(g) C_{H^+} influence on Ω (h) $\partial_{H^+}\Omega$ at the 20 µs

Figure 5.21.: Temporal development of average and maximal saturation product and its sensitivities (left) and spatial distribution of these values in a middle cut plane (right). Part I/II.

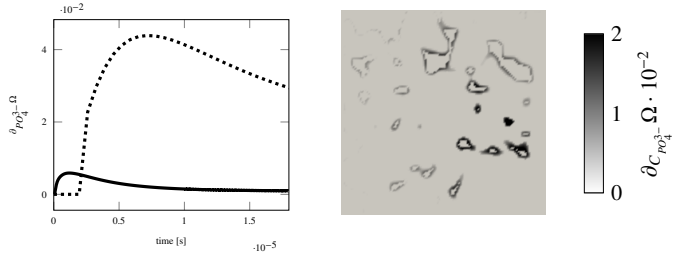

(a) $C_{\mathrm{PO}_4^{3+}}$ influence on Ω (b) $\partial_{\mathrm{PO}_4^{3+}} \Omega$ at the 20 µs

Figure 5.22.: Temporal development of average and maximal saturation product and its sensitivities (left) and spatial distribution of these values in a middle cut plane (right). Part II/II.

5.2.2.2 Influence of the inlet velocity

The impact of the inlet velocity is presented in Figures 5.21e and 5.21f. The average derivative of the saturation product with respect to carrier fluid inlet velocity remains negative, similarly to what is observed in the 2D simulations, given that most pores in the current geometry are open. However, the derivative in cells with maximal saturation product is positive, indicating a contrasting effect. An examination of the spatial distribution of this sensitivity reveals that in pores with high saturation, the derivative tends to be positive. This phenomenon can be attributed to phosphate accumulation in the dead zone leeway of, or inside the geometry. This demonstrates that, whenever there is a sufficient concentration of phosphate to interact with the solid phase of the porous system, the interaction becomes more dependent on the average pore flow rates.

Higher inlet velocity enhances saturation in cells located favorably in convenient spots (pores opened to outer flow dead zones where ions are gathering), but generally reduces saturation values at most blind cells, as it hinders accumulation of ions at one position and enables recovery of phosphate from the porous absorbents (see Figure 5.23). Due to this behavior, especially as the temporal influence tends toward negative sensitivity values, the fluid injection rates need to be optimized for effective trapping of phosphate. On the other hand, statistically, applying velocity to a large number of micro-particles may increase crystallization probability at some particles.

As such, due to the diminishing influence of the flow rate over time, optimizing the fluid injection rate is essential for effective adsorption in porous micro-particles. On the other side, increasing the flow rate (velocity) may enhance the likelihood of crystallization in certain micro-particles.

(a) With 0.2 $\mathrm{m\,s^{-1}}$ inlet velocity. $\Omega_{\max} = 0.455$.

(b) Without inlet velocity. $\Omega_{\max} = 0.437$.

Figure 5.23.: Saturation product with and without inlet velocity. Visualized are inner cells with $\Omega \geq 0.2$.

5.2.2.3 Influence of hydrogen and phosphate ions concentration

These sensitivity trends (Figures 5.21g, 5.21h, 5.22a, 5.22b) are generally weak but consistently positive across all regions. Increasing ion concentrations, as anticipated, result in higher saturation—in particular, in blind pores. The derivative with respect to phosphate concentration is stronger than that with respect to hydrogen concentration. The disparity between average and maximal values of these sensitivities is also substantial.

5.2.2.4 Influence of the total porous geometry volume

Considering the anisotropy of the pore structure taken into consideration, it is crucial to investigate the influence of the total pore geometry volume. In the original setup, a quarter of the Estaillades carbonate scan was simulated. Here, 45% of the scan's volume is simulated under identical conditions. The comparison of these two geometries and their resulting saturation products is illustrated in Figure 5.24. Simulating a larger portion of the porous rock CT scan results in higher local and average saturation product values that do not stabilize within the simulated time.

As such, it can be concluded that a larger geometry accumulates more ions due to longer pores, whilst maintaining the same pore size distribution.

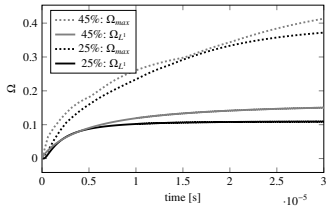

(a) Temporal development of average and maximal saturation products by two geometry sizes.

(b) $\alpha_{\text{geom}} = 25\%$ (c) $\alpha_{\text{geom}} = 45\%$

Figure 5.24.: Influence of the porous geometry size on the saturation product development.

5.2.2.5 Verification of 3D sensitivities by setup parameter variation

To verify the sensitivity analysis results of the realistic porous geometry, three different setups are considered (Table 5.3).

Setup	I	II	III
ψ_{H} [V]	+0.01	+0.02	+0.02
$C(\text{H}^+)$ [mol m^{-3}]	6	6	6
$C(\text{PO}_4^{3+})$ [mol m^{-3}]	1	1	1
u_{in} [m s^{-1}]	0	0	0
α_{geom} [%]	45	45	100

Table 5.3.: Parameter optimization on a realistic geometry.

The ions accumulate deeper in the pores when the surface electric potential is increased from Setup I to Setup II. This results in a lower average saturation product, but at the same time, in an increase of the maximum saturation product within the blind pores. Enlarging the geometry increases the average saturation due to the presence of deeper pores, which in turn require more time for diffusion processes to plateau. This trend is observed in the temporal development of the maximum saturation product in Setup III. In terms of spatial distribution, the saturation product and calcium ion concentration, which has the strongest influence on saturation, primarily accumulate towards the center of the geometry.

For phosphate saturation in CSH particles, the particle size is typically several hundred micrometers. In current research, a realistically porous particle with a side length of 0.72 µm is simulated. It can be assumed that simulating larger domains will yield higher saturation product values. Investigating this aspect will be part of the future research.

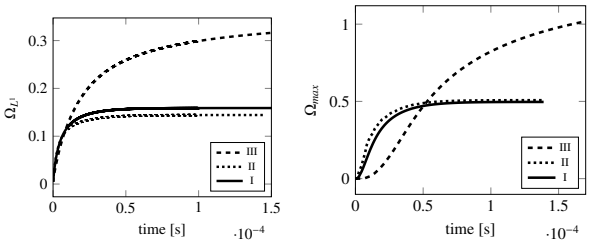

(a) Average saturation product (b) Maximal saturation product

Figure 5.25.: Saturation products development by Setups I, II and III on a realistic geometry.

It is observed that increasing the surface potential results in a lower average saturation product, while the maximum value of Ω is slightly higher and is reached in a shorter time. This is due to a stronger driving electric force based on the potential gradient. The size of the geometry taken into consideration produces the highest influence on the considered values, which grow twice by the Setup III in comparison to the Setup II (Figure 5.25). As already investigated in the Section 5.2.1.3, the highest saturation product is reached in the cells with the highest values of calcium ion concentration, as in the 3D simulations (Figures 5.26 and 5.27).

Figure 5.26.: Spatial distribution of calcium cation concentration and saturation product in the realistic 3D geometry by Setup III at the 170 µs in the middle cut plane.

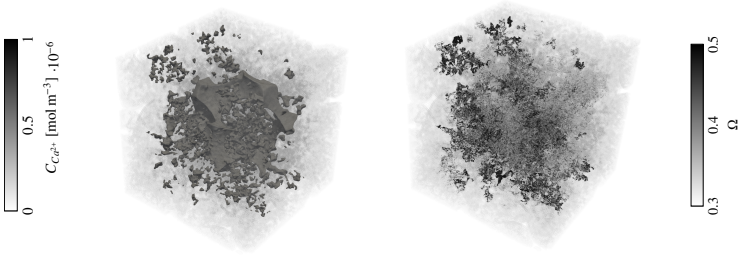

Figure 5.27.: Spatial distribution of calcium cation concentration and saturation product in the realistic 3D geometry by Setup III at the 170 µs.

The described results prove correctness of the previously presented sensitivity analysis.

5.3 Summary and answer to the third open question

In this Chapter, steps **S1.1–S2.3** of the numerical analysis (Section 1.3) of the crystallization reaction at the pore-scale are performed. A novel hydro-electrochemical three-dimensional simulation system for nano-porous resolved geometries is established and validated on analytical solutions. The performed tests show the possibility of omitting the internal Poisson calculation loop in the cases in which the final result is stationary or quasi-stationary, as the changes of Nernst-Planck and Navier-Stokes equations per one time step are much slower than the changes of electric potential. The coupled forward algorithmic

differentiation algorithm used for sensitivity analysis is validated using FDM. The resulting simulative investigation tool can be used for predicting different surface ionic reactions of liquids through nanoscale porous systems.

The goal of the current research at the nano-level was to explore the dependencies of phosphate saturation in porous CSH particles. Two-dimensional parameterized simplified porous micro-systems representing open and blind pores were investigated using the previously validated *RNSPNPE* model. A μCT-scan of Estaillades carbonate was taken and scaled to the necessary size for a 3D simulation of phosphate saturation in a realistic porous geometry.

After this short summary, the last main question can be partially answered

Q3: Which parameters have influence on the pore-level crystallization reaction?

The analysis revealed several *key findings*:

1. Saturation inside the porous body is significantly higher than on the outer surfaces. In blind pore systems, saturation increases towards the dead end as well as by open pores it grows towards the geometry center shifted along the carrier fluid movement direction.
2. Narrow pore width and large pore length promote oversaturation of the ionic solution, whereby deeper pores extend diffusion times for ions from the bulk.
3. Increasing electric surface potential enhances saturation at the end of blind pores but decreases it in open pores.
4. Higher concentrations of hydrogen and phosphate anions, combined with positive Helmholtz potential, consistently lead to higher saturation.
5. Calcium concentration has the strongest impact on OCP saturation, it can be investigated by observation of the total ion velocity that consists of the carrier fluid velocity, electric and diffusion velocities.
6. Carrier fluid velocity negatively influences saturation in open pores above a certain threshold, but can increase saturation in some blind pores if their inlets are located in dead zones of the flow. However, it decreases saturation in other blind pores.

7. Across all pore types, carrier fluid velocity accelerates the filling of pore volumes with ions from the bulk solution.
8. By using a larger geometry, the total pore length is increased, leading to a higher resulting average and local saturation products.

These findings underscore the complex interplay between geometry, surface potential, ion concentrations, and carrier fluid dynamics in determining phosphate saturation within porous CSH systems. By extending the current model with the crystallization reaction and adding a new boundary condition that allows fluid cells to become solid according to the formed crystal volume, the full crystallization process can be investigated. The presented simulation model and results are a solid foundation for further investigations.

6 Summary and conclusion

This thesis investigates multiple optimization possibilities for the phosphorus crystallization reaction, which is part of the P-RoC process developed at KIT by Berg *et al*. It aims to improve wastewater treatment and enhance the circular economy in chemical processing.

6.1 Summary

In the introduction (Chapter 1), the P-RoC process was presented, and the existing knowledge gaps, challenges, and key questions regarding crystallization process optimization were identified. A multiscale solution approach was introduced, consisting of several numerical analysis steps (**S1**–**S3**) applied to different parts of the process across multiple length scales (Section 1.3). Subsequently, in Chapter 2, fundamental modeling concepts and LBM discretization schemes were outlined, along with relevant characteristic numbers. Given the thesis focus on multiphase, multi-component, and reactive systems, particular attention was paid to transport equations for mass, momentum, and scalars, including turbulence modeling and multiphase Eulerian schemes. Basic principles of the LBM were also presented, followed by specialized LBM approaches for VANSE. At the end of the chapter, the methodology for simulation model validation was described. The content of this chapter provided the theoretical foundation for the subsequent parts of the thesis. All simulations at different length scales were implemented using the *OpenLB* software library and can be reproduced using the corresponding Git commits or provided examples. A detailed description of the cases is included in Appendix A.2.

Macro-level analysis (S1.1–S1.3)

At the macro-level, a full-size reactor simulation using the multiphase multicomponent Euler-Euler approach was created. For this work, CSH microparticles, dissolved phosphate, and particle loading were treated as an Eulerian secondary phase (Chapter 3). The heterogeneous reaction was modeled using the experimentally fitted mathematical expressions that incorporate mass transfer levels between bulk and unresolved particles. This simulation model was validated using analytical solutions for discontinuous and continuous reaction cases. Given the low volume fractions and small particle sizes, a one-way NSE and ADE coupling suffices. The model was applied to a static mixer with adsorbent particles moving with the carrier fluid at one inlet and dissolved phosphate at the other.

Contributions advancing the state of the art at the macroscale

A novel LBM model for the simulation of the adsorption on unresolved moving particles is built, which includes

- Coupling of separate phases for carrier fluid, solid particles, solved adsorptive, and particle loading,
- Different mass transfer mechanisms for distinct adsorption levels with LDF approach,
- Validation with convergency check on examples with analytical solutions,
- Application to a static mixer with moving particles.

Micro-level analysis (S1.1–S1.3)

For laminar and turbulent flows that involve the transport and reactions of chemical species, spatial resolution is critical. In the case of phosphate crystallization at the CSH microparticles, microscale is the relevant length scale for mixing and reacting processes from the microparticles' point of view.

Section 4.2 demonstrated that in laminar micro-mixers with low-diffusivity species, accurately representing flow substructures at the Batchelor scale is essential for proper calculation of mixing quality and reaction progression.

Numerical diffusion due to insufficient resolution artificially increased the reactant contact volume, leading to unrealistically high product yields. For cells with high Peclet numbers, stabilization required adding local artificial diffusion.

In turbulent flow simulations (Section 4.3), a turbulence model becomes necessary when the cell sizes exceed the Kolmogorov length scale. This model mathematically represents the flow resistance proportional to the unresolved vortex energy. In turbulent reactive flows with low-diffusivity species, the Peclet number is even higher than in laminar cases, placing the Batchelor scale within the nano-region. Resolving this scale is often unfeasible, necessitating stabilization approaches akin to those used in laminar cases. The added diffusion was scaled proportionally to the Peclet number. Accurate results require local adjustments to the source term to minimize numerical diffusion effects. This approach will be refined in future work.

Contributions advancing the state of the art at the microscale

The benchmark of a reactive T-micromixer is re-established with LES using LBM on multiple GPUs and an equidistant mesh in its complete volume, whereby

- Reactive flow is for the first time resolved until the Batchelor scale similar size in the whole geometry,
- Schmidt number stabilization method for high shear strain regions is for the first time applied in a laminar secondary flow,
- A convergence study is performed for the first time in this case.

Nano-level analysis (S1.1–S2.3)

The phosphate crystallization occurs on the surface of nanopores inside CSH microparticles. Therefore, to analyze the influencing factors on this reaction, it was modeled at this level (Chapter 5). In this context, transported chemical species in the vicinity of the reactive surface in a liquid water solution were treated as electrically charged ions. These ions move because of both the carrier fluid flow and the spatial gradient of the electric potential. At the surface, these ions react and saturate, eventually precipitating to form a crystalline hydrocomplex. The electric attraction of ions to the surface and their chemical

precipitation represent physical and chemical adsorption, which can only be fully analyzed at the nanopore scale.

The equations describing this complex system were discretized using the LBM within the NSPNPE. Each component of the system was validated against analytically solvable examples. The simplicity of the LBM algorithm facilitates the parallel implementation of forward AD for selected variables (e.g. saturation product) regarding boundary parameters such as inflow velocity, reactant concentrations, surface electric potential, and pore geometry (width and length). Sensitivity analysis of these variables offers significant time savings compared to neural network training on extensive datasets and enhances the simulation system's adaptability to various chemical reactions.

In Section 5.2, the results of the sensitivity analysis for the saturation product of OCP were presented and discussed. A notable conclusion was the significant influence of pore geometry, particularly the differences in adsorption processes between open and closed pores. Variations in pore length and width also substantially impact saturation. The parallelized simulation model enabled investigation of chemical processes in resolved, realistic porous microparticles, corroborating findings from simplified 2D geometries.

Contributions advancing the state of the art at the nanoscale

- LBM discretization of the reactive hydro-electrochemical dynamic equation system isfor the first time applied to three-dimensional simulation cases of complex hydro-electrochemical processes.
- The forward-mode AD approach is coupled for the first time with the developed solver to perform sensitivity analysis of key variables. The AD-based sensitivity results are validated against those obtained using FDM.
- A numerical sensitivity analysis of the OCP saturation product in simplified 2D and realistic 3D pore geometries with respect to carrier fluid velocity, hydrogen and phosphate ions concentrations in the bulk, pore walls' surface electric potential, pore type and dimensions is performed for the first time.

6.2 Conclusion

This thesis presented a multiscale investigation of phosphate crystallization within a stirred tank crystallization reactor, focusing on parameter optimization, species transport, and pore-level reaction mechanisms. The study was driven by three **open questions** defined in the Section 1.2, each addressing a different scale and aspect of the crystallization process. The answers to these questions collectively form a comprehensive understanding of the system and undertake the first basic steps on the way to an automatically optimizable crystallization reactor design.

Q1: Which crystallization process parameters are significant and can be optimized by a stirred tank crystallization reactor?

This question has been addressed in this thesis through the identification of key macroscopic process parameters by building and validating a multiphase multicomponent Euler-Euler simulation model with LDF-based adsorption reaction kinetics and a multilevel mass transfer mechanism representing the crystallization process in the nanopores of subgrid CSH microparticles. These significant parameters are particle size, porosity (through microparticle design), carrier fluid velocity, particle concentration, pH factor, and diffusion coefficients at the different adsorption levels. Reaction kinetics can also be modified according to the findings from the nano-level as soon as the full crystallization growth model is added to the saturation model created here. Using a validated gradient-based optimization solver [109], the model successfully recovers the critical adsorption parameters and demonstrates numerical robustness and precision. Although the phosphate concentration is predefined upstream, the model allows tuning of other influential variables, showing a high potential for real-world process optimization.

Which of the named parameters can be optimized so that the efficiency of the total process increases is still an open part of this question, which can be answered only after the findings from the smaller scales are incorporated into the macroscale simulation model.

Q2: Reaction happens at the level of microparticles within their nanopores, so how can the species mixing and reaction be correctly predicted?

This question has been conclusively answered, particularly in terms of numerical modeling. The thesis shows that accurate prediction of species mixing and reaction requires resolving flow and transport dynamics down to the Batchelor scale. DNS or fine LES are necessary for accurate mixing quality calculation, especially in regions with high shear stress. Moreover, the study proposes a Schmidt-number based ADE stabilization approach efficient in both laminar and turbulent flows. The simulation model is validated through the reestablishment of a T-micromixer benchmark. By insufficient resolutions, as will be the case in macroscopic simulation, the high numerical diffusion can be annihilated by a correction term, which needs to be elaborated in future work.

Q3: Which parameters influence the pore-level crystallization reaction?

This question has been comprehensively addressed through detailed pore-scale simulations and analysis. Several key parameters were identified. Saturation within porous bodies is significantly higher than at their outer surfaces, with blind pores showing increasing saturation toward their dead ends, and open pores exhibiting a peak near the geometric center in the flow direction. Narrow and deep pores promote oversaturation by slowing ion diffusion from the bulk. An increased electric surface potential raises saturation in blind pores but reduces it in open ones. High concentrations of hydrogen and phosphate ions, along with a positive Helmholtz potential, further enhance saturation, while calcium concentration exerts the strongest influence. The carrier fluid velocity has a complex role – beyond a certain threshold, it lowers saturation in open pores but may enhance it in blind pores located in flow dead zones, though overall predictability in realistic porous systems is limited. Nevertheless, increased velocity accelerates ion filling across all pore types. Larger geometries, with extended pore networks, tend to yield higher average and local saturation levels. The model's capability to analyze such fine-scale effects marks a significant advancement in understanding pore-level behavior, whereby the crystal nucleation and growth models are still missing, not allowing us to derive a novel crystallization kinetics expression for macroscopic simulations. This study will be part of the future works.

Overall evaluation

In summary, the thesis gives first significant insights into the phosphate crystallization process multiscale dynamics based on results provided by validated numerical simulation models addressing the three open questions **Q1–Q3**. This thesis introduces a holistic, robust, extendable, and HPC-compatible modeling framework capable of parameter optimization, resolved transport modeling, and pore-scale reaction analysis. Shown results prove the statement given in the introduction that the numerical analysis is a faster and cheaper way to look into the smallest process scales. This framework demonstrates a high potential for a physics-informed, automatically optimizable reactor design.

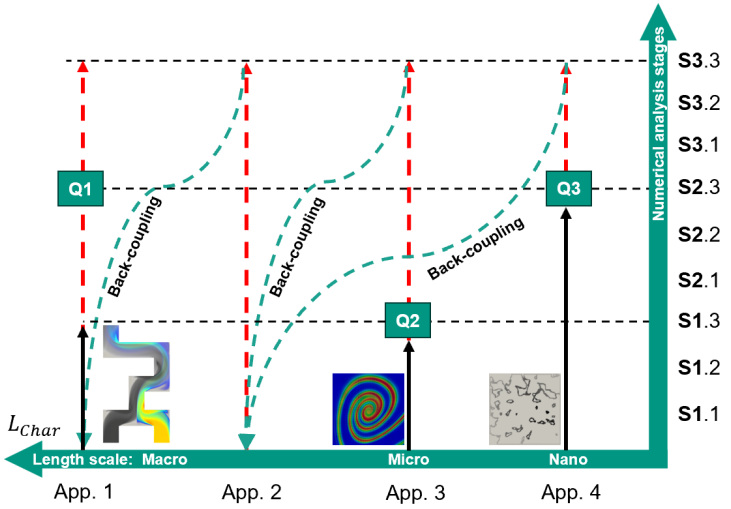

Figure 6.1.: Realized numerical analysis steps for building of a multiscale simulation model of the crystallization stirred tank reactor. Main questions are Q1–Q3. Main steps (Y-axis): S1 – Modeling and discretization. S2 – Sensitivity assessment and optimization. S3 – Reduced-order model. Substeps (Y-axis): 1. Implementation. 2. Validation. 3. Application. Partial application cases for representation of the reactor (X-axis): App. 1 – Heterogeneous mixing and reaction on subgrid particles. App. 2 – Heterogeneous mixing and reactions on resolved particles. App. 3 – Homogeneous mixing and reaction in bulk. App. 4 – Surface reaction in resolved nano-pores. Black arrows show the performed steps, the red lines – the remaining steps.

Figure 6.1 summarizes the progress in the multiscale coupled modeling of the crystallization reactor. At the *macroscale*, a novel LBM-based model was

developed to simulate adsorption on unresolved moving particles. It features multiphase coupling, advanced mass transfer modeling using the LDF approach, and was validated against analytical solutions, with successful application in a static mixer scenario (**App. 1, S1.1–S1.3**).

At the *microscale*, the reactive T-micromixer benchmark was re-implemented using LES with LBM on multi-GPU architectures and a fully equidistant mesh. This allowed, for the first time, resolution down to Batchelor-scale-like structures, application of Schmidt number stabilization in laminar secondary flows, and a full convergence study (**App. 3, S1.1–S1.3**).

At the *nanoscale*, LBM was, for the first time, applied to 3D simulations of reactive hydro-electrochemical processes. A forward-mode AD approach was integrated into the solver for sensitivity analysis, validated against finite difference methods. Additionally, a comprehensive sensitivity study of OCP saturation in 2D and 3D pore geometries was conducted, accounting for fluid velocity, ion concentrations, pore geometry, and surface potentials (**App. 4, S1.1–S2.3**).

While certain steps are marked as future work, the current study lays a strong, validated foundation. It bridges the gap between macroscale process control and pore-scale physical chemistry, contributing both methodological tools and mechanistic insights to the field of practically relevant crystallization chemistry.

Acknowledgment

This work was performed on the HoreKa supercomputer funded by the Ministry of Science, Research and the Arts Baden-Württemberg and by the Federal Ministry of Education and Research.

The current research is a part of the DFG project number 436212129 ”Increase of efficiency in phosphate recovery by understanding the interaction of flow and loading processes with modeling and simulation”.

Bibliography

[1] *Verordnung zur Neuordnung der Klärschlammverwertung (Klärschlammverordnung – AbfKlärV)*. German. Bundesgesetzblatt Teil I, S. 3465. Last amended by Article 6 of the Ordinance of 27 September 2017. 2017. URL: https://www.bgbl.de/xaver/bgbl/start.xav?startbk=Bundesanzeiger_BGBl&jumpTo=bgbl117s3465.pdf.

[2] U. Berg, G. Knoll, E. Kaschka, V. Kreutzer, D. Donnert, P. G. Weidler, and R. Nüesch. «P-RoC-Phosphorus recovery from wastewater by crystallisation of calcium phosphate compounds». In: *Journal of residuals science and technology* 4.3 (2005).

[3] D. Montag, W. Everding, S. Malms, J. Pinnekamp, J. Reinhardt, H. Fehrenbach, U. Arnold, M. Trimborn, H. Goldbach, W. Klett, et al. *Bewertung konkreter Maßnahmen einer weitergehenden Phosphorrückgewinnung aus relevanten Stoffströmen sowie zum effizienten Phosphoreinsatz*. Tech. rep. Umweltbundesamt, 2015.

[4] L. Egle, H. Rechberger, and M. Zessner. *Endbericht Phosphorrückgewinnung aus dem Abwasser*. Tech. rep. Technische Universität Wien, 2014.

[5] Z. Zhang, X. Wang, and J. Zhao. «Phosphate recovery from wastewater using calcium silicate hydrate (C-S-H): sonochemical synthesis and properties». In: *Environmental Science: Water Research & Technology* 5.1 (2019), pp. 131–139. ISSN: 2053-1419. DOI: 10.1039/C8EW00643A. URL: https://pubs.rsc.org/en/content/articlelanding/2019/ew/c8ew00643a.

[6] M. Krause. «Through Numerical Simulation to Scientific Knowledge». In: June 2023, pp. 201–215. ISBN: 978-3-658-36973-6. DOI: 10.1007/978-3-658-36974-3_16.

[7] T. Henn, G. Thäter, W. Dörfler, H. Nirschl, and M. J. Krause. «Parallel dilute particulate flow simulations in the human nasal cavity». In: *Computers & Fluids* 124 (2016), pp. 197–207. ISSN: 00457930. DOI: 10.1016/j.compfluid.2015.08.002.

[8] T. Krüger, H. Kusumaatmaja, A. Kuzmin, O. Shardt, G. Silva, and E. M. Viggen. *The Lattice Boltzmann Method*. Cham: Springer International Publishing, 2017. ISBN: 978-3-319-44647-9. DOI: 10.1007/978-3-319-44649-3.

[9] M. J. Krause, A. Kummerländer, S. J. Avis, H. Kusumaatmaja, D. Dapelo, F. Klemens, M. Gaedtke, N. Hafen, A. Mink, R. Trunk, J. E. Marquardt, M. L. Maier, M. Haussmann, and S. Simonis. «OpenLB—Open source lattice Boltzmann code». In: *Computers & Mathematics with Applications* 81 (2021), pp. 258–288. ISSN: 0898-1221. DOI: 10.1016/J.CAMWA.2020.04.033.

[10] M. Haussmann, F. Ries, J. B. Jeppener-Haltenhoff, Y. Li, M. Schmidt, C. Welch, L. Illmann, B. Böhm, H. Nirschl, M. J. Krause, and A. Sadiki. «Evaluation of a Near-Wall-Modeled Large Eddy Lattice Boltzmann Method for the Analysis of Complex Flows Relevant to IC Engines». In: *Computation* 8.2 (2020). DOI: 10.25534/tuprints-00013372.

[11] Z. Peng, S. Liu, Y. Li, Z. Deng, and H. Feng. «Pore-Scale Lattice Boltzmann Simulation of Gas Diffusion–Adsorption Kinetics Considering Adsorption-Induced Diffusivity Change». In: *Energies* 13.18 (2020), p. 4927. DOI: 10.3390/en13184927. URL: https://www.mdpi.com/1996-1073/13/18/4927.

[12] Z. Peng, Z. Deng, H. Feng, S. Liu, and Y. Li. «Multiscale Lattice Boltzmann Simulation of the Kinetics Process of Methane Desorption-Diffusion in Coal». In: *ACS Omega* 6.30 (2021), pp. 19789–19798. DOI: 10.1021/acsomega.1c02499.

[13] M.-L. Maier, S. Milles, S. Schuhmann, G. Guthausen, H. Nirschl, and M. J. Krause. «Fluid flow simulations verified by measurements to investigate adsorption processes in a static mixer». In: *Computers & Mathematics with Applications* 76.11-12 (2018), pp. 2744–2757. ISSN: 0898-1221. DOI: 10.1016/j.camwa.2018.08.066.

[14] Q. Ma, Z. Chen, and H. Liu. «Multiple-relaxation-time lattice Boltzmann simulation for flow, mass transfer, and adsorption in porous media». In: *Physical review. E* 96.1-1 (2017), p. 013313. DOI: 10.1103/PhysRevE.96.013313.

[15] C. Kaplan, D. Mott, and E. Oran. «Towards the design of efficient micromixers». In: *42nd AIAA Aerospace Sciences Meeting and Exhibit*. 2004, p. 931. DOI: 10.2514/6.2004-931. eprint: https://arc.aiaa.org/doi/pdf/10.2514/6.2004-931. URL: https://arc.aiaa.org/doi/abs/10.2514/6.2004-931.

[16] C. Kaplan, J. Liu, D. Mott, and E. Oran. «Computations of Chaotic Flow in a Passive Micromixer». In: *36th AIAA Fluid Dynamics Conference and Exhibit*. 2006, p. 3716. DOI: 10.2514/6.2006-3716. eprint: https://arc.aiaa.org/doi/pdf/10.2514/6.2006-3716. URL: https://arc.aiaa.org/doi/abs/10.2514/6.2006-3716.

[17] A. N. Kolmogorov. «Local structure of turbulence in an incompressible fluid at very high Reynolds numbers». In: *Dokl. Akad. Nauk SSSR* 30 (1941a), pp. 299–303.

[18] G. K. Batchelor. «Small-scale variation of convected quantities like temperature in turbulent fluid Part 1. General discussion and the case of small conductivity». In: *Journal of Fluid Mechanics* 5.1 (1959), pp. 113–133. DOI: 10.1017/S002211205900009X.

[19] S. Schwolow, J. Hollmann, B. Schenkel, and T. Röder. «Application-oriented analysis of mixing performance in microreactors». In: *Organic Process Research & Development* 16 (Sept. 2012), pp. 1513–1522. DOI: 10.1021/op300107z.

[20] M.-A. Schneider and F. Stoessel. «Determination of the kinetic parameters of fast exothermal reactions using a novel microreactor-based calorimeter». In: *Chemical Engineering Journal* 115.1 (2005), pp. 73–83. ISSN: 1385-8947. DOI: https://doi.org/10.1016/j.cej.2005.09.019. URL: https://www.sciencedirect.com/science/article/pii/S1385894705003414.

[21] O. Wörz. «Wozu Mikroreaktoren?» In: *Chemie in unserer Zeit* 34.1 (2000), pp. 24–29. DOI: https://doi.org/10.1002/(SICI)1521-3781(200002)34:1<24::AID-CIUZ24>3.0.CO;2-A.

[22] H. Pennemann, V. Hessel, and H. Löwe. «Chemical microprocess technology—from laboratory-scale to production». In: *Chemical Engineering Science* 59.22 (2004). ISCRE18, pp. 4789–4794. ISSN: 0009-2509. DOI: https://doi.org/10.1016/j.ces.2004.07.049. URL: https://www.sciencedirect.com/science/article/pii/S000925090400483X.

[23] V. Hessel, P. Löb, and H. Löwe. «Industrial microreactor process development up to production». English. In: *Micro process engineering, Volume 3: System, process and plant engineering*. Ed. by V. Hessel, A. Renken, J. Schouten, and J. Yoshida. Germany: Wiley-VCH Verlag, 2009, pp. 183–247. ISBN: 978-3-527-31550-5.

[24] B. K. Johnson and R. K. Prud'homme. «Chemical processing and micromixing in confined impinging jets». In: *AIChE Journal* 49.9 (2003), pp. 2264–2282. DOI: https://doi.org/10.1002/aic.690490905. eprint: https://aiche.onlinelibrary.wiley.com/doi/pdf/10.1002/aic.690490905. URL: https://aiche.onlinelibrary.wiley.com/doi/abs/10.1002/aic.690490905.

[25] Y. Diao, T. Harada, A. S. Myerson, T. A. Hatton, and B. L. Trout. «The role of nanopore shape in surface-induced crystallization». In: *Nature Materials* 10.11 (2011), pp. 867–871. DOI: 10.1038/nmat3117. URL: https://doi.org/10.1038/nmat3117.

[26] W. Guan, F. Ji, Q. Chen, P. Yan, and L. Pei. «Synthesis and enhanced phosphate recovery property of porous calcium silicate hydrate using polyethyleneglycol as pore-generation agent». In: *Materials* 6.7 (2013), pp. 2846–2861. ISSN: 1996-1944. DOI: 10.3390/ma6072846. URL: https://www.mdpi.com/1996-1944/6/7/2846.

[27] A. Trapote-Barreira, J. Cama, and J. M. Soler. «Dissolution kinetics of C–S–H gel: Flow-through experiments». In: *Physics and Chemistry of the Earth, Parts A/B/C* 70-71 (2014). Mechanisms and Modelling of Waste-Cement and Cement-Host Rock Interactions, pp. 17–31. ISSN: 1474-7065. DOI: https://doi.org/10.1016/j.pce.2013.11.003. URL: https://www.sciencedirect.com/science/article/pii/S1474706513001794.

[28] H. Su, J. Hu, and H. Li. «Multi-scale performance simulation and effect analysis for hydraulic concrete submitted to leaching and frost». In: *Engineering with Computers* 34 (2018), pp. 821–842. DOI: 10.1007/s00366-018-0575-9.

[29] K. Fukushi, A. Okuyama, N. Takeda, and S. Kosugi. «Parameterization of adsorption onto minerals by Extended Triple Layer Model». In: *Applied Geochemistry* 134 (2021), p. 105087. ISSN: 0883-2927. DOI: https://doi.org/10.1016/j.apgeochem.2021.105087. URL: https://www.sciencedirect.com/science/article/pii/S0883292721002183.

[30] M. Uwaha. «8 - Growth kinetics: Basics of crystal growth mechanisms». In: *Handbook of Crystal Growth (Second Edition)*. Ed. by T. Nishinaga. Second Edition. Boston: Elsevier, 2015, pp. 359–399. ISBN: 978-0-444-56369-9. DOI: https://doi.org/10.1016/B978-0-444-56369-9.00008-3. URL: https://www.sciencedirect.com/science/article/pii/B9780444563699000083.

[31] D. Kim, N. Mahabadi, J. Jang, and L. A. van Paassen. «Assessing the kinetics and pore-scale characteristics of biological calcium carbonate precipitation in porous media using a microfluidic chip experiment». In: *Water Resources Research* 56.2 (2020). e2019WR025420 2019WR025420, e2019WR025420. DOI: https://doi.org/10.1029/2019WR025420. eprint: https://agupubs.onlinelibrary.wiley.com/doi/pdf/10.1029/2019WR025420. URL: https://agupubs.onlinelibrary.wiley.com/doi/abs/10.1029/2019WR025420.

[32] M. Ahkami, A. Parmigiani, P. Di Palma, M. Saar, and X. Kong. «A lattice-Boltzmann study of permeability-porosity relationships and mineral precipitation patterns in fractured porous media». In: *Computational Geosciences* 24 (Oct. 2020). DOI: 10.1007/s10596-019-09926-4.

[33] D. Dapelo, F. Bukreev, M. J. Krause, and J. Bridgeman. «Lattice-Boltzmann methods for dispersed, mixed and transitional fluid flows: a review of current approaches towards a general multiphase/multicomponent Eulerian model». In: *Submitted to Archives of Computational Methods in Engineering* (2025).

[34] F. Bukreev, F. Raichle, H. Nirschl, and M. J. Krause. «Simulation of adsorption processes on moving particles based on an Euler-Euler description using a lattice Boltzmann discretization». In: *Chemical Engineering Science* 270 (2023), p. 118485. ISSN: 0009-2509. DOI: https://doi.org/10.1016/j.ces.2023.118485. URL: https://www.sciencedirect.com/science/article/pii/S0009250923000416.

[35] F. Bukreev, A. Kummerländer, J. Jeßberger, D. Teutscher, S. Simonis, D. Bothe, and M. J. Krause. «Benchmark Simulation of Laminar Reactive Micromixing Using Lattice Boltzmann Methods». In: *AIAA Journal* 0.0 (0), pp. 1–10. DOI: 10.2514/1.J064234. eprint: https://doi.org/10.2514/1.J064234. URL: https://doi.org/10.2514/1.J064234.

[36] F. Bukreev, A. Kummerländer, J. Jeßberger, D. Teutscher, S. Ito, S. Simonis, D. Dapelo, M. M. Nezhad, H. Nirschl, and M. J. Krause. «A hybrid Lattice-Boltzmann model for hydro-electrochemical modeling and sensitivity analysis of crystallization potential in nanoporous media. Part I: simulation model». In: *Engineering with Computers* (2025). ISSN: 1435-5663. DOI: 10.1007/s00366-025-02216-x. URL: https://doi.org/10.1007/s00366-025-02216-x.

[37] F. Bukreev, A. Kummerländer, J. Jeßberger, D. Teutscher, S. Ito, S. Simonis, D. Dapelo, M. M. Nezhad, H. Nirschl, and M. J. Krause. «A hybrid Lattice-Boltzmann model for hydro-electrochemical modeling and sensitivity analysis of crystallization potential in nanoporous media. Part II: application to the identification and quantification of influencing factors of phosphate saturation». In: *Engineering with Computers* (2025). ISSN: 1435-5663. DOI: 10.1007/s00366-025-02217-w. URL: https://doi.org/10.1007/s00366-025-02217-w.

[38] B. E. Rapp. «Chapter 9 - Fluids». In: *Microfluidics: Modelling, Mechanics and Mathematics*. Ed. by B. E. Rapp. Micro and Nano Technologies. Oxford: Elsevier, 2017, pp. 243–263. ISBN: 978-1-4557-3141-1. DOI: https://doi.org/10.1016/B978-1-4557-3141-1.50009-5. URL: https://www.sciencedirect.com/science/article/pii/B9781455731411500095.

[39] N. Nguyen, S. Wereley, and S. Shaegh. *Fundamentals and Applications of Microfluidics, Third Edition*. Artech House integrated microsystems series. Artech House, 2019. ISBN: 9781630813659. URL: https://books.google.de/books?id=h3iFDwAAQBAJ.

[40] A. Selmi, S. Bhapkar, C. Nagel, A. Kummerländer, and M. J. Krause. «Simulation of Temperature Driven Microflows Using a Lattice Boltzmann Method in Slip and Moderate Transition Regimes». In: *2023 24th International Conference on Thermal, Mechanical and Multi-Physics Simulation and Experiments in Microelectronics and Microsystems (EuroSimE)*. 2023, pp. 1–6. DOI: 10.1109/EuroSimE56861.2023.10100812.

[41] A. Schmidt and U. Renz. «Eulerian computation of heat transfer in fluidized beds». In: *Chemical Engineering Science* 54.22 (1999), pp. 5515–5522. ISSN: 00092509. DOI: 10.1016/S0009-2509(99)00298-5. URL: https://www.sciencedirect.com/science/article/pii/S0009250999002985.

[42] J. R. Backhurst, J. H. Harker, J. F. Richardson, and J. M. Coulson. *Chemical Engineering Volume 1: Fluid Flow, Heat Transfer and Mass Transfer*. Ed. by R. P. Chhabra. 6th ed. Softcover, 928 pages. Oxford: Butterworth-Heinemann Ltd, 1999. ISBN: 978-0-7506-4444-0.

[43] W. Schröder. *Fluidmechanik*. 4th ed. Vol. 16. ABS. Paperback, 354 Seiten. Wiesbaden: Springer Vieweg, 2020. ISBN: 978-3-95886-221-0.

[44] S. V. Patankar. *Numerical Heat Transfer and Fluid Flow*. Hardcover, 214 pages. Boca Raton: CRC Press, 1980. ISBN: 978-0-89116-522-4.

[45] J. H. Ferziger and M. Perić. *Computational Methods for Fluid Dynamics*. third, rev. edition. Springer eBook Collection. Heidelberg: Springer, 2002. ISBN: 9783642560262. DOI: 10.1007/978-3-642-56026-2.

[46] A. Leonard. «Energy Cascade in Large Eddy Simulations of Turbulent Fluid Flow». In: *Adv. Geophys.* 18A (Jan. 1974), pp. 237–248. DOI: 10.1016/S0065-2687(08)60464-1.

[47] J. Smagorinsky. «General circulation experiments with the primitive equations». In: *Monthly Weather Review* 91.3 (Jan. 1963), p. 99. DOI: 10.1175/1520-0493(1963)091<0099:GCEWTP>2.3.CO;2.

[48] K. E. Lilly. «On the application of the eddy viscosity concept in the Inertial sub-range of turbulence». In: 1966.

[49] M. Haussmann, S. Simonis, H. Nirschl, and M. J. Krause. «Direct numerical simulation of decaying homogeneous isotropic turbulence—numerical experiments on stability, consistency and accuracy of distinct lattice Boltzmann methods». In: *International Journal of Modern Physics C* 30.09 (2019), p. 1950074. DOI: 10.1142/S0129183119500748.

[50] M. Siodlaczek, M. Gaedtke, S. Simonis, M. Schweiker, N. Homma, and M. J. Krause. «Numerical evaluation of thermal comfort using a large eddy lattice Boltzmann method». In: *Building and Environment* 192 (2021), p. 107618. DOI: 10.1016/j.buildenv.2021.107618.

[51] S. Shu, J. Zhang, and N. Yang. «GPU-accelerated transient lattice Boltzmann simulation of bubble column reactors». In: *Chemical Engineering Science* 214 (2020), p. 115436. ISSN: 0009-2509. DOI: https://doi.org/10.1016/j.ces.2019.115436. URL: https://www.sciencedirect.com/science/article/pii/S0009250919309261.

[52] S. Shu, N. Yang, F. Bertrand, and J. Chaouki. «High-resolution simulation of oscillating bubble plumes in a square cross-sectioned bubble column with an unsteady k-epsilon model». In: *Chemical Engineering Science* 231 (2021), p. 116321. ISSN: 0009-2509. DOI: https://doi.org/10.1016/j.ces.2020.116321. URL: https://www.sciencedirect.com/science/article/pii/S0009250920308538.

[53] COMSOL AB. *COMSOL Multiphysics Reference Manual*. COMSOL AB. Stockholm, Sweden, 2023. URL: https://www.comsol.com.

[54] A. Sokolichin, S. Becker, and G. Eigenberger. «Modellierung und Numerische Simulation von G/L-Blasen Strömungen». In: *Chemie Ingenieur Technik* 66.4 (1994), pp. 505–510. DOI: https://doi.org/10.1002/cite.330660411. eprint: https://onlinelibrary.wiley.com/doi/pdf/10.1002/cite.330660411. URL: https://onlinelibrary.wiley.com/doi/abs/10.1002/cite.330660411.

[55] M. A. A. Spaid and J. Phelan Frederick R. «Lattice Boltzmann methods for modeling microscale flow in fibrous porous media». In: *Physics of Fluids* 9.9 (Sept. 1997), pp. 2468–2474. ISSN: 1070-6631. DOI: 10.1063/1.869392. eprint: https://pubs.aip.org/aip/pof/article-pdf/9/9/2468/12477935/2468_1_online.pdf. URL: https://doi.org/10.1063/1.869392.

[56] S. Simonis, N. Hafen, J. Jeßberger, D. Dapelo, G. Thäter, and M. J. Krause. *Homogenized lattice Boltzmann methods for fluid flow through porous media – part I: kinetic model derivation*. 2023. arXiv: 2310.14746 [math.NA]. URL: https://arxiv.org/abs/2310.14746.

[57] Z. Guo and T. S. Zhao. «Lattice Boltzmann model for incompressible flows through porous media». In: *Phys. Rev. E* 66 (3 Sept. 2002), p. 036304. DOI: 10.1103/PhysRevE.66.036304. URL: https://link.aps.org/doi/10.1103/PhysRevE.66.036304.

[58] L. Wang, L.-P. Wang, Z. Guo, and J. Mi. «Volume-averaged macroscopic equation for fluid flow in moving porous media». In: *International Journal of Heat and Mass Transfer* 82 (2015), pp. 357–368. ISSN: 0017-9310. DOI: https://doi.org/10.1016/j.ijheatmasstransfer.2014.11.056. URL: https://www.sciencedirect.com/science/article/pii/S0017931014010448.

[59] J. Zhang, L. Wang, and J. Ouyang. «Lattice Boltzmann model for the volume-averaged Navier-Stokes equations». In: *Europhysics Letters* 107.2 (July 2014), p. 20001. DOI: 10.1209/0295-5075/107/20001. URL: https://dx.doi.org/10.1209/0295-5075/107/20001.

[60] S. B. Höcker, R. Trunk, W. Dörfler, and M. J. Krause. «Towards the simulations of inertial dense particulate flows with a volume-averaged lattice Boltzmann method». In: *Computers & Fluids* 166 (2018), pp. 152–162. ISSN: 0045-7930. DOI: https://doi.org/10.1016/j.compfluid.2018.02.011. URL: https://www.sciencedirect.com/science/article/pii/S0045793018300665.

[61] B. Blais, J.-M. Tucny, D. Vidal, and F. Bertrand. «A conservative lattice Boltzmann model for the volume-averaged Navier–Stokes equations based on a novel collision operator». In: *Journal of Computational Physics* 294 (2015), pp. 258–273. DOI: 10.1016/j.jcp.2015.03.036.

[62] F. Bukreev, S. Simonis, A. Kummerländer, J. Jeßberger, and M. J. Krause. «Consistent lattice Boltzmann methods for the volume averaged Navier–Stokes equations». In: *Journal of Computational Physics* 490 (2023), p. 112301. ISSN: 0021-9991. DOI: https://doi.org/10.1016/j.jcp.2023.112301. URL: https://www.sciencedirect.com/science/article/pii/S0021999123003960.

[63] S. Fu, Z. Hao, and L. Wang. «A pressure-based lattice Boltzmann method for the volume-averaged Navier-Stokes equations». In: *Journal of Computational Physics* 516 (2024), p. 113350. ISSN: 0021-9991. DOI: https://doi.org/10.1016/j.jcp.2024.113350. URL: https://www.sciencedirect.com/science/article/pii/S0021999124005989.

[64] R. Trunk, T. Henn, W. Dörfler, H. Nirschl, and M. J. Krause. «Inertial dilute particulate fluid flow simulations with an Euler–Euler lattice Boltzmann method». In: *Journal of Computational Science* 17 (2016). Discrete Simulation of Fluid Dynamics 2015, pp. 438–445. ISSN: 1877-7503. DOI: https://doi.org/10.1016/j.jocs.2016.03.013. URL: https://www.sciencedirect.com/science/article/pii/S1877750316300345.

[65] ANSYS Inc. *ANSYS Theory Guide*. Release 2023 R1. ANSYS Inc. Canonsburg, PA, USA, 2023. URL: https://www.ansys.com.

[66] W. Reschetilowski. *Handbuch Chemische Reaktoren Grundlagen und Anwendungen der Chemischen Reaktionstechnik: Grundlagen und Anwendungen der Chemischen Reaktionstechnik*. Berlin Heidelberg: Springer Spektrum, Jan. 2020. DOI: 10.1007/978-3-662-56444-8.

[67] K. Sattler. *Thermische Trennverfahren*. John Wiley & Sons, Ltd., 2001. DOI: 10.1002/3527603328.ch1a.

[68] M. Bohnet. *Mechanische Verfahrenstechnik*. John Wiley & Sons, Ltd, 2003. DOI: 10.1002/9783527663569.fmatter.

[69] P. Nithiarasu, K. Seetharamu, and T. Sundararajan. «Natural convective heat transfer in a fluid saturated variable porosity medium». In: *International Journal of Heat and Mass Transfer* 40.16 (1997), pp. 3955–3967. ISSN: 0017-9310. DOI: https://doi.org/10.1016/S0017-9310(97)00008-2. URL: https://www.sciencedirect.com/science/article/pii/S0017931097000082.

[70] D. Gidaspow. *Multiphase Flow and Fluidization*. San Diego: Academic Press, 1994. DOI: 10.1016/C2009-0-21244-X.

[71] T. Zhu. «Unsteady porous–media flow». PhD thesis. Technische Universität München, 2016. URL: https://mediatum.ub.tum.de/doc/1279870/1279870.pdf.

[72] K. Hiltunen, A. Jäsberg, S. Kallio, H. Karema, M. Kataja, A. Koponen, M. Manninen, and V. Taivassalo. *Multiphase flow dynamics: Theory and numerics*. VTT Publications 722. VTT Technical Research Centre of Finland, 2009.

[73] A. Kummerländer, F. Bukreev, S. Berg, M. Dorn, and M. J. Krause. «Advances in Computational Process Engineering using Lattice Boltzmann Methods on High Performance Computers». In: *High Performance Computing in Science and Engineering '22*. Springer, 2024. ISBN: 978-3-031-46869-8. DOI: 10.1007/978-3-031-46869-8.

[74] D. Hänel. *Molekulare Gasdynamik : Einführung in die kinetische Theorie der Gase und Lattice-Boltzmann-Methoden*. Berlin Heidelberg: Springer, 2004. DOI: 10.1007/3-540-35047-0.

[75] T. Krüger, H. Kusumaatmaja, A. Kuzmin, O. Shardt, G. Silva, and E. M. Viggen. *The Lattice Boltzmann Method - Principles and Practice*. Springer Cham, 2016. DOI: 10.1007/978-3-319-44649-3.

[76] H. Grad. «On the kinetic theory of rarefied gases». In: *Communications on Pure and Applied Mathematics* 2.4 (1949), pp. 331–407. DOI: https://doi.org/10.1002/cpa.3160020403. eprint: https://onlinelibrary.wiley.com/doi/pdf/10.1002/cpa.3160020403. URL: https://onlinelibrary.wiley.com/doi/abs/10.1002/cpa.3160020403.

[77] Z. Guo, C. Zheng, and B. Shi. «Discrete lattice effects on the forcing term in the lattice Boltzmann method». In: *Phys. Rev. E* 65 (4 Apr. 2002), p. 046308. DOI: 10.1103/PhysRevE.65.046308. URL: https://link.aps.org/doi/10.1103/PhysRevE.65.046308.

[78] Z. Chai and B. Shi. «A novel lattice Boltzmann model for the Poisson equation». In: *Applied Mathematical Modelling* 32.10 (2008), pp. 2050–2058. ISSN: 0307-904X. DOI: https://doi.org/10.1016/j.apm.2007.06.033. URL: https://www.sciencedirect.com/science/article/pii/S0307904X07001722.

[79] J. Latt, B. Chopard, O. Malaspinas, M. Deville, and A. Michler. «Straight velocity boundaries in the lattice Boltzmann method». In: *Phys. Rev. E* 77 (5 May 2008), p. 056703. DOI: 10.1103/PhysRevE.77.056703. URL: https://link.aps.org/doi/10.1103/PhysRevE.77.056703.

[80] X. He and L.-S. Luo. «Lattice Boltzmann Model for the Incompressible Navier–Stokes Equation». In: *Journal of Statistical Physics* 88.3-4 (1997), pp. 927–944. DOI: 10.1023/B:JOSS.0000015179.12689.e4. URL: https://doi.org/10.1023/B:JOSS.0000015179.12689.e4.

[81] R. Allen and T. Reis. «Moment-based boundary conditions for lattice Boltzmann simulations of natural convection in cavities». In: *Progress in Computational Fluid Dynamics, an International Journal* 16.4 (2016), pp. 216–231. DOI: 10.1504/PCFD.2016.077296. eprint: https://www.inderscienceonline.com/doi/pdf/10.1504/PCFD.2016.077296. URL: https://www.inderscienceonline.com/doi/abs/10.1504/PCFD.2016.077296.

[82] W. Oberkampf and C. Roy. *Verification and Validation in Scientific Computing*. Cambridge University Press, 2010. DOI: 10.1017/CBO9780511760396.

[83] D. Micale, R. Uglietti, M. Bracconi, and M. Maestri. «Coupling Euler-Euler and Microkinetic Modeling for the Simulation of Fluidized Bed Reactors: an Application to the Oxidative Coupling of Methane». In: *Industrial & Engineering Chemistry Research* 60.18 (2021), pp. 6687–6697. ISSN: 0888-5885. DOI: 10.1021/acs.iecr.0c05845.

[84] L. A. Vandewalle, G. B. Marin, and K. M. van Geem. «catchyFOAM: Euler–Euler CFD Simulations of Fluidized Bed Reactors with Microkinetic Modeling of Gas-Phase and Catalytic Surface Chemistry». In: *Energy & Fuels* 35.3 (2021), pp. 2545–2561. ISSN: 0887-0624. DOI: 10.1021/acs.energyfuels.0c02824.

[85] D. M. LeVan, G. Carta, and K. S. Walton. «Adsorption and Ion Exchange». In: *Perry's chemical engineers' handbook*. Ed. by D. W. Green and M. Z. Southard. New York: McGraw Hill Education, 2019, pp. 16-1 - 16–54. ISBN: 9780071834094.

[86] E. Glueckauf and J. I. Coates. «Theory of chromatography; the influence of incomplete equilibrium on the front boundary of chromatograms and on the effectiveness of separation». In: *Journal of the Chemical Society (Resumed)* 0 (1947), pp. 1315–1321. ISSN: 0368-1769. DOI: 10.1039/JR9470001315. URL: https://pubs.rsc.org/en/content/articlelanding/1947/jr/jr9470001315/unauth.

[87] H.-K. Hsuen. «An improved linear driving force approximation for intraparticle adsorption». In: *Chemical Engineering Science* 55.17 (2000), pp. 3475–3480. ISSN: 00092509. DOI: 10.1016/S0009-2509(99)00600-4. URL: https://www.sciencedirect.com/science/article/pii/S0009250999006004.

[88] S. Sircar and J. R. Hufton. «Why Does the Linear Driving Force Model for Adsorption Kinetics Work?» In: *Adsorption* 6.2 (2000), pp. 137–147. ISSN: 1572-8757. DOI: 10.1023/A:1008965317983. URL: https://link.springer.com/article/10.1023/A:1008965317983.

[89] C. H. Liaw, J. S. P. Wang, R. A. Greenkorn, and K. C. Chao. «Kinetics of fixed-bed adsorption: A new solution». In: *AIChE Journal* 25.2 (1979), pp. 376–381. ISSN: 1547-5905. DOI: 10.1002/aic.690250229. URL: https://aiche.onlinelibrary.wiley.com/doi/10.1002/aic.690250229.

[90] K. Hashimoto and K. Miura. «A simplified method to design fixed-bed adsorbers for the Freundlich isotherm». In: *JOURNAL OF CHEMICAL ENGINEERING OF JAPAN* 9.5 (1976), pp. 388–392. ISSN: 0021-9592. DOI: 10.1252/jcej.9.388.

[91] E. Worch. «Fixed-bed adsorption in drinking water treatment: a critical review on models and parameter estimation». In: *Journal of Water Supply: Research and Technology-Aqua* 57.3 (2008), pp. 171–183. ISSN: 0003-7214. DOI: 10.2166/aqua.2008.100.

[92] E. Worch. *Adsorption technology in water treatment: Fundamentals, processes, and modeling*. 2nd, revised edition. Berlin Germany and Boston: De Gruyter, 2021. ISBN: 9783110715422.

[93] I. Neretnieks. «Analysis of some adsorption experiments with activated carbon». In: *Chemical Engineering Science* 31.11 (1976), pp. 1029–1035. ISSN: 00092509. DOI: 10.1016/0009-2509(76)87023-6. URL: https://www.sciencedirect.com/science/article/pii/0009250976870236.

[94] T. Choong and D. M. Scott. «The linear driving force model for cyclic adsorption and desorption: the effect of external fluid-film mass transfer». In: *Chemical Engineering Science* 53.4 (1998), pp. 847–851. ISSN: 00092509. DOI: 10.1016/S0009-2509(97)00345-X. URL: https://www.sciencedirect.com/science/article/pii/S000925099700345X.

[95] T. Seta. «Implicit temperature-correction-based immersed-boundary thermal lattice Boltzmann method for the simulation of natural convection». In: *Physical review. E, Statistical, nonlinear, and soft matter physics* 87.6 (2013), p. 063304. DOI: 10.1103/PhysRevE.87.063304.

[96] N. S. Raghavan and D. M. Ruthven. «Numerical simulation of a fixed-bed adsorption column by the method of orthogonal collocation». In: *AIChE Journal* 29.6 (1983), pp. 922–925. ISSN: 1547-5905. DOI: 10.1002/aic.690290608. URL: https://aiche.onlinelibrary.wiley.com/doi/10.1002/aic.690290608.

[97] P. Virtanen et al. «SciPy 1.0: Fundamental Algorithms for Scientific Computing in Python». In: *Nature Methods* 17 (2020), pp. 261–272. DOI: 10.1038/s41592-019-0686-2.

[98] S. Simonis, M. Frank, and M. J. Krause. «On relaxation systems and their relation to discrete velocity Boltzmann models for scalar advection–diffusion equations». In: *Philosophical Transactions of the Royal Society A* 378 (2020), p. 20190400. DOI: 10.1098/rsta.2019.0400.

[99] S. Simonis, M. Frank, and M. J. Krause. «Constructing relaxation systems for lattice Boltzmann methods». In: *Applied Mathematics Letters* 137 (2023), p. 108484. DOI: 10.1016/j.aml.2022.108484.

[100] S. Simonis, M. Haussmann, L. Kronberg, W. Dörfler, and M. J. Krause. «Linear and brute force stability of orthogonal moment multiple-relaxation-time lattice Boltzmann methods applied to homogeneous isotropic turbulence». In: *Philosophical Transactions of the Royal Society A* 379.2208 (2021), p. 20200405. DOI: 10.1098/rsta.2020.0405.

[101] S. Simonis, D. Oberle, M. Gaedtke, P. Jenny, and M. J. Krause. «Temporal large eddy simulation with lattice Boltzmann methods». In: *Journal of Computational Physics* 454 (2022), p. 110991. DOI: 10.1016/j.jcp.2022.110991.

[102] Z. Chai, B. Shi, and Z. Guo. «A multiple-relaxation-time lattice Boltzmann model for general nonlinear anisotropic convection–diffusion equations». In: *Journal of Scientific Computing* 69.1 (2016), pp. 355–390. DOI: 10.1007/s10915-016-0198-5.

[103] Z. Chai and B. Shi. «Multiple-relaxation-time lattice Boltzmann method for the Navier-Stokes and nonlinear convection-diffusion equations: Modeling, analysis, and elements». In: *Phys. Rev. E* 102 (2 Aug. 2020), p. 023306. DOI: 10.1103/PhysRevE.102.023306.

[104] I. Ginzburg. «Equilibrium-type and link-type lattice Boltzmann models for generic advection and anisotropic-dispersion equation». In: *Advances in Water Resources* 28.11 (2005), pp. 1171–1195. ISSN: 0309-1708. DOI: 10.1016/j.advwatres.2005.03.004.

[105] B. Chopard, J. L. Falcone, and J. Latt. «The lattice Boltzmann advection-diffusion model revisited». In: *The European Physical Journal Special Topics* 171.1 (2009), pp. 245–249. DOI: 10.1140/epjst/e2009-01035-5.

[106] D. Dapelo, S. Simonis, M. J. Krause, and J. Bridgeman. «Lattice-Boltzmann coupled models for advection–diffusion flow on a wide range of Péclet numbers». In: *Journal of Computational Science* 51 (2021), p. 101363. DOI: 10.1016/j.jocs.2021.101363.

[107] S. A. Hosseini, N. Darabiha, D. Thévenin, and A. Eshghinejadfard. «Stability limits of the single relaxation-time advection–diffusion lattice Boltzmann scheme». In: *International Journal of Modern Physics C* 28.12 (2017), p. 1750141. DOI: 10.1142/S0129183117501418.

[108] Z. Zhang, Z. Li, and Y. Wu. «Advection–Diffusion Lattice Boltzmann Method With and Without Dynamical Filter». In: *Frontiers in Physics* 10 (2022). DOI: 10.3389/fphy.2022.875628.

[109] S. Ito, S. Großmann, F. Bukreev, J. Jeßberger, and M. J. Krause. «Benchmark case for the inverse determination of adsorption parameters using lattice Boltzmann methods and gradient-based optimization». In: *Chemical Engineering Science* 309 (2025), p. 121467. ISSN: 0009-2509. DOI: https://doi.org/10.1016/j.ces.2025.121467. URL: https://www.sciencedirect.com/science/article/pii/S0009250925002908.

[110] C. Stemich. «Theoretische und numerische Untersuchung des Strömungsmischens in einem T-förmigen Mikromischer». dissertation. Universität Paderborn, 2006. URL: https://nbn-resolving.org/urn:nbn:de:hbz:466-2007021993.

[111] D. Bothe, A. Lojewski, and H.-J. Warnecke. «Fully resolved numerical simulation of reactive mixing in a T-shaped micromixer using parabolized species equations». In: *Chemical Engineering Science - CHEM ENG SCI* 66 (Dec. 2011), pp. 6424–6440. DOI: 10.1016/j.ces.2011.08.045.

[112] C. Galletti, A. Mariotti, L. Siconolfi, R. Mauri, and E. Brunazzi. «Numerical investigation of flow regimes in T-shaped micromixers: Benchmark between finite volume and spectral element methods». In: *The Canadian Journal of Chemical Engineering* 97.2 (2019), pp. 528–541. DOI: https://doi.org/10.1002/cjce.23321. eprint: https://onlinelibrary.wiley.com/doi/pdf/10.1002/cjce.23321. URL: https://onlinelibrary.wiley.com/doi/abs/10.1002/cjce.23321.

[113] A. Lobasov and A. Minakov. «Analyzing mixing quality in a T-shaped micromixer for different fluids properties through numerical simulation». In: *Chemical Engineering and Processing - Process Intensification* 124 (2018), pp. 11–23. ISSN: 0255-2701. DOI: https://doi.org/10.1016/j.cep.2017.11.004. URL: https://www.sciencedirect.com/science/article/pii/S0255270117303306.

[114] S. Tokas, M. Zunaid, and M. A. Ansari. «Numerical investigation of the performance of 3D-helical passive micromixer with Newtonian fluid and non-Newtonian fluid blood». In: *Asia-Pacific Journal of Chemical Engineering* 16.1 (2021). e2570 APJ-20-0294.R1, e2570. DOI: https://doi.org/10.1002/apj.2570. eprint: https://onlinelibrary.wiley.com/doi/pdf/10.1002/apj.2570. URL: https://onlinelibrary.wiley.com/doi/abs/10.1002/apj.2570.

[115] C. Fonte, D. Fletcher, P. Guichardon, and J. Aubin. «Simulation of micromixing in a T-mixer under laminar flow conditions». In: *Chemical Engineering Science* 222 (Apr. 2020), p. 115706. DOI: 10.1016/j.ces.2020.115706.

[116] J. Jeßberger, J. E. Marquardt, L. Heim, J. Mangold, F. Bukreev, and M. J. Krause. «Optimization of a micromixer with automatic differentiation». In: *Fluids* 7.5 (2022). ISSN: 2311-5521. DOI: 10.3390/fluids7050144. URL: https://www.mdpi.com/2311-5521/7/5/144.

[117] D. Bothe, C. Stemich, and H.-J. Warnecke. «Fluid mixing in a T-shaped micro-mixer». In: *Chemical Engineering Science* 61 (2006), pp. 2950–2958.

[118] D. Bothe, A. Lojewski, and H.-J. Warnecke. «Computational analysis of an instantaneous chemical reaction in a T-microreactor». In: *AIChE Journal* 56.6 (2010), pp. 1406–1415. DOI: https://doi.org/10.1002/aic.12067. eprint: https://aiche.onlinelibrary.wiley.com/doi/pdf/10.1002/aic.12067. URL: https://aiche.onlinelibrary.wiley.com/doi/abs/10.1002/aic.12067.

[119] A. Kummerländer, M. Dorn, M. Frank, and M. J. Krause. «Implicit propagation of directly addressed grids in lattice Boltzmann methods». In: *Concurrency and Computation: Practice and Experience* 35.8 (2023), e7509. DOI: https://doi.org/10.1002/cpe.7509. eprint: https://onlinelibrary.wiley.com/doi/pdf/10.1002/cpe.7509. URL: https://onlinelibrary.wiley.com/doi/abs/10.1002/cpe.7509.

[120] A. Lojewski. «Computergestützte Analyse des reaktiven Strömungsmischens in T-Mikroreaktoren». dissertation. RWTH Aachen, 2010.

[121] M. Hettel, F. Bukreev, E. Daymo, A. Kummerländer, M. J. Krause, and O. Deutschmann. «Calculation of Single and Multiple Low Reynolds Number Free Jets with a Lattice-Boltzmann Method». In: *AIAA Journal* 0.0 (0), pp. 1–14. DOI: 10.2514/1.J064280. eprint: https://doi.org/10.2514/1.J064280. URL: https://doi.org/10.2514/1.J064280.

[122] A. Kummerländer, F. Bukreev, D. Teutscher, M. Dorn, and M. J. Krause. «Optimization of Single Node Load Balancing for Lattice Boltzmann Methods on Heterogeneous High Performance Computers». In: *preprint* (2025). Available at SSRN: https://ssrn.com/abstract=4713497 or http://dx.doi.org/10.2139/ssrn.4713497.

[123] P. A. Kler, E. J. López, L. D. Dalcín, F. A. Guarnieri, and M. A. Storti. «High performance simulations of electrokinetic flow and transport in microfluidic chips». In: *Computer Methods in Applied Mechanics and Engineering* 198.30 (2009), pp. 2360–2367. ISSN: 0045-7825. DOI: https://doi.org/10.1016/j.cma.2009.02.028. URL: https://www.sciencedirect.com/science/article/pii/S0045782509000991.

[124] R. Barnett, F. Municchi, J. King, et al. «Electrochemical transport modelling and open-source simulation of pore-scale solid–liquid systems». In: *Engineering with Computers* 39 (2023), pp. 4129–4152. DOI: 10.1007/s00366-023-01828-5.

[125] E. M. Ryan and P. P. Mukherjee. «Mesoscale modeling in electrochemical devices—A critical perspective». In: *Progress in Energy and Combustion Science* 71 (2019), pp. 118–142. ISSN: 0360-1285. DOI: https://doi.org/10.1016/j.pecs.2018.11.002. URL: https://www.sciencedirect.com/science/article/pii/S0360128518300078.

[126] L. Zhang and M. Wang. «Modeling of electrokinetic reactive transport in micropore using a coupled lattice Boltzmann method». In: *Journal of Geophysical Research: Solid Earth* 120.5 (2015), pp. 2877–2890. DOI: https://doi.org/10.1002/2014JB011812. eprint: https://agupubs.onlinelibrary.wiley.com/doi/pdf/10.1002/2014JB011812. URL: https://agupubs.onlinelibrary.wiley.com/doi/abs/10.1002/2014JB011812.

[127] X. He and N. Li. «Lattice Boltzmann simulation of electrochemical systems». In: *Computer Physics Communications* 129.1 (2000), pp. 158–166. ISSN: 0010-4655. DOI: https://doi.org/10.1016/S0010-4655(00)00103-X. URL: https://www.sciencedirect.com/science/article/pii/S001046550000103X.

[128] D. Zhang, W. Liu, C.-Y. Wu, and Q. Cai. «The development of a 3D pore-scale lattice Boltzmann model for 3D microstructure modeling and design of Li-ion battery electrodes». In: *Energy Technology* 10.7 (2022), p. 2200080. DOI: https://doi.org/10.1002/ente.202200080. eprint: https://onlinelibrary.wiley.com/doi/pdf/10.1002/ente.202200080. URL: https://onlinelibrary.wiley.com/doi/abs/10.1002/ente.202200080.

[129] *ICMENS '04: Proceedings of the 2004 International Conference on MEMS, NANO and Smart Systems*. USA: IEEE Computer Society, 2004. ISBN: 0769521894.

[130] R. Hunter. *Foundations of colloid science*. Oxford University Press, 2001. ISBN: 9780198505020. URL: https://books.google.de/books?id=-UVCAQAAIAAJ.

[131] J. Ross-Jones, M. Gaedtke, S. Sonnick, M. Rädle, H. Nirschl, and M. J. Krause. «Conjugate heat transfer through nano scale porous media to optimize vacuum insulation panels with lattice Boltzmann methods». In: *Computers & Mathematics with Applications* 77.1 (2019), pp. 209–221. ISSN: 0898-1221. DOI: https://doi.org/10.1016/j.camwa.2018.09.023. URL: https://www.sciencedirect.com/science/article/pii/S0898122118305352.

[132] J. Ross-Jones, M. Gaedtke, S. Sonnick, M. Meier, M. Rädle, H. Nirschl, and M. J. Krause. «Pore-scale conjugate heat transfer simulations using lattice Boltzmann methods for industrial applications». In: *Applied Thermal Engineering* 182 (2021), p. 116073. ISSN: 1359-4311. DOI: https://doi.org/10.1016/j.applthermaleng.2020.116073. URL: https://www.sciencedirect.com/science/article/pii/S1359431120335535.

[133] J. Fu, M. Wang, B. Chen, et al. «A data-driven framework for permeability prediction of natural porous rocks via microstructural characterization and pore-scale simulation». In: *Engineering with Computers* 39 (2023), pp. 3895–3926. DOI: 10.1007/s00366-023-01841-8.

[134] A. Trapote-Barreira, J. Cama, and J. M. Soler. «Dissolution kinetics of C–S–H gel: Flow-through experiments». In: *Physics and Chemistry of the Earth, Parts A/B/C* 70-71 (2014). Mechanisms and Modelling of Waste-Cement and Cement-Host Rock Interactions, pp. 17–31. ISSN: 1474-7065. DOI: https://doi.org/10.1016/j.pce.2013.11.003. URL: https://www.sciencedirect.com/science/article/pii/S1474706513001794.

[135] S. Graham and P. W. Brown. «Reactions of octacalcium phosphate to form hydroxyapatite». In: *Journal of Crystal Growth* 165.1 (1996), pp. 106–115. ISSN: 0022-0248. DOI: https://doi.org/10.1016/0022-0248(95)00994-9. URL: https://www.sciencedirect.com/science/article/pii/0022024895009949.

[136] D. L. Parkhurst and C. A. J. Appelo. *Description of input and examples for PHREEQC version 3–A computer program for speciation, batch-reaction, one-dimensional transport, and inverse geochemical calculations*. Techniques and Methods. U.S. Geological Survey, 2013. Chap. A43, p. 497. URL: http://pubs.usgs.gov/tm/06/a43.

[137] A. M. Holtzer. «The collected papers of Peter J. W. Debye. Interscience, New York-London, 1954. xxi + 700 pp., $9.50.» In: *Journal of Polymer Science* 13.72 (1954), pp. 548–548. DOI: https://doi.org/10.1002/pol.1954.120137203. eprint: https://onlinelibrary.wiley.com/doi/pdf/10.1002/pol.1954.120137203. URL: https://onlinelibrary.wiley.com/doi/abs/10.1002/pol.1954.120137203.

[138] F. Tian, B. Li, and D. Kwok. «Lattice Boltzmann simulation of electroosmotic flows in micro- and nanochannels». In: *2004 International Conference on MEMS, NANO and Smart Systems (ICMENS'04)*. 2004, pp. 294–299. DOI: 10.1109/ICMENS.2004.1508964.

[139] F. F. Chen. «Diffusion and resistivity». In: *Introduction to Plasma Physics and Controlled Fusion*. Cham: Springer International Publishing, 2016, pp. 145–185. ISBN: 978-3-319-22309-4. DOI: 10.1007/978-3-319-22309-4_5.

[140] Y. Marcus. *Ion properties / Yizhak Marcus.* eng. New York: Marcel Dekker, 1997. ISBN: 0824700112.

[141] M. Tung, N. Eidelman, B. Sieck, and W. Brown. «Octacalcium phosphate solubility product from 4 to 37-degree-C». In: *Journal of Research of the National Bureau of Standards* 93 (Sept. 1988), p. 613. DOI: 10.6028/jres.093.153.

[142] J. Heughebaert and G. Nancollas. «ChemInform Abstract: Kinetics of crystallization of octacalcium phosphate». In: *Chemischer Informationsdienst* 15 (Sept. 1984). DOI: 10.1002/chin.198438004.

[143] Y. Marcus. «Ionic radii in aqueous solutions». In: *Chemical Reviews* 88.8 (1988), pp. 1475–1498. DOI: 10.1021/cr00090a003. eprint: https://doi.org/10.1021/cr00090a003. URL: https://doi.org/10.1021/cr00090a003.

[144] A. Griewank and A. Walther. *Evaluating derivatives*. Second. Society for Industrial and Applied Mathematics (SIAM), Philadelphia, PA, 2008, pp. xxii+438. ISBN: 978-0-898716-59-7. DOI: 10.1137/1.9780898717761. URL: https://doi.org/10.1137/1.9780898717761.

[145] M. D. Gunzburger. *Perspectives in flow control and optimization*. Society for Industrial and Applied Mathematics, 2002. DOI: 10.1137/1.9780898718720. eprint: https://epubs.siam.org/doi/pdf/10.1137/1.9780898718720. URL: https://epubs.siam.org/doi/abs/10.1137/1.9780898718720.

[146] M. J. Krause and V. Heuveline. «Parallel fluid Flow control and optimisation with lattice Boltzmann methods and automatic differentiation». In: *Computers and Fluids* 80 (July 2013), pp. 28–36. DOI: 10.1016/j.compfluid.2012.07.026.

[147] S. Ito, J. Jeßberger, S. Simonis, F. Bukreev, A. Kummerländer, A. Zimmermann, G. Thäter, G. R. Pesch, J. Thöming, and M. J. Krause. «Identification of reaction rate parameters from uncertain spatially distributed concentration data using gradient-based PDE constrained optimization». In: *Computers & Mathematics with Applications* 167 (2024), pp. 249–263. ISSN: 0898-1221. DOI: https://doi.org/10.1016/j.camwa.2024.05.026. URL: https://www.sciencedirect.com/science/article/pii/S0898122124002451.

[148] J. Rouquerol, D. Avnir, C. W. Fairbridge, D. H. Everett, J. M. Haynes, N. Pernicone, J. D. F. Ramsay, K. S. W. Sing, and K. K. Unger. In: *Pure and Applied Chemistry* 66.8 (1994), pp. 1739–1758. DOI: doi:10.1351/pac199466081739. URL: https://doi.org/10.1351/pac199466081739.

[149] *DyMAS: A direct multi-scale pore-level simulation approach*. Vol. Day 3 Tue, April 25, 2017. SPE Western Regional Meeting. Apr. 2017, D031S007R004. DOI: 10.2118/185720-MS. eprint: https://onepetro.org/SPEWRM/proceedings-pdf/17WRM/3-17WRM/D031S007R004/1289648/spe-185720-ms.pdf. URL: https://doi.org/10.2118/185720-MS.

[150] P. L. Bhatnagar, E. P. Gross, and M. Krook. «A model for collision processes in gases. I. Small amplitude processes in charged and neutral one-component systems». In: *Phys. Rev.* 94 (3 May 1954), pp. 511–525. DOI: 10.1103/PhysRev.94.511. URL: https://link.aps.org/doi/10.1103/PhysRev.94.511.

[151] J. Zhang, L. Wang, and J. Ouyang. «Lattice Boltzmann Model for The Volume-Averaged Navier-Stokes Equations». In: *EPL (Europhysics Letters)* 107 (June 2014), p. 20001. DOI: 10.1209/0295-5075/107/20001.

[152] M.-L. Maier. «Coupled lattice Boltzmann and discrete element method for reactive particle fluid flows with applications in process engineering». PhD thesis. Karlsruher Institut für Technologie (KIT), 2021. 121 pp. DOI: 10.5445/IR/1000132643.

[153] P. Roache. «Code Verification by the Method of Manufactured Solutions». In: *Journal of Fluids Engineering* 124 (2002), p. 4. DOI: 10.1115/1.1436090.

[154] B. Blais and F. Bertrand. «On the use of the method of manufactured solutions for the verification of CFD codes for the volume-averaged Navier–Stokes equations». In: *Computers & Fluids* 114 (2015), pp. 121–129. DOI: 10.1016/j.compfluid.2015.03.002.

[155] A. Kummerländer, T. Bingert, F. Bukreev, L. E. Czelusniak, D. Dapelo, S. Englert, N. Hafen, M. Heinzelmann, S. Ito, J. Jeßberger, F. Kaiser, E. Kummer, H. Kusumaatmaja, J. E. Marquardt, M. Rennick, T. Pertzel, F. Prinz, M. Sadric, M. Schecher, S. Simonis, P. Sitter, D. Teutscher, M. Zhong, and M. J. Krause. *OpenLB User Guide 1.7*. Version 1.7r0. Feb. 2024. DOI: 10.5281/zenodo.13293033. URL: https://doi.org/10.5281/zenodo.13293033.

[156] A. Kummerländer et al. *OpenLB Release 1.8.1: Open Source Lattice Boltzmann Code*. Version 1.8.1. May 2025. DOI: 10.5281/zenodo.15440776. URL: https://doi.org/10.5281/zenodo.15440776.

Nomenclature

Abbreviations

AD	Algorithmic differentiation
ADE	Advection-diffusion equation
BGK	Bhatnagar-Gross-Krook
BTC	Breakthrough curve
CE	Chapman–Enskog
CFD	Computational fluid dynamics
CPU	Central processing unit
CSH	Calcium silicate hydrate
CT	Computed tomography
DNS	Direct numerical simulation
EDL	Electric double layer
EOC	Experimental order of convergence
FDM	Finite differences method
FVM	Finite volume method
GPU	Graphics processing unit
HPC	High performance cluster
IAP	Ionic activity product
IUPAC	International Union of Pure and Applied Chemistry
LB	Lattice Boltzmann
LBE	Lattice Boltzmann equation
LBM	Lattice Boltzmann methods
LDF	Linear driving force
LES	Large eddy simulation
LIF	Laser induces fluorescence
MFP	Mean free path
MMS	Method of manufactured solutions
MTZ	Mass transfer zone
NSE	Navier-Stokes equations
NSPNPE	Navier-Stokes-Poisson-Nernst-Planck equations
OCP	Octacalcium phosphate
ODE	Ordinary differential equation
PE	Poisson equation
PDE	Partial differential equation
PDF	Particle distribution function
PNPE	Poisson Nernst-Planck equation
P-RoC	Phosphorus Recovery from Wastewater by Crystall. of Calc. Phosph. Compounds
RADE	Reactive advection-diffusion equation
RNPE	Reactive Nernst-Planck equation
RNSPNPE	Reactive Navier-Stokes-Poisson-Nernst-Planck equations
SGS	Subgrid-scale
TKE	Turbulent kinetic energy
ULES	Uniform large eddy simulation
VANSE	Volume-averaged Navier–Stokes equations

Physics variables

A, B	Specific Debye constants	V	Volume
A_s	Particle surface area	$\dot{V}$	Volume flow
C	Specie concentration	X	Dimensionless concentration
C_S	Smagorinsky constant	a	Ionic activity
D	Specie diffusivity, Dimensions number	a_0	Smallest distance between ions
		α_T	Thermal diffusivity
D_b	Dispersion factor	$\boldsymbol{x}$	Coordinates vector
D_num	Numerical diffusion constant	b	Control variable, parameter
D_s	Surface diffusion coefficient	c_s	Speed of sound
E	Electric field strength	δ	Kronecker symbol
F	Faraday constant	d_m	Molecular distance
$\boldsymbol{F}$	Force vector	e	Elementary charge
I	Ionic strength	ϵ	Electric permittivity, Label parameter for Kn
K_sp	Saturation point constant		
Kn	Knudsen number	ϵ_TKE	TKE dissipation rate
L	Total/characteristic length	η	Machine precision
L^1	L1 error norm	f	LB population
L^2	L2 error norm	f^eq	LB equilibrium population
L^∞	infinity error norm	$\boldsymbol{g}$	Gravitational acceleration
M	Molar mass Moment of LB populations	h	Coefficient in analytical PE, Height
M^eq	Moment of equilibrium populations	γ	Ion activity coefficient
Ma	Mach number	γ_T	Specific heat ratio
N	Number density	k_B	Boltzmann constant
N_A	Avogadro number	k_f	Forward reaction rate constant, Film mass transfer coefficient
N_node	Number of cells		
N_t	Number of time steps	k_s	Surface mass transfer coefficient, Total mass transfer coefficient
Q	Number of lattice directions		
Q_c	Q-criterion	$l_{x/y}$	plane dimensions
Q_s	Source/sink term	m	Mass
Q_cs	Cross section area	$\dot{m}$	Mass flow
Pe	Peclet number	λ	Mean free path (MFP)
Pr	Prandtl number	λ_D	Debye length
R	Reaction term	μ	Dynamic viscosity Step size for difference quotients
R_g	Universal gas constant		
Re	Reynolds number	n	Crystallization order
S	Source term	ν	Kinematic viscosity
$\bar{S}$	Strain rate tensor	$\boldsymbol{\xi}$	Molecular velocity vector
Sc	Schmidt number	$\boldsymbol{\xi}_i$	Lattice normalized velocity vector
St	Stokes number	Ω	Saturation product
T	Temperature	Ω^C	Collision operator
$\boldsymbol{T}$	Stress tensor	Ω^S	Source term operator
U	Characteristic velocity	p	Pressure

ψ	Electric potential
ψ_{H}	Surface Helmholtz electric potential
$\bar{q}$	Actual particle loading
q_{s}	Surface equilibrium loading
ρ	Density
r	Reaction rate
r_{p}	Particle radius
σ_{T}	Temkin coefficient
τ	Lattice relaxation time
s	Scalar, quantity
$\boldsymbol{s}$	Vector
t	Time
τ	Lattice relaxation time
v	Stoichiometric coefficient
ϕ	Volume fraction, porosity
ϕ_{B}	Reactor bed porosity
$\triangle t$	Time step size
$\triangle x$	Cell size
u	Velocity vector component
$\boldsymbol{u}$	Velocity vector
ϑ	Stoichiometric coefficient
w	Lattice weight
z	Ion valence
η_{B}	Batchelor length scale
η_{K}	Kolmogorov length scale

Subscripts

+	Cations
−	Anions
0	Initial/inlet value
b	Phasic
A	Adsorbent
F	Force
PC	Pressure correction
R	Reactor
a	Analytical
abs	Absolute
b	Breakthrough
ad	Advection
avg	Average
α, β	Einstein summation indices
c	Node index, continuous
diss	Dissolution
eff	Effective
el	Electric
fl	Fluid
i	Species, ions
in	Inlet
j	Lattice direction
k	Reaction index
	General subscript
l, m	Time step indices
	by convergence check
max	Maximal
mol	Molecular
n	Numerical/normal
p	Particle
r	Residence
rec	Reconstructed
rel	Relative
s	Scalar, surface
st	stabilization, stoichiometric
t	Turbulent, total
x, y	Coordinates x and y
DH	Debye-Hückel

A Appendix

A.1 VANSE-LBM

This section is based on a published article: ***Bukreev, F.****, Simonis, S., Kummerländer, A., Jeßberger, J., Krause, M. J. (2023). Consistent lattice Boltzmann methods for the volume averaged Navier–Stokes equations. Journal of Computational Physics, 489, 112301. DOI:10.1016/j.jcp.2023.112301*

The applications used here are listed in the Section A.2.4.

After chemical processes are analyzed at the three distinct scales, an attempt to build an own VANSE-LBM approach is undertaken. It is necessary for a correct Euler-Euler multiphase modeling as well as for the representation of a flow through porous media. The goal of this attempt is to get a consistent scheme capable of reproducing second-order convergent pressure, which is more sensitive in LBM than in velocity.

The Section is structured as follows. First, the principles of VANSE and the corresponding existing LBM scheme are presented, after which a novel VANSE-LBM is derived. In particular, novel population moments are presented and locally varying void fractions are taken into account. In Section A.1.2, the validation of the new correction is performed on stationary and transient examples. The numerical results suggest a second-order convergence of flow velocity and pressure. Further, the CE expansion, formally proving the approximation of the VANSE with the present LBM up to higher-order terms, is detailed in A.1.3.

A.1.1 VANSE-LBM with extended pressure correction

In the following, equations (2.26) and (2.27) are approximated with an LBM based on BGK collision [150] and Guo *et al.* forcing [77] (Eq. 2.37 and Table 2.1) on two- and three-dimensional $D2Q9$ and $D3Q27$ lattices (Figures 2.3a, 2.3d).

The equilibrium particle distribution function used by Zhang *et al.* [151] as well as by Höcker *et al.* [60] and Maier [152] is simple, universal for all populations from 0 to 26, and stable for all possible volume fraction values. It is the common, second order truncated Maxwell equilibrium, multiplied with the local volume fraction $\phi^\mathfrak{b}(\boldsymbol{x},t)$ (cf. Equation 2.51).

After the first time step, $\widetilde{\rho^\mathfrak{b}}\phi^\mathfrak{b}$ is replaced by the zeroth population moment $\sum_j f_j$. The standard LBM presupposes the constant density of the fluid, which is typically fulfilled e.g. in multiphase or porous flows. In contrast, if the constant density is multiplied with the spatially and temporally varying volume fraction, the result is not constant anymore. The density in lattice units usually takes the value of 1, whereas the volume fraction can vary between 0 and 1, such that the effective density considered here in turn is varying also between 0 and 1. Taking into account the streaming of effective densities along the lattice directions, the new form of the equilibrium distribution function is then after the first collision

$$f_j^{\mathrm{eq}}(\boldsymbol{x},t) = w_j \left(\int_V \widetilde{\rho^\mathfrak{b}}(\boldsymbol{x},t)\phi^\mathfrak{b}(\boldsymbol{x},t)\mathrm{d}V \right) \left(1 + \frac{\xi_{j\alpha}\overline{u_\alpha^\mathfrak{b}}}{c_\mathrm{s}^2} + \frac{(\xi_{j\alpha}\xi_{j\beta} - c_\mathrm{s}^2\delta_{\alpha\beta})\overline{u_\alpha^\mathfrak{b}u_\beta^\mathfrak{b}}}{2c_\mathrm{s}^4} \right). \tag{A.1}$$

In equation A.1, the first term in brackets is the zeroth moment of the populations which includes both the pressure as density fluctuations and the void fraction through streaming. Two different cases can be distinguished, namely

$$\nabla\phi^\mathfrak{b} < \nabla\widetilde{\rho^\mathfrak{b}} \quad \text{or} \quad \nabla\phi^\mathfrak{b} \geq \nabla\widetilde{\rho^\mathfrak{b}}. \tag{A.2}$$

In the first case ($\nabla\phi^\mathfrak{b} < \nabla\widetilde{\rho^\mathfrak{b}}$) the method of Zhang *et al.* [151] is suitable without any modifications. Thus, the expression

$$\widetilde{\rho^\mathfrak{b}} = \frac{\sum_j f_j}{\phi^\mathfrak{b}(\boldsymbol{x},t)} \tag{A.3}$$

for the effective density is sufficient for second order pressure convergence. In the second case of (A.2) ($\nabla\phi^{\mathrm{b}} \geq \nabla\widetilde{\rho^{\mathrm{b}}}$) the change of void fraction over the cell can not be neglected and hence should be considered by the density moment. Based on that, the new effective density and velocity are defined as

$$\widetilde{\rho^{\mathrm{b}}} = \frac{\sum_j f_j}{\int_V \phi^{\mathrm{b}}(\boldsymbol{x}, t)\mathrm{d}V}, \tag{A.4}$$

$$\overline{\boldsymbol{u}^{\mathrm{b}}} = \frac{\sum_j \boldsymbol{\xi}_j f_j}{\sum_j f_j} + \frac{\triangle t}{2}\frac{\sum_k \overline{\boldsymbol{F}_k}}{\sum_j f_j}, \tag{A.5}$$

respectively. The density definition uses for the volume fraction integration the neighboring cell data, which is considered further below. Due to Guo *et al.* forcing scheme [77], the velocity $\overline{\boldsymbol{u}^{\mathrm{b}}}$ contains the sum of forces used in the example $\sum_k \overline{\boldsymbol{F}_k}$. Further, the forcing term is defined as

$$\Omega_j^F = \left(1 - \frac{\triangle t}{2\tau}\right) w_j \left(\frac{\xi_{j\alpha}}{c_{\mathrm{s}}^2} + \frac{(\xi_{j\alpha}\xi_{j\beta} - c_{\mathrm{s}}^2\delta_{\alpha\beta})\overline{u_\beta^{\mathrm{b}}}}{c_{\mathrm{s}}^4}\right) \sum_k \overline{F_{k\alpha}}. \tag{A.6}$$

The sum $\sum_k \overline{F_{k\alpha}}$ includes the phase interaction forces and the pressure correction force proposed by Zhang *et al.* [151]

$$\overline{\boldsymbol{F}^{\mathrm{P}}} = \widetilde{p}\boldsymbol{\nabla}\phi^{\mathrm{b}} = \widetilde{\rho^{\mathrm{b}}} c_{\mathrm{s}}^2 \boldsymbol{\nabla}\phi^{\mathrm{b}}. \tag{A.7}$$

This correction force adjusts the pressure term in the momentum equation, which is $\boldsymbol{\nabla}(\phi^{\mathrm{b}}\widetilde{p})$ according to the CE expansion of Zhang *et al.* equilibrium particle distribution and should be $\phi^{\mathrm{b}}\boldsymbol{\nabla}\widetilde{p}$ as in VANSE. The phase interaction forces are, for example, in the case of a particle-laden flow given by the drag, lift, gravity, virtual mass, and turbulence interaction forces. These interaction forces are not considered in the present work due to the focus on model validation. Note that the consistent incorporation of the neglected forces can be done with Guo *et al.* forcing scheme alongside the pressure correction. Hence, without loss of generality, it is assumed that $\sum_k \overline{\boldsymbol{F}_k} = \overline{\boldsymbol{F}^{\mathrm{P}}}$. Further, the gradient of volume fraction appearing in (A.7) is discretized through central differences, thus for example in two dimensions

$$\boldsymbol{\nabla}\phi^{\mathrm{b}} \approx \frac{1}{2\triangle x}\begin{pmatrix} \phi_{x+1}^{\mathrm{b}} - \phi_{x-1}^{\mathrm{b}} \\ \phi_{y+1}^{\mathrm{b}} - \phi_{y-1}^{\mathrm{b}} \end{pmatrix}. \tag{A.8}$$

Here, central differences are chosen to match the overall second-order accuracy of the numerical scheme.

The above-mentioned effective density is part of the equilibrium distribution function, and hence propagates from and to the neighbor lattice cells (cf. (2.51) → cf. (A.1)), such that volume fraction becomes integrated over the cell volume $\widetilde{\rho^{\flat}}\phi^{\flat} \rightarrow \widetilde{\rho^{\flat}} \int_V \phi^{\flat}(\boldsymbol{x}, t)\mathrm{d}V$. Each cell contains its own distinct effective density and different density values at the interfaces, calculated by integration with the neighbor cells' effective densities. For the discretized integral calculations, quadrature rules are used:

$$\int_V \phi^{\flat}(\boldsymbol{x}, t)\mathrm{d}V = \sum_j^N \varpi_j(N)\phi^{\flat}(\boldsymbol{x} - \boldsymbol{\xi}_j \triangle t, t), \tag{A.9}$$

which are rearranged to

$$\sum_j^N \varpi_j(N)\phi^{\flat}(\boldsymbol{x} - \boldsymbol{\xi}_j \triangle t, t) = \left(\varpi_{j\neq 0}(N)\boldsymbol{\nabla}^2\phi^{\flat} + \phi^{\flat}\right)(\boldsymbol{x}, t), \tag{A.10}$$

respectively. The number of quadrature points N is dependent on the void fraction variation directions number. Hereby the diagonal directions are not considered. In particular, the volume fraction integration is performed on the $D1Q3$ lattice if the volume fraction changes only in one direction, on the $D2Q5$ lattice if in two and on $D3Q7$ if in all three directions. In (A.9) and (A.10) N is equal to Q. It is to be noted that the weighting factors (ϖ_j), which are listed in Table A.1, do not conform to the weights of a discrete velocity set.

Dimensions	ϖ_0	$\varpi_{j\neq 0}$
$D = 1$	$1/2$	$1/4$
$D = 2$	$1/3$	$1/6$
$D = 3$	$1/6$	$5/36$

Table A.1.: Quadrature weights for void fraction integration over a lattice cell.

For $\triangle x \rightarrow 0$, the term $\nabla^2\phi^{\flat}$ in equation (A.10) nulls out and the integration becomes equal to the local void fraction value, which leads back to the model of Zhang *et al.* [151].

For the second case of (A.2) the equilibrium moments with varying local volume fractions are thus computed via (A.1), (A.4), (A.5), and (A.10) in a separately regarded lattice cell in the pre-collision state to

$$M_0^{\mathrm{eq}} = \sum_j f_j^{\mathrm{eq}} = \widetilde{\rho^{\mathrm{b}}}\left(\phi^{\mathrm{b}}(\boldsymbol{x},t) + \varpi_{j\neq 0}(N)\boldsymbol{\nabla}^2\phi^{\mathrm{b}}\right), \tag{A.11}$$

$$M_{1\alpha}^{\mathrm{eq}} = \sum_j \xi_{j\alpha} f_j^{\mathrm{eq}} = \widetilde{\rho^{\mathrm{b}}}\left(\phi^{\mathrm{b}}(\boldsymbol{x},t) + \varpi_{j\neq 0}(N)\boldsymbol{\nabla}^2\phi^{\mathrm{b}}\right)\overline{\boldsymbol{u}^{\mathrm{b}}}, \tag{A.12}$$

$$\begin{aligned} M_{2\alpha\beta}^{\mathrm{eq}} = \sum_j \xi_{j\alpha}\xi_{j\beta} f_j^{\mathrm{eq}} &= \widetilde{\rho^{\mathrm{b}}}\left(\phi^{\mathrm{b}}(\boldsymbol{x},t) + \varpi_{j\neq 0}(N)\boldsymbol{\nabla}^2\phi^{\mathrm{b}}\right)\overline{u_\alpha^{\mathrm{b}} u_\beta^{\mathrm{b}}} \\ &+ \widetilde{\rho^{\mathrm{b}}} c_s^2\left(\phi^{\mathrm{b}}(\boldsymbol{x},t) + \varpi_{j\neq 0}(N)\boldsymbol{\nabla}^2\phi^{\mathrm{b}}\right), \end{aligned} \tag{A.13}$$

$$M_{3\alpha\beta\gamma}^{\mathrm{eq}} = \sum_j \xi_{j\alpha}\xi_{j\beta}\xi_{j\gamma} f_j^{\mathrm{eq}} = \widetilde{\rho^{\mathrm{b}}}\left(\phi^{\mathrm{b}}(\boldsymbol{x},t) + \varpi_{j\neq 0}(N)\boldsymbol{\nabla}^2\phi^{\mathrm{b}}\right)\overline{\boldsymbol{u}^{\mathrm{b}}}\delta_{\alpha\beta\gamma}. \tag{A.14}$$

Finally, using these moments, a CE expansion (see A.1.3) of the above proposed lattice Boltzmann scheme yields formal consistency towards the VANSE (2.26), (2.27).

A.1.2 Numerical validation of the novel approach

The numerical validation of the proposed LBM for VANSE is performed on a stationary and a transient example. Both examples are built with the method of manufactured solutions (MMS) [153]. Thereby, analytical functions for volume fraction, fluid velocity and pressure are chosen, s.t. they fulfill the mass conservation law of VANSE. For these fixed functions $\phi^{\mathrm{b}}, \overline{\boldsymbol{u}^{\mathrm{b}}}, \widetilde{p_j}$, the MMS force is calculated with central finite differences to

$$\begin{aligned} \boldsymbol{F}^{\mathrm{MMS}} = \partial_t\left(\phi^{\mathrm{b}}\widetilde{\rho^{\mathrm{b}}}\overline{\boldsymbol{u}^{\mathrm{b}}}\right) + \boldsymbol{\nabla}\cdot\left(\phi^{\mathrm{b}}\widetilde{\rho^{\mathrm{b}}}\overline{\boldsymbol{u}^{\mathrm{b}}\boldsymbol{u}^{\mathrm{b}}}\right) + \phi^{\mathrm{b}}\boldsymbol{\nabla}\widetilde{p_j} \\ - \nu\boldsymbol{\nabla}\cdot\left(\phi^{\mathrm{b}}\widetilde{\rho^{\mathrm{b}}}\left(\boldsymbol{\nabla}\overline{\boldsymbol{u}^{\mathrm{b}}} + \overline{\boldsymbol{u}^{\mathrm{b}}}\boldsymbol{\nabla}\right)\right), \end{aligned} \tag{A.15}$$

including all terms of the momentum equation. This force is used as a forcing term in the LBE (2.37) together with the pressure correction force

$$\sum_k \overline{\boldsymbol{F}_k} = \overline{\boldsymbol{F}^{\mathrm{MMS}}} + \overline{\boldsymbol{F}^{\mathrm{P}}}. \tag{A.16}$$

The examples are evaluated through several error measurements. The errors correspond to L^1-, L^2- and L^∞-norms over nodal values of velocity and pressure deviations between the simulated and the prescribed data (Eq. 2.70, 2.71, 2.72).

The solutions of the VANSE are chosen for time-independent and time-dependent cases, constructed similarly to those of Blais *et al.* [154] and Höcker *et al.* [60]. The configurations tested here are summarized as follows.

1. Stationary two-dimensional example:

$$\phi^\flat = 0.5 + 0.4 \sin(\pi x) \sin(\pi y), \tag{A.17}$$

$$\overline{\boldsymbol{u}^\flat} = 2 \begin{pmatrix} -(\sin(\pi x))^2 \sin(\pi y) \cos(\pi y) \\ (\sin(\pi y))^2 \sin(\pi x) \cos(\pi x) \end{pmatrix}, \tag{A.18}$$

$$\widetilde{p^\flat} = \sin(\pi x) \sin(\pi y). \tag{A.19}$$

2. Stationary three-dimensional example:

$$\phi^\flat = 0.5 + 0.4 \sin(\pi x) \sin(\pi y) \sin(\pi z), \tag{A.20}$$

$$\overline{\boldsymbol{u}^\flat} = \begin{pmatrix} (\sin(\pi x))^2 \sin(\pi y) \cos(\pi y) \sin(\pi z) \cos(\pi z) \\ (\sin(\pi y))^2 \sin(\pi x) \cos(\pi x) \sin(\pi z) \cos(\pi z) \\ -2(\sin(\pi z))^2 \sin(\pi x) \cos(\pi x) \sin(\pi y) \cos(\pi y) \end{pmatrix}, \tag{A.21}$$

$$\widetilde{p^\flat} = \sin(\pi x) \sin(\pi y) \sin(\pi z). \tag{A.22}$$

3. Transient one-dimensional example:

$$\phi^\flat = 0.5 + 0.4 \sin(\pi(x - 0.5t)), \tag{A.23}$$

$$\overline{\boldsymbol{u}^\flat} = \begin{pmatrix} 0.5 + \frac{1}{\phi^\flat} \\ 0 \end{pmatrix}, \tag{A.24}$$

$$\widetilde{p^\flat} = \sin(\pi(x - 0.5t)). \tag{A.25}$$

4. Transient two-dimensional example:

$$\phi^\flat = 0.5 + 0.4 \sin(\pi(x - 0.5t)) \sin(\pi(y - 0.5t)), \tag{A.26}$$

$$\overline{\boldsymbol{u}^\flat} = \begin{pmatrix} 0.5 + \frac{1}{\phi^\flat} \\ 0.5 + \frac{1}{\phi^\flat} \end{pmatrix}, \tag{A.27}$$

$$\widetilde{p^\flat} = \sin(\pi(x - 0.5t)) \sin(\pi(y - 0.5t)). \tag{A.28}$$

5. Transient three-dimensional example:

$$\phi^{\flat} = 0.5 + 0.4 \sin\left(\pi(x - 0.5t)\right) \sin\left(\pi(y - 0.5t)\right) \sin\left(\pi(z - 0.5t)\right), \tag{A.29}$$

$$\overline{\boldsymbol{u}^{\flat}} = \begin{pmatrix} 0.5 + \frac{1}{\phi^{\flat}} \\ 0.5 + \frac{1}{\phi^{\flat}} \\ 0.5 + \frac{1}{\phi^{\flat}} \end{pmatrix}, \tag{A.30}$$

$$\widetilde{p^{\flat}} = \sin\left(\pi(x - 0.5t)\right) \sin\left(\pi(y - 0.5t)\right) \sin\left(\pi(z - 0.5t)\right). \tag{A.31}$$

The spatial simulation domain comprises $2\,m$ in each coordinate direction with periodic boundary conditions in every example. The fluid density is set to 1 kg/m^3 and the kinematic viscosity to 0.1 m^2/s. The relaxation time is held constant by all resolutions under diffusive scaling and is equal to 0.53 for the stationary and 0.5075 for the transient examples. Exemplary solutions are visualized in Figure A.1 for the stationary three-dimensional example 2 and in Figure A.2 for the transient three-dimensional example 5.

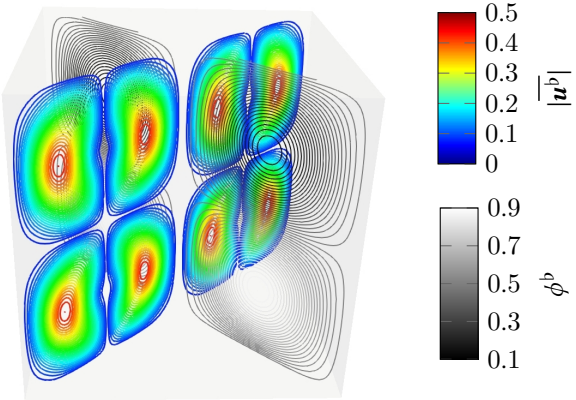

Figure A.1.: Stationary three-dimensional velocity and porosity distribution of Example 2.

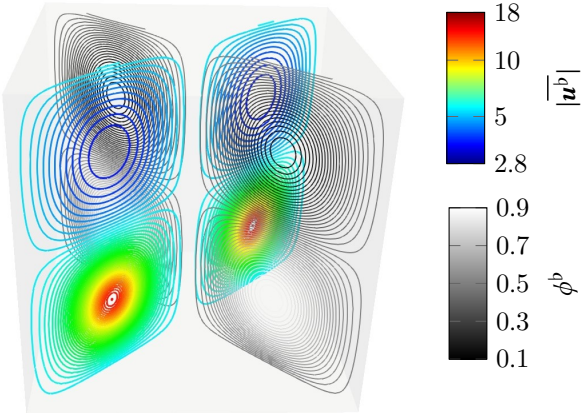

Figure A.2.: Transient three-dimensional velocity and porosity distribution of Example 5.

The convergence plots for the examples in each error norm are shown in Figures A.3, A.4, A.5, A.6, and A.7, respectively.

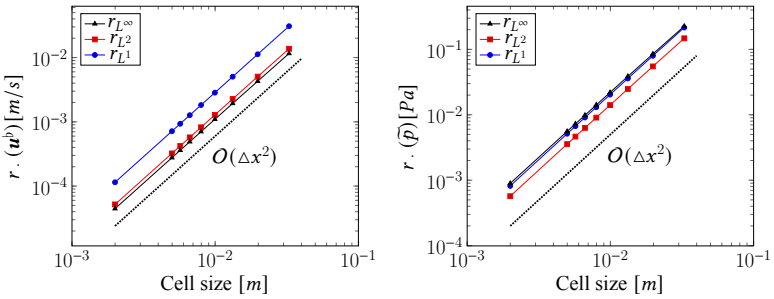

(a) Velocity error (b) Pressure error

Figure A.3.: Error measurements for (a) velocity and (b) pressure of the stationary two-dimensional Example 1.

All examples are evaluated after the state stabilizes and error norms remain asymptotically constant. It is to be noted that also the error norms reach a steady state after sufficiently long simulation time. This is due to the periodic boundary condition and constant maximal and minimal variable values that change only in position but not in amplitude.

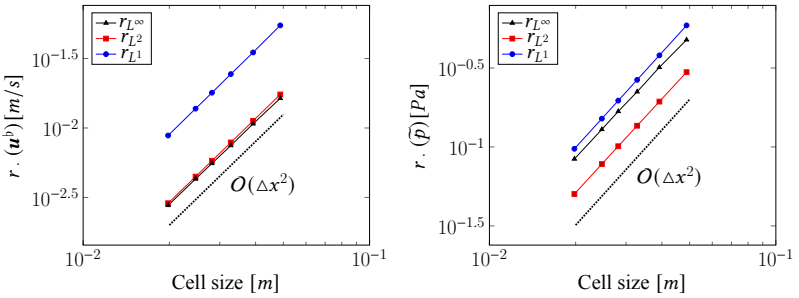

(a) Velocity error (b) Pressure error

Figure A.4.: Error measurements for (a) velocity and (b) pressure of the stationary three-dimensional Example 2.

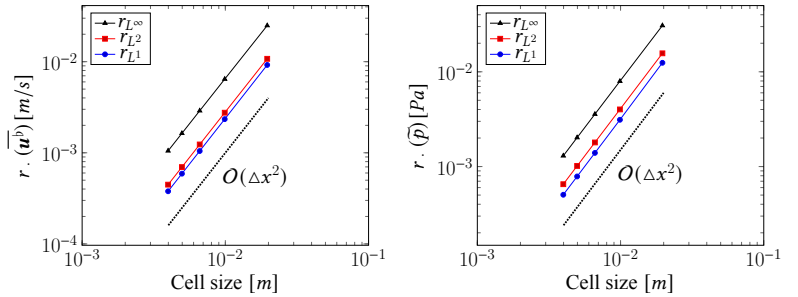

(a) Velocity error (b) Pressure error

Figure A.5.: Error measurements for (a) velocity and (b) pressure of the transient one-dimensional Example 3.

In Figures A.3, A.4, A.5, A.6, and A.7 the same experimental convergence order of two in every norm type for the velocity as well as the pressure error is observed. The absolute pressure deviation is not scaling by an increase of the target pressure values, so that the relative pressure can be made small enough. The results above clarify that the proposed LBM model for approximating VANSE converges with second order and thus is validly consistent in the present numerical tests.

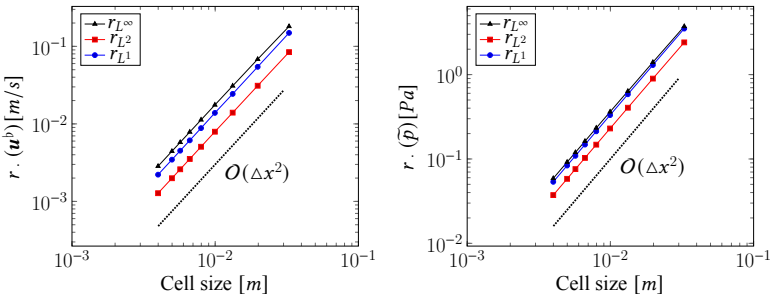

(a) Velocity error (b) Pressure error

Figure A.6.: Error measurements for (a) velocity and (b) pressure of the transient two-dimensional Example 4.

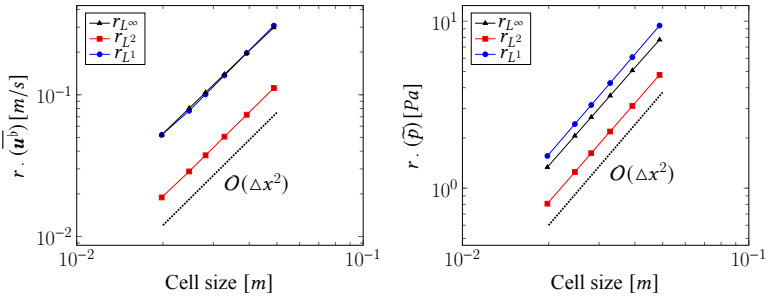

(a) Velocity error (b) Pressure error

Figure A.7.: Error measurements for (a) velocity and (b) pressure of the transient three-dimensional Example 5.

A.1.3 Chapman–Enskog expansion of VANSE-LBM

Below, consistency of the above proposed LBE (2.37) w.r.t. the targeted VANSE (2.26) and (2.27) up to higher order terms is formally proved. The following CE expansion is based on the classical results for the diffusion limit towards the incompressible NSE as summarized for example in [75] and references therein.

Let $\epsilon > 0$ denote a label parameter for the Knudsen number Kn, and all other quantities be defined as above. The expansion ansatz is made

$$\begin{cases} f_j = \sum_{k=0}^{\infty} \epsilon^k f_j^{(k)}, \\ \partial_t = \epsilon \partial_t^{(1)} + \epsilon^2 \partial_t^{(2)}, \\ \boldsymbol{\nabla} = \epsilon \boldsymbol{\nabla}^{(1)}, \\ \Omega_j^F = \epsilon \Omega_j^{F,(1)}. \end{cases} \tag{A.32}$$

Taylor expanding the LBE (2.37) yields

$$\triangle t(\partial_t + \boldsymbol{\xi}_j \cdot \boldsymbol{\nabla}) f_j + \frac{\triangle t^2}{2}(\partial_t + \boldsymbol{\xi}_j \cdot \boldsymbol{\nabla})^2 f_j = -\frac{\triangle t}{\tau} f_j^{\mathrm{neq}} + \triangle t \Omega_j^F + O(\triangle t^3), \tag{A.33}$$

where $\triangle t$ and τ are fixed and $f_j^{\mathrm{neq}} = f_j - f_j^{\mathrm{eq}}$. Subsequent to injecting (A.32), the resulting version of (A.33) can be separated into different ϵ-orders, respectively

$O(\epsilon^0)$:

$$f_j^{(0)} = f_j^{eq}, \tag{A.34}$$

$O(\epsilon^1)$:

$$(\partial_t^{(1)} + \boldsymbol{\xi}_j \cdot \boldsymbol{\nabla}^{(1)}) f_j^{(0)} = -\frac{1}{\tau} f_j^{(1)} + \Omega_j^{F,(1)}, \tag{A.35}$$

$O(\epsilon^2)$:

$$\partial_t^{(2)} f_j^{(0)} + \left(1 - \frac{\triangle t}{2\tau}\right)(\partial_t^{(1)} + \boldsymbol{\xi}_j \cdot \boldsymbol{\nabla}^{(1)})\left(f_j^{(1)} + \frac{\triangle t}{2}\Omega_j^{F,(1)}\right) = -\frac{1}{\tau} f_j^{(2)}. \tag{A.36}$$

Here and in the following, derivative terms of order $k \geq 3$ are neglected due to the smallness argument $\triangle t^k(\partial_t + \boldsymbol{\epsilon}_j \cdot \boldsymbol{\nabla})^k f_j \sim O(\mathrm{Kn}^k)$, as explained in detail in [75].

The pressure forcing term moments, taken in one lattice cell, are

$$M_0^{F,(1)} = \sum_j \Omega_j^{F^{\mathrm{P}}} = 0, \tag{A.37}$$

$$M_{1\alpha}^{F,(1)} = \sum_j \xi_{j\alpha}\Omega_j^{F^{\mathrm{P}}} = \left(1 - \frac{\triangle t}{2\tau}\right)F_{\mathrm{PC},\alpha} = \left(1 - \frac{\triangle t}{2\tau}\right)p\boldsymbol{\nabla}\phi, \tag{A.38}$$

$$M_{2\alpha\beta}^{F,(1)} = \sum_j \xi_{j\alpha}\xi_{j\beta}\Omega_j^{F^{\mathrm{P}}} = \left(1 - \frac{\triangle t}{2\tau}\right)(F_{\mathrm{PC},\alpha}u_\beta + u_\alpha F_{\mathrm{PC},\beta}). \tag{A.39}$$

Note that

$$M_0^{(1)} = -\frac{\triangle t}{2\left(1 - \frac{\triangle t}{2\tau}\right)}M_0^{F,(1)} = 0, \tag{A.40}$$

$$M_{1\alpha}^{(1)} = -\frac{\triangle t}{2\left(1 - \frac{\triangle t}{2\tau}\right)}M_{1\alpha}^{F,(1)} = -\frac{\triangle t}{2}F_{\mathrm{PC},\alpha}, \tag{A.41}$$

and for $k \geq 2$ is assumed

$$M_0^{(k)} = \sum_j f_j^{(k)} = 0 = \sum_j \xi_{j\alpha} f_j^{(k)} = M_{1\alpha}^{(k)}. \tag{A.42}$$

Taking the zeroth, first and second order moments of (A.35) and the zeroth and first ones of (A.36), and substituting the notation of (A.11–A.14) and (A.37–A.39), the following is obtained

$O(\epsilon^1)$:

$$\partial_t^{(1)} M_0^{(0)} + \boldsymbol{\nabla}^{(1)} M_{1\alpha}^{(0)} = 0, \tag{A.43}$$

$$\partial_t^{(1)} M_{1\alpha}^{(0)} + \boldsymbol{\nabla}^{(1)} M_{2\alpha\beta}^{(0)} = -\frac{1}{\tau}M_{1\alpha}^{(1)} + M_{1\alpha}^{F,(1)}, \tag{A.44}$$

$$\partial_t^{(1)} M_{2\alpha\beta}^{(0)} + \boldsymbol{\nabla}^{(1)} M_{3\alpha\beta\gamma}^{(0)} = -\frac{1}{\tau}M_{2\alpha\beta}^{(1)} + M_{2\alpha\beta}^{F,(1)}. \tag{A.45}$$

$O(\epsilon^2)$:

$$\partial_t^{(2)} M_0^{(0)} = 0, \tag{A.46}$$

$$\partial_t^{(2)} M_{1\alpha}^{(0)} + \left(1 - \frac{\triangle t}{2\tau}\right)\boldsymbol{\nabla}^{(1)} M_{2\alpha\beta}^{(1)} = -\frac{\triangle t}{2}\boldsymbol{\nabla}^{(1)}\left(1 - \frac{\triangle t}{2\tau}\right)M_{2\alpha\beta}^{F,(1)}. \tag{A.47}$$

Thus, the recombination (A.43) + (A.46) and (A.44) + (A.47) yields

$$\partial_t M_0^{(0)} + \boldsymbol{\nabla}^{(1)} M_{1\alpha}^{(0)} = 0, \tag{A.48}$$

and

$$\begin{aligned}\partial_t M_{1\alpha}^{(0)} + \boldsymbol{\nabla}^{(1)} M_{2\alpha\beta}^{(0)} + \left(1 - \frac{\triangle t}{2\tau}\right) \boldsymbol{\nabla}^{(1)} M_{2\alpha\beta}^{(1)} \\ = -\frac{1}{\tau} M_{1\alpha}^{(1)} + M_{1\alpha}^{F,(1)} - \frac{\triangle t}{2}\left(1 - \frac{\triangle t}{2\tau}\right) \boldsymbol{\nabla}^{(1)} M_{2\alpha\beta}^{F,(1)},\end{aligned} \tag{A.49}$$

respectively. Under the diffusion limit assumption $\triangle t \sim \triangle x^2 \to 0$ when refining the spatial mesh $\triangle x \to 0$, (A.48) and (A.49) are rewritten as

$$\partial_t M_0^{(0)} + \boldsymbol{\nabla}^{(1)} M_{1\alpha}^{(0)} = 0, \tag{A.50}$$

$$\partial_t M_{1\alpha}^{(0)} + \boldsymbol{\nabla}^{(1)} M_{2\alpha\beta}^{(0)} = -\frac{1}{\tau} M_{1\alpha}^{(1)} + M_{1\alpha}^{F,(1)} - \left(1 - \frac{\triangle t}{2\tau}\right) \boldsymbol{\nabla}^{(1)} M_{2\alpha\beta}^{(1)}. \tag{A.51}$$

The moment notation is substituted to recover

$$\begin{aligned}&\partial_t \left(\widetilde{\rho^{\mathrm{b}}}\left(\phi^{\mathrm{b}}(\boldsymbol{x}, t) + \varpi_{j\neq 0}(N)\boldsymbol{\nabla}^2\phi^{\mathrm{b}}\right)\right) \\ &+ \boldsymbol{\nabla} \cdot \left(\widetilde{\rho^{\mathrm{b}}}\left(\phi^{\mathrm{b}}(\boldsymbol{x}, t) + \varpi_{j\neq 0}(N)\boldsymbol{\nabla}^2\phi^{\mathrm{b}}\right)\overline{\boldsymbol{u}^{\mathrm{b}}}\right) = 0,\end{aligned} \tag{A.52}$$

$$\begin{aligned}&\partial_t \left(\widetilde{\rho^{\mathrm{b}}}\left(\phi^{\mathrm{b}}(\boldsymbol{x}, t) + \varpi_{j\neq 0}(N)\boldsymbol{\nabla}^2\phi^{\mathrm{b}}\right)\overline{\boldsymbol{u}^{\mathrm{b}}}\right) \\ &+ \boldsymbol{\nabla} \cdot \left(\widetilde{\rho^{\mathrm{b}}}\left(\phi^{\mathrm{b}}(\boldsymbol{x}, t) + \varpi_{j\neq 0}(N)\boldsymbol{\nabla}^2\phi^{\mathrm{b}}\right)\overline{\boldsymbol{u}^{\mathrm{b}}\boldsymbol{u}^{\mathrm{b}}}\right) \\ &+ \boldsymbol{\nabla}\left(\widetilde{\rho^{\mathrm{b}}} c_s^2\left(\phi^{\mathrm{b}}(\boldsymbol{x}, t) + \varpi_{j\neq 0}(N)\boldsymbol{\nabla}^2\phi^{\mathrm{b}}\right)\right) = -\left(1 - \frac{\triangle t}{2\tau}\right)\boldsymbol{\nabla} M_{2\alpha\beta}^{(1)} \\ &\quad + \widetilde{\rho^{\mathrm{b}}} c_{\mathrm{s}}^2 \boldsymbol{\nabla}\phi^{\mathrm{b}}.\end{aligned} \tag{A.53}$$

Via reordering (A.45) and deletion of higher-order terms, the following is unfolded

$$M_{2\alpha\beta}^{(1)} = c_{\mathrm{s}}^2 \phi^{\mathrm{b}} \widetilde{\rho^{\mathrm{b}}}(\boldsymbol{\nabla}\overline{\boldsymbol{u}^{\mathrm{b}}} + \overline{\boldsymbol{u}^{\mathrm{b}}}\boldsymbol{\nabla}). \tag{A.54}$$

The derivatives of third order and higher are to be neglected [75]. The terms with $\triangle t$ are also striving for zero by infinite refinement. After the insertion of the stress tensor $\boldsymbol{\nabla} M_{2\alpha\beta}^{(1)}$ the VANSE are recovered up to higher-order terms

$$\partial_t(\phi^{\mathrm{b}}\widetilde{\rho^{\mathrm{b}}}) + \boldsymbol{\nabla} \cdot (\phi^{\mathrm{b}}\widetilde{\rho^{\mathrm{b}}}\overline{\boldsymbol{u}^{\mathrm{b}}}) = 0, \tag{A.55}$$

$$\partial_t(\phi^{\mathrm{b}}\widetilde{\rho^{\mathrm{b}}}\overline{\boldsymbol{u}^{\mathrm{b}}}) + \boldsymbol{\nabla} \cdot (\phi^{\mathrm{b}}\widetilde{\rho^{\mathrm{b}}}\overline{\boldsymbol{u}^{\mathrm{b}}\boldsymbol{u}^{\mathrm{b}}}) + \phi^{\mathrm{b}}\boldsymbol{\nabla}\widetilde{p} = \nu\boldsymbol{\nabla} \cdot (\phi^{\mathrm{b}}\widetilde{\rho^{\mathrm{b}}}(\boldsymbol{\nabla}\overline{\boldsymbol{u}^{\mathrm{b}}} + \overline{\boldsymbol{u}^{\mathrm{b}}}\boldsymbol{\nabla})), \tag{A.56}$$

where the viscosity is regained as

$$\nu = \left(\tau - \frac{\triangle t}{2}\right) c_{\mathrm{s}}^2 \tag{A.57}$$

from comparison to (2.27).

A.2 Applications and tests used in this work

The main principles of *OpenLB* workflow and the main points of setup structure including unit conversion, preparation of geometry, lattice, setting of boundary conditions, and the simulation loop with collision and streaming steps as well as the main evaluation instruments for simulation results are described in the user guide of *OpenLB* [155]. The code given here related to some examples can be found in the release 1.8.1 of *OpenLB* [156] or in the development repository if the commit is provided. The software library is generally implemented using templates and is automatically tested within a continuous integration pipeline.

A.2.1 Macro-level modeling

A.2.1.1 Adsorption on microparticles

The applications for batch adsorption and adsorption in a mixer can be found under *examples/adsorption/*.

The geometries and physical setups with discretization parameters of these applications are described in Chapter 3. These setups include the following lattices:

1. sLattice with D3Q19 for *NSE* (if needed),
2. sLatticeAD with D3Q7 for adsorbent particles transport *ADE*,
3. CADLattice with D3Q7 for solute concentration *ADE*,
4. QADLattice with D3Q7 for adsorbate loading *ADE*.

The AdsorptionFullCoupling3D sets velocities and reaction rates on the ADE lattices.

```
1  // coupling struct
2  template <typename ADSORPTION_REACTION, typename FORCE>
3  struct AdsorptionFullCoupling3D {
4    using reaction_t = ADSORPTION_REACTION;
5    static constexpr OperatorScope scope = OperatorScope::
       PerCellWithParameters;
6
7    // Combine the parameters of ADSORPTION_REACTION and FORCE
```

```
8   using parameters = meta::merge<typename ADSORPTION_REACTION::
9                                  parameters, typename FORCE::parameters>;
10
11  template <typename CELLS, typename PARAMETERS>
12  void apply(CELLS& cells, PARAMETERS& parameters) any_platform
13  {
14    using V = typename CELLS::template value_t<names::Concentration0>::
       value_t;
15    using DESCRIPTOR = typename CELLS::template value_t<names::
       Concentration0>::descriptor_t;
16
17    auto& cellNS = cells.template get<names::NavierStokes>();
18    auto& cellParticle = cells.template get<names::Concentration0>();
19    auto& cellSolute = cells.template get<names::Concentration1>();
20    auto& cellLoading = cells.template get<names::Concentration2>();
21
22    // computation of particle velocity for particle and load lattices
23    V velocity[3], velocityRight[3], velocityLeft[3], velocityUp[3],
       velocityDown[3], velocityFront[3], velocityBack[3] {V(0)};
24    cellNS.computeU(velocity);
25    // x-velocities
26    cellNS.neighbor({1,0,0}).computeU(velocityRight);
27    cellNS.neighbor({-1,0,0}).computeU(velocityLeft);
28    // y-velocities
29    cellNS.neighbor({0,1,0}).computeU(velocityUp);
30    cellNS.neighbor({0,-1,0}).computeU(velocityDown);
31    // z-velocities
32    cellNS.neighbor({0,0,1}).computeU(velocityFront);
33    cellNS.neighbor({0,0,-1}).computeU(velocityBack);
34    // velocity gradients
35    V velocityGrad[3] = {0., 0., 0.};
36    velocityGrad[0] =
37        0.5*( velocity[0]*(velocityRight[0] - velocityLeft[0])
38        + velocity[1]*(velocityUp[0] - velocityDown[0])
39        + velocity[2]*(velocityFront[0] - velocityBack[0]) );
40    velocityGrad[1] =
41        0.5*( velocity[0]*(velocityRight[1] - velocityLeft[1])
42        + velocity[1]*(velocityUp[1] - velocityDown[1])
43        + velocity[2]*(velocityFront[1] - velocityBack[1]) );
44    velocityGrad[2] =
45        0.5*( velocity[0]*(velocityRight[2] - velocityLeft[2])
46        + velocity[1]*(velocityUp[2] - velocityDown[2])
47        + velocity[2]*(velocityFront[2] - velocityBack[2]) );
48
49    V forceValue[3] = {0.,0.,0.};
50
51    FORCE().applyForce(forceValue,cells,velocity,parameters);
52
53    // compute new particle velocity under action of forces
54    V newVel[3];
55    for (int i=0; i < DESCRIPTOR::d; i++) {
```

```
56        newVel[i] = velocity[i] + forceValue[i] - velocityGrad[i];
57      }
58      cellParticle.template setField<descriptors::VELOCITY>(newVel);
59      cellLoading.template setField<descriptors::VELOCITY>(newVel);
60
61      //setting of the solute velocity to the carrier fluid velocity
62      cellSolute.template setField<descriptors::VELOCITY>(velocity);
63
64      //computation of the adsorption source terms for solute and load
         lattices
65      V soluteConcentration = cellSolute.computeRho();
66      V particleConcentration = cellParticle.computeRho();
67      V particleLoading = cellLoading.computeRho();
68
69      Vector<V, 2> reactionRates = ADSORPTION_REACTION().getReactionRate(
         soluteConcentration, particleLoading, particleConcentration,
         parameters);
70      cellLoading.template setField<descriptors::SOURCE>(reactionRates[1]);
71      cellSolute.template setField<descriptors::SOURCE>(-reactionRates[0]);
72      }
73  };
```

The reaction rates are calculated as:

```
1   template <typename V, typename PARAMETERS>
2   Vector<V, 2> getReactionRate(V soluteConcentration,
3                                V particleLoading,
4                                V particleConcentration,
5                                PARAMETERS& params) any_platform{
6       V surfaceLoad;
7       V conversionFactorDensity = params.template get<CONV_DENS>();
8       V conversionFactorParticleDensity = params.template get<
         CONV_PARC_DENS>();
9       particleConcentration *= conversionFactorParticleDensity; //convert
         to kg/m^3
10      soluteConcentration *= conversionFactorDensity; //convert to g/m^3
11      particleLoading *= conversionFactorParticleDensity; //convert to g/m
         ^3
12      auto externalMassTransferEnabled = params.template get<EXT_MASS>();
13      if (externalMassTransferEnabled) {
14        surfaceLoad = getSurfaceLoading(soluteConcentration,
         particleLoading, particleConcentration, params);
15      } else {
16        surfaceLoad = getSurfaceLoading(soluteConcentration,params);
17      }
18      V D_s = params.template get<D_S>();
19      V r_p = params.template get<R_P>();
20      V k_s = params.template get<K_S>();
21
22      V reactionRate = k_s * (surfaceLoad * particleConcentration -
         particleLoading);
```

```
23     Vector<V, 2> reactionRates(
24         reactionRate / conversionFactorDensity, // solute
25         reactionRate / conversionFactorParticleDensity ); // loading
26
27     return reactionRates;
28 }
```

The getSurfaceLoading includes different mass transfer mechanisms from bulk using distinct diffusion coefficients. Also, an isotherm type should be chosen in the setup (linear, Langmuir, or Freundlich).

A.2.2 Micro-level modeling

A.2.2.1 Laminar reactive T-micromixer

This application is in *examples/advectionDiffusionReaction/laminarReactiveT-mixer/*.

The geometry and physical setup with discretization parameters of the micromixer are described in the Section 4.2. From the code point of view, four lattices are considered:

- sLatticeNS with D3Q19 descriptor for *NSE*,
- CRADlattice 1 with D3Q7 descriptor for *ADE* of specie *A*,
- CRADlattice 2 with D3Q7 descriptor for *ADE* of specie *B*,
- CRADlattice 3 with D3Q7 descriptor for *ADE* of specie *C*.

By *NSE*, the fixed velocity InterpolatedVelocity boundary is set on the two inlets, at the outlet the InterpolatedPressure boundary is defined. BounceBack for no-slip condition is used at the walls. RectanglePoiseuille3D functor at the inlets in the setBoundaryValues section approximates the inflow Poiseuille velocity profile. Thereby, the sinus start ramp for velocity from zero to the needed value is used. As collision operator BGKdynamics is chosen for this lattice.

By all *ADE*s, AdvectionDiffusionDirichlet boundaries are applied to the inlets and the setZeroGradientBoundary is set at the outlet. Depending on the species, different values are defined at the inlets. BounceBack is used at the walls as

well. SourcedLimitedAdvectionDiffusionBGKdynamics with locally taken relaxation frequencies is used as a collision operator. This dynamics considers the reaction term per cell and ensures that the species concentrations do not become negative.

For reaction terms calculation (stochCoeff[0]*source) and stabilization of *ADE*s – computation of local "turbulent" relaxation times tau_turb_AD0, the LESReactionCoupling is applied per cell in each time step. Thereby, *Smagorinsky approach* is taken for calculation of "turbulent" relaxation times of the *NSE* lattice and then they are transformed to the stabilization *ADE* relaxation times using chosen *stabilization Schmidt numbers*.

```
1  template<typename T, int numComp>
2  struct LESReactionCoupling {
3  static constexpr OperatorScope scope = OperatorScope::
       PerCellWithParameters;
4
5  struct LATTICE_REACTION_COEFF : public descriptors::FIELD_BASE<1> { };
6  struct STOCH_COEFF : public descriptors::FIELD_BASE<numComp> { };
7  struct REACTION_ORDER : public descriptors::FIELD_BASE<numComp> { };
8  struct SMAGORINSKY_PREFACTOR : public descriptors::FIELD_BASE<1> { };
9  struct SCHMIDT : descriptors::FIELD_BASE<numComp> { };
10 struct OMEGA_NSE : public descriptors::FIELD_BASE<1> { };
11 struct OMEGAS_ADE : public descriptors::FIELD_BASE<numComp> { };
12
13 using parameters = meta::list<LATTICE_REACTION_COEFF, STOCH_COEFF,
       REACTION_ORDER, SMAGORINSKY_PREFACTOR, SCHMIDT, OMEGA_NSE,
       OMEGAS_ADE>;
14
15 template <typename CELLS, typename PARAMETERS>
16 void apply(CELLS& cells, PARAMETERS& parameters) any_platform
17  {
18   using DESCRIPTOR = typename CELLS::template value_t<names::
       NavierStokes>::descriptor_t;
19   using DESCRIPTOR_ADE = typename CELLS::template value_t<names::
       Concentration0>::descriptor_t;
20   // Velocity coupling
21   auto u = cells.template get<names::Concentration0>().template
       getField<descriptors::VELOCITY>();
22   T rho, pi[util::TensorVal<DESCRIPTOR>::n] { };
23   cells.template get<names::NavierStokes>().computeAllMomenta(rho, u.
       data(), pi);
24   cells.template get<names::Concentration0>().template setField<
       descriptors::VELOCITY>(u);
25   cells.template get<names::Concentration1>().template setField<
       descriptors::VELOCITY>(u);
26   cells.template get<names::Concentration2>().template setField<
       descriptors::VELOCITY>(u);
27   // Stress tensor
28   T PiNeqNormSqr = pi[0]*pi[0] + 2.0*pi[1]*pi[1] + pi[2]*pi[2];
```

```
29      if constexpr (util::TensorVal<DESCRIPTOR>::n == 6) {
30        PiNeqNormSqr += pi[2]*pi[2] + pi[3]*pi[3] + 2*pi[4]*pi[4] +pi[5]*pi
          [5];
31      }
32      T PiNeqNorm     = util::sqrt(PiNeqNormSqr);
33      // Molecular realaxation time
34      T tau_mol_NS = T{1} / parameters.template get<OMEGA_NSE>();
35      auto omegasAD = parameters.template get<OMEGAS_ADE>();
36      T tau_mol_AD0 = T{1} / omegasAD[0];
37      ...
38      // Turbulent realaxation time
39      T smagoPrefactor = parameters.template get<SMAGORINSKY_PREFACTOR>();
40      T tau_turb_NS = T{0.5}*(util::sqrt(tau_mol_NS*tau_mol_NS +
          smagoPrefactor/rho*PiNeqNorm) - tau_mol_NS);
41      // Schmidt number stabilization
42      auto Sc = parameters.template get<SCHMIDT>();
43      T tauTurbADPrefactor0 = descriptors::invCs2<T,DESCRIPTOR_ADE>() /
          descriptors::invCs2<T,DESCRIPTOR>() / Sc[0];
44      ...
45      T tau_turb_AD0 = tau_turb_NS * tauTurbADPrefactor0;
46      ...
47      cells.template get<names::Concentration0>().template setField<
          descriptors::OMEGA>(T{1} / (tau_mol_AD0 + tau_turb_AD0));
48      ...
49      // reaction terms calculation
50      auto stochCoeff = parameters.template get<STOCH_COEFF>();
51      auto reactionOrder = parameters.template get<REACTION_ORDER>();
52      T source = parameters.template get<LATTICE_REACTION_COEFF>();
53      {
54        T conc = cells.template get<names::Concentration0>().computeRho();
55        source *= util::pow(conc, reactionOrder[0]);
56      }
57      ...
58      {
59        cells.template get<names::Concentration0>().template setField<
          descriptors::SOURCE>(stochCoeff[0]*source);
60        ...
61      }
62    }
63  };
```

By evaluations of simulation results in the getResultsNS and getResultsCRAD sections, the carrier fluid velocity, pressure, instantaneous and time-averaged concentration, as well as local diffusion values are written out, including plots of concentrations and diffusivities along the T-mixer central axis.

A.2.2.2 Turbulent micromixer with confined impinging jets

This application can be found under *apps/fedor_bukreev/turbulentMixerGPU*. The geometry and physical setup with discretization parameters of the turbulent micromixer are described in Section 4.3.

In this feasibility study, only two lattices are considered: one for *NSE* and one for *ADE*. The boundary conditions are the same as in the laminar micromixer, except for the type of velocity distribution at the inlets. They are now circular and turbulent, which is why CirclePowerLaw3D has a power law velocity profile with a power of 8. Additionally, the vortex method is used for turbulence initialization:

```
1     VortexMethodTurbulentVelocityBoundary<T,NSDESCRIPTOR> vortex3(
2     superGeometry.getMaterialIndicator(3), // material number of inlet (
       see user guide)
3     layerInflowL,                          // inlet plane
4     converter,                             // unit converter (see user
       guide)
5     sLatticeNS,                            // lattice of vortex method
       application
6     500,                                   // N vortexes on inlet plane
7     100,                                   // N time steps till change of
        vortex rotation sense
8     converter.getCharPhysLength()*0.1,     // size of turbent vortexes
9     turbIntensity,                         // turbulence intensity
10    inflowAxis3);                          // direction of inflow
```

For *NSE* lattice, the SmagorinskyBGKdynamics is used that combines BGK collision with the Smagorinsky LES approach.

```
1  /// Smagorinsky BGK collision step
2  template<typename T, typename DESCRIPTOR, typename MOMENTA=momenta::
       BulkTuple>
3  using SmagorinskyBGKdynamics = dynamics::Tuple<
4    T, DESCRIPTOR,
5    MOMENTA,
6    equilibria::SecondOrder,
7    collision::SmagorinskyEffectiveOmega<collision::BGK>
8  >;
9
10 /// Smagorinsky turbulent viscosity -> relaxation frequency OMEGA
11 template <typename COLLISION, typename DESCRIPTOR, typename MOMENTA,
       typename EQUILIBRIUM>
12 struct SmagorinskyEffectiveOmega {
13   using MomentaF = typename MOMENTA::template type<DESCRIPTOR>;
```

```
14    using CollisionO = typename COLLISION::template type<DESCRIPTOR,
          MOMENTA, EQUILIBRIUM>;
15
16    template <concepts::Cell CELL, concepts::Parameters PARAMETERS,
          typename V=typename CELL::value_t>
17    V computeEffectiveOmega(CELL& cell, PARAMETERS& parameters)
          any_platform {
18      V piNeqNormSqr { };
19      MomentaF().computePiNeqNormSqr(cell, piNeqNormSqr);
20      const V rho = MomentaF().computeRho(cell);
21      const V omega = parameters.template get<descriptors::OMEGA>();
22      const V smagorinsky = parameters.template get<collision::LES::
          SMAGORINSKY>();
23      V piNeqNorm = util::sqrt(piNeqNormSqr);
24      V preFactor = smagorinsky*smagorinsky
25                    * descriptors::invCs2<V,DESCRIPTOR>()*descriptors::invCs2
          <V,DESCRIPTOR>()
26                    * 2 * util::sqrt(2);
27      /// Molecular realaxation time
28      V tauMol = V{1} / omega;
29      /// Turbulent realaxation time
30      V tauTurb = V{0.5} * (util::sqrt(tauMol*tauMol + preFactor / rho *
          piNeqNorm) - tauMol);
31      /// Effective realaxation time
32      V tauEff = tauMol + tauTurb;
33      return  V{1} / tauEff;
34    }
35
36    template <concepts::Cell CELL, concepts::Parameters PARAMETERS,
          typename V=typename CELL::value_t>
37    CellStatistic<V> apply(CELL& cell, PARAMETERS& parameters) any_platform
          {
38      parameters.template set<descriptors::OMEGA>(
39        computeEffectiveOmega(cell, parameters));
40      return CollisionO().apply(cell, parameters);
41    }
42  };
```

A similar lattice coupler is used in this case without calculation of reaction terms, only *ADE stabilization* is applied. For evaluation, only instantaneous velocity and ADE scalar distribution are visualized.

A.2.3 Nano-level modeling

A.2.3.1 Poisson equation

This application can be found in *examples/pdeSolverEoc/poisson/*.

The mathematical description of this application is given in Section 5.1.3.1. The *PE* is solved with SourcedAdvectionDiffusionBGKdynamics. This example has periodic boundary conditions in Y and Z directions, whereby in X direction the AdvectionDiffusionDirichlet boundary condition is taken. The needed source term is computed using struct ComputeSourceTerm:

```
// Updating of source term in each time step in each cell
struct ComputeSourceTerm {
  static constexpr OperatorScope scope = OperatorScope::
    PerCellWithParameters;

  // time step unit conversion factor
  struct C_T : public descriptors::FIELD_BASE<1> { };
  // chosen k constant
  struct CONSTK : public descriptors::FIELD_BASE<1> { };

  using parameters = meta::list<C_T,CONSTK>;

  int getPriority() const {
    return 0;
  }

  template <typename CELL, typename PARAMETERS>
  void apply(CELL& cell, PARAMETERS& parameters) any_platform {
    using V = typename CELL::value_t;
    V psi = cell.computeRho();
    V k = parameters.template get<CONSTK>();
    V source = -k*k*psi*parameters.template get<C_T>();
    cell.template setField<descriptors::SOURCE>(source);
  }
};
```

The VELOCITY field is set to 0. The simulation runs until convergence of the average ψ value in the calculation domain with a convergence criterion of 10^{-9}.

A.2.3.2 Poisson-Nernst-Planck equation system

This application is in *examples/electroChemistry/poissonNernstPlanck/*.

The mathematical and physical description of this application is given in the Section 5.1.3.2. The app considers three lattices: one for *PE*, one for cation *NPE* and one for anion *NPE*, all of them are of D3Q19, which is more precise for the calculation of electric potential gradients. The ion dynamics is represented with AdvectionDiffusionBGKdynamics. In this application, variables change only in the Y direction, which is why X and Z directions are set to periodicity. In the Y direction, the *PE* lattice gets AdvectionDiffsionDirichlet boundary conditions at both edges. The ion lattices get the same boundary condition at the bulk side and BounceBack at the wall side.

The *PE* can be simulated in the form of an internal loop until convergence in each Nernst-Planck time step, or it can do only one collision per global time step due to the steadiness of the given example. The calculation of potential gradients, ions' velocities, and Poisson equation source term happens in the PNPCoupling.

```
1  // Poisson-Nernst-Planck coupling
2  template<typename T>
3  struct PNPCoupling {
4    static constexpr OperatorScope scope = OperatorScope::
       PerCellWithParameters;
5
6    ...
7
8    template <typename CELLS, typename PARAMETERS>
9    void apply(CELLS& cells, PARAMETERS& parameters) any_platform
10    {
11     T dX = parameters.template get<DX>();
12     T velCoeff = parameters.template get<NPVELCOEFF>();
13     T poissonCoeff = parameters.template get<POISSONCOEFF>();
14     T omega = parameters.template get<OMEGA>();
15     using DESCRIPTOR = typename CELLS::template value_t<names::
         Concentration0>::descriptor_t;
16
17     auto& cellNP = cells.template get<names::Concentration0>();
18     auto& cellP = cells.template get<names::Concentration1>();
19     auto& cellNP2 = cells.template get<names::Concentration2>();
20
21     T dxPsi[3] = {0.};
22
23     for(int iPop = 0; iPop < DESCRIPTOR::q; iPop++){
```

```
24        dxPsi[0] += descriptors::c<DESCRIPTOR>(iPop, 0) * cellP[iPop];
25        dxPsi[1] += descriptors::c<DESCRIPTOR>(iPop, 1) * cellP[iPop];
26        dxPsi[2] += descriptors::c<DESCRIPTOR>(iPop, 2) * cellP[iPop];
27      }
28
29      dxPsi[0] *= (-1.*omega*descriptors::invCs2<T,DESCRIPTOR>()/dX);
30      ...
31
32      T vel[3] ={0.};
33      vel[0] -= velCoeff * dxPsi[0];
34      ...
35      cellNP.template setField<descriptors::VELOCITY>(vel);
36
37      T vel2[3] ={0.};
38      vel2[0] += velCoeff * dxPsi[0];
39      ...
40      cellNP2.template setField<descriptors::VELOCITY>(vel2);
41
42      T concentration = cellNP.computeRho();
43      if(util::abs(concentration) > 1.){ concentration = 0.; }
44      T concentration2 = cellNP2.computeRho();
45      if(util::abs(concentration2) > 1.){ concentration2 = 0.; }
46      T poissonSource = poissonCoeff * (concentration - concentration2);
47      cellP.template setField<descriptors::SOURCE>(poissonSource);
48    }
49  };
```

A.2.3.3 Navier-Stokes-Poisson-Nernst-Planck equation system

This application is in *examples/electroChemistry/electroosmosis/*.

The mathematical and physical description of this application is given in the Section 5.1.3.3. The code of the application is based on the previous one; it is extended with *NSE* D3Q19 lattice. This lattice is operated with ForcedBGKdynamics. At the wall thereby, the BounceBack boundary condition is defined. At the bulk borders, the setZeroGradient is chosen. The coupler is extended by:

```
1     auto force = cellNSE.template getField<descriptors::FORCE>();
2     force = {0.,0.,0.};
3     force[0] = forceCoeff * (concentration - concentration2);
4     cellNSE.template setField<descriptors::FORCE>(force);
```

The forceCoeff is defined as:

```
1    T forceCoeff = eField * Faraday * valence/density * converterNSE.
      getConversionFactorMass() / converterNSE.getConversionFactorForce();
```

A.2.3.4 Forward AD implementation example

In *OpenLB*, forward AD is then implemented via C++ operator overloading by a data type ADf<double,D> which stores for any quantity X its value as well as its sensitivities with respect to the controls. The collision operators in *OpenLB* are mostly fully differentiable, which allows the application of the forward AD to all the dynamics. Functioning of AD is verified by the implemented unit tests. For example, the overloading multiplication operator for variables of type ADf<double,n> looks like

```
1 template <class T, unsigned D>
2 inline constexpr ADf<T,D>& ADf<T,D>::operator *= (const ADf<T,D>& Y) {
3   // _v stores the value, _d stores the derivative vector
4   _d = _d*Y._v+_v*Y._d;
5   _v *= Y._v;
6   return *this;
7 }
```

Therefore, the data type used for floating-point variables in the entire code base is employed as a template parameter. This allows compilation runs of the same function with both IEEE double precision (for primal simulation) and ADf<double,D> (for derivative computation) type variables. The result is a generic method, which reuses the same setup for both the primal simulation and the sensitivity analysis.

A.2.3.5 Applications used for OCP crystallization

Commit: *OCP crystallization*

Section 5.2.1.1	*apps/fedor_bukreev/Poisson/crystalSimulationAD*
	apps/fedor_bukreev/Poisson/crystalSimulationV2
Section 5.2.2	*apps/fedor_bukreev/Poisson/crystalSimulationOnRockAD*
	apps/fedor_bukreev/Poisson/crystalSimulationOnRockA

Table A.2.: Application used for [37].

The listed here applications are based on the code described in the Section A.2.3.3. The lattice coupler is extended with identification of boundary cells and the calculation of saturation products and surface reaction kinetics in these cells.

A.2.4 VANSE LBM

Commit: *VANSE LBM*

Stationary 2D example	*apps/fedor_bukreev/VANS/testFlowVANS2D*
Stationary 3D example	*apps/fedor_bukreev/VANS/testFlowVANS3D*
Transient 1D example	*apps/fedor_bukreev/VANS/testFlowVANS1D*
Transient 2D example	*apps/fedor_bukreev/VANS/testFlowVANS2D*
Transient 3D example	*apps/fedor_bukreev/VANS/testFlowVANS3D*

Table A.3.: Application used for [62].

A.3 Publications, conference talks, software releases

The publications, conference talks, and software releases listed here are related to the current thesis or some aspects of them can be used for further steps in the optimization of the crystallization reactor.

Peer-reviewed articles

1. **Bukreev, F.**, Kummerländer, A., Jeßberger, J., Teutscher, D., Ito, S., Simonis, S., Dapelo, D., Nezhad, M. M., Nirschl, H., Krause, M. J. (2025). A Hybrid Lattice-Boltzmann Model for Hydro-Electrochemical Modeling and Sensitivity Analysis of Crystallization Potential in Nanoporous Media. Part I: Simulation Model. Engineering with Computers, 2025, ISSN: 1435-5663. https://doi.org/10.1007/s00366-025-02216-x

2. **Bukreev, F.**, Kummerländer, A., Jeßberger, J., Teutscher, D., Ito, S., Simonis, S., Dapelo, D., Nezhad, M. M., Nirschl, H., Krause, M. J. (2025). A Hybrid Lattice-Boltzmann Model for Hydro-Electrochemical Modeling and Sensitivity Analysis of Crystallization Potential in Nanoporous Media. Part II: Application to the Identification and Quantification of Influencing Factors of Phosphate Saturation. Engineering with Computers, 2025, ISSN: 1435-5663. https://doi.org/10.1007/s00366-025-02217-w

3. **Bukreev, F.**, Kummerländer, A., Jeßberger, J., Teutscher, D., Simonis, S., Bothe, D., Krause, M. J. (2025). Benchmark Simulation of Laminar Reactive Micromixing Using Lattice Boltzmann Methods. *AIAA Journal*, 63:4, 1295-1304. https://doi.org/10.2514/1.J064234

4. **Bukreev, F.**, Raichle, F., Nirschl, H., Krause, M. J. (2023). Simulation of adsorption processes on moving particles based on an Euler-Euler description using a lattice Boltzmann discretization. *Chemical Engineering Science*, 270, 118485. https://doi.org/10.1016/j.ces.2023.118485

5. **Bukreev, F.**, Simonis, S., Kummerländer, A., Jeßberger, J., Krause, M. J. (2023). Consistent lattice Boltzmann methods for the volume averaged Navier–Stokes equations. *Journal of Computational Physics*, 489, 112301. https://doi.org/10.1016/j.jcp.2023.112301

6. Teutscher, D., **Bukreev, F.**, Kummerländer, A., Simonis, S., Bächler, P., Rezaee, A., Hermansdorfer, M., Krause, M. J. (2025). A digital urban twin enabling interactive pollution predictions and enhanced planning. *Building and Environment*, 281, 113093. https://doi.org/10.1016/j.buildenv.2025.113093

7. Kummerländer, A., **Bukreev, F.**, Teutscher, D., Dorn, M., Krause, M. J. (2024). Optimization of single node load balancing for lattice Boltzmann methods on heterogeneous high performance computers. *Journal of Parallel and Distributed Computing*, vol. 206, p. 105-169, 2025, issn: 0743-7315.https://doi.org/10.1016/j.jpdc.2025.105169

8. Hettel, M., **Bukreev, F.**, Daymo, E., Kummerländer, A., Krause, M. J., Deutschmann, O. (2025). Calculation of single and multiple low Reynolds number free jets with a lattice-Boltzmann method. *AIAA Journal*, 63(4), 1305–1318. https://doi.org/10.2514/1.J064280

9. Kummerländer, A., **Bukreev, F.**, Berg, S.F.R., Dorn, M., Krause, M.J. (2024). Advances in Computational Process Engineering using Lattice Boltzmann Methods on High Performance Computers. In: *Nagel, W.E., Kröner, D.H., Resch, M.M. (eds) High Performance Computing in Science and Engineering '22*. HPCSE 2022. Springer, Cham. https://doi.org/10.1007/978-3-031-46870-4_16

10. Ito, S., Großmann, S., **Bukreev, F.**, Jeßberger, J., Krause, M. J. (2025). Benchmark case for the inverse determination of adsorption parameters using lattice Boltzmann methods and gradient-based optimization. *Chemical Engineering Science*, 309, 121467. https://doi.org/10.1016/j.ces.2025.121467

11. Teutscher, D., Kummerländer, A., **Bukreev, F.**, Dorn, M., Krause, M. J. (2024). Just-in-Time Fluid Flow Simulation on Mobile Devices Using OpenVisFlow and OpenLB. *Applied Sciences*, 14(5), 1784. https://doi.org/10.3390/app14051784

12. Ito, S., Jeßberger, J., Simonis, S., **Bukreev, F.**, Kummerländer, A., Zimmermann, A., Thäter, G., Pesch, G. R., Thöming, J., Krause, M. J. (2024). Identification of reaction rate parameters from uncertain spatially distributed concentration data using gradient-based PDE constrained optimization. *Computers & Mathematics with Applications*, 167, 249–263. https://doi.org/10.1016/j.camwa.2024.05.026

13. Jeßberger, J., Marquardt, J. E., Heim, L., Mangold, J., **Bukreev, F.**, Krause, M. J. (2022). Optimization of a Micromixer with Automatic Differentiation. Fluids, 7(5), 144. https://doi.org/10.3390/fluids7050144

Preprints and publication in review

14. Dapelo, D.*, **Bukreev, F.***, Krause, M. J., Bridgeman, J. (2025). Lattice-Boltzmann methods for dispersed, mixed and transitional fluid flows: a review of current approaches towards a general multiphase/multicomponent Eulerian model. *Submitted to Archives of Computational Methods in Engineering*
(*)The authors share first authorship.

15. **Bukreev, F.**, Berg, S. F. R., Faeghi, S., Kummerländer, A., Krause, M. J. (2024). Prediction of aerosol distributions in turbulent flow regimes with a sub-grid scale particle lattice Boltzmann method. *SSRN*. https://doi.org/10.2139/ssrn.4991224

16. Kummerländer, A., **Bukreev, F.**, Shimojima, Y., Ito, S., Krause, M. J. (2025). Large-scale simulations of turbulent flows using lattice Boltzmann methods on heterogeneous high performance computers. *arXiv*. https://arxiv.org/abs/2506.21804

17. Selmi, A., Krause, M. J., **Bukreev, F.**, Nagel, C. (2025). A lattice Boltzmann approach for thermal microflows. *SSRN*. https://doi.org/10.2139/ssrn.5201331

18. Ito, S., Zimmermann, A., Jeßberger, J., Simonis, S., Kummerländer, A., **Bukreev, F.**, Thöming, J., Pesch, G., Krause, M.J. (2025) Geometry Reconstruction from Magnetic Resonance Velocimetry Measurements via Solving an Inverse Fluid Flow Problem *SSRN*. https://ssrn.com/abstract=5313346

Conference talks

1. **Bukreev, F.**, Kummerländer, A., Ito, S., Krause, M. J. (2025). Efficient wall-modelled large eddy simulation for fluid-structure interaction using homogenized hybrid recursive regularized Lattice-Boltzmann methods. In *15th European Aerospace Science Network (EASN) Conference*, Madrid, Spain.
2. **Bukreev, F.**, Kummerländer, A., Ito, S., Krause, M. J. (2025). Efficient Wall-Modelled Large Eddy Simulation (WMLES) with Fluid-Structure Interaction (FSI) using Hybrid Homogenized Regularized Recursive Lattice-Boltzmann Methods (HHRRLBM). In *23rd Computational Fluids Conference*, Santiago de Chile, Chile.
3. **Bukreev, F.**, Teutscher, D., Kummerländer, A., Nirschl, H., Krause, M. J. (2024). Simulation of Crystallization Reaction on Nano-scale Using Lattice Boltzmann Methods. In *The 33rd Discrete Simulation of Fluid Dynamics (DSFD) conference*, Zürich, Switzerland.
4. **Bukreev, F.**, Kummerländer, A., Jeßberger, J., Teutscher, D., Bothe, D., Krause, M. J. (2024). Hydrodynamic Modeling and Simulation of Crystallization Reactions at Nano-scales with Parallel Sensitivity Analysis. In *9th European Congress on Computational Methods in Applied Sciences and Engineering*, Lisbon, Portugal.
5. **Bukreev, F.**, Kummerländer, A., Jeßberger, J., Teutscher, D., Bothe, D., Krause, M. J. (2023). Lattice Boltzmann Simulation of a Reacting Micro-mixer. In *22nd Computational Fluids Conference*, Cannes, France.
6. **Bukreev, F.**, Nirschl, H., Krause, M. J. (2022). Eulerian Multiphase Simulation of Phosphate Adsorption from Wastewater Using the Lattice Boltzmann Method. In *ProcessNet*, Leipzig, Germany.

Other talks

1. **Bukreev, F.**, Bingert, T. N., Czelusniak, L., Kummerländer, A., Ito, S., Krause, M. J. (2025). Reactive Microfluidics with LBM using OpenLB., Paul Scherrer Institute (PSI), Villigen, Switzerland
2. **Bukreev, F.**, Kummerländer, A., Ito, S., Krause, M. J. (2025). Wall-Modeled Large Eddy Simulation Approach with Incompressible Homogenized Lattice Boltzmann Method Using OpenLB. FALCON project meeting, Ostrava, Czech Republic
3. **Bukreev, F.**, Nirschl, H., Krause, M. J. (2024). Crystallization of Phosphates in a Nanopore. Neustadt an der Weinstraße, Germany
4. **Bukreev, F.**, Dapelo, D. (2024). LBM for Advection-Diffusion-Reaction Problems. In *Spring School: Lattice Boltzmann Methods with OpenLB Software Lab*, Heidelberg, Germany
5. **Bukreev, F.**, Dapelo, D. (2023). LBM for Advection-Diffusion-Reaction Problems. In *Spring School: Lattice Boltzmann Methods with OpenLB Software Lab*, London, UK

6. **Bukreev, F.**, Nirschl, H., Krause, M. J. (2023). Crystallization of Phosphates on and in Microparticles. University of Erlangen-Nuremberg, Erlangen, Germany

7. **Bukreev, F.**, Mödl, J. (2022). LBM for Advection-Diffusion-Reaction Problems. In *Spring School: Lattice Boltzmann Methods with OpenLB Software Lab*, Krakow, Poland

Software releases

1. Kummerländer, A., Bingert, T., **Bukreev, F.**, Czelusniak, L. E., Dapelo, D., Gaul, C., Hafen, N., Ito, S., Jeßberger, J., Khazaeipoul, D., Krüger, T., Kusumaatmaja, H., Marquardt, J. E., Raeli, A., Rennick, M., Prinz, F., Schecher, M., Schneider, A., Shimojima, Y., … Krause, M. J. (2025). OpenLB Release 1.8.1: Open Source Lattice Boltzmann Code (1.8.1). Zenodo. https://doi.org/10.5281/zenodo.15440776

2. Kummerländer, A., Bingert, T., **Bukreev, F.**, Czelusniak, L. E., Dapelo, D., Hafen, N., Heinzelmann, M., Ito, S., Jeßberger, J., Kusumaatmaja, H., Marquardt, J. E., Rennick, M., Pertzel, T., Prinz, F., Sadric, M., Schecher, M., Simonis, S., Sitter, P., Teutscher, D., Zhong, M., Krause, M. J. (2024). OpenLB Release 1.7: Open Source Lattice Boltzmann Code. Zenodo. https://doi.org/10.5281/zenodo.10684609

3. Kummerländer, A., Avis, S., Kusumaatmaja, H., **Bukreev, F.**, Crocoll, M., Dapelo, D., Hafen, N., Ito, S., Jeßberger, J., Marquardt, J. E., Mödl, J., Pertzel, T., Prinz, F., Raichle, F., Schecher, M., Simonis, S., Teutscher, D., Krause, M. J. (2023). OpenLB Release 1.6: Open Source Lattice Boltzmann Code. Zenodo. https://doi.org/10.5281/zenodo.7773497

4. Kummerländer, A., Avis, S., Kusumaatmaja, H., **Bukreev, F.**, Dapelo, D., Großmann, S., Hafen, N., Holeksa, C., Husfeldt, A., Jeßberger, J., Kronberg, L., Marquardt, J. E., Mödl, J., Nguyen, J., Pertzel, T., Simonis, S., Springmann, L., Suntoyo, N., Teutscher, D., Zhong, M., Krause, M. J. (2022). OpenLB Release 1.5: Open Source Lattice Boltzmann Code. Zenodo. https://doi.org/10.5281/zenodo.6469606